Title
Design and Analysis of Small-Scale Solar Thermal Combined Heat and Power Systems

Author
Sunter, Deborah Ann

Publication Date
2013

Peer reviewed|Thesis/dissertation

Design and Analysis of Small-Scale Solar Thermal Combined Heat and Power Systems

By

Deborah Ann Sunter

A dissertation submitted in partial satisfaction of the

requirements for the degree of

Doctor of Philosophy

in

Engineering- Mechanical Engineering

in the

Graduate Division

of the

University of California, Berkeley

Committee in charge:

Professor Van P. Carey, Chair
Professor Daniel M. Kammen
Professor Samuel S. Mao
Professor Per F. Peterson

Fall 2013

Design and Analysis of Small-Scale Solar Thermal Combined Heat and Power Systems

Abstract

Design and Analysis of Small-Scale Solar Thermal
Combined Heat and Power Systems

by

Deborah Ann Sunter

Doctor of Philosophy in Engineering- Mechanical Engineering

University of California, Berkeley

Professor Van P. Carey, Chair

Distributed solar thermal combined heat and power is an area where there is potential for significant innovation to reduce the cost of solar energy. Two areas for innovation were explored: reduced thermal losses in a novel dual-chamber absorber tube and parametric study for optimal efficiency of small-scale (5-10 kW) radial inflow turbines.

Increasing the peak temperature in solar thermal systems typically increases the cycle thermal efficiency. However, the outer wall temperature of the absorber tube also increases causing greater thermal losses to the surroundings. A novel finned dual-chamber absorber tube design was presented as a possible solution. Fins attached to the outer wall could serve as a heat sink to send heat into the inner chamber. Computation modeling was validated by a reduced-scale experiment to the accuracy of the correlations used. From these models, it has been demonstrated that the heat loss to the environment from the outer wall of the absorber tube could be reduced by 10-60%. The best performance was found when water enters the outer chamber at the highest mass flow rate tested. This impressive improvement encourages further development of the dual chamber design.

One of the primary obstacles of scaling down solar thermal technology for distributed power generation is finding an appropriate expander design. The radial inflow turbine was considered. A parametric study of seventeen input parameters was completed. Of these parameters, the mass flow rate, $r_{2,h}r_{2,t}$ (ratio of rotor exit hub radius to rotor exit tip radius) and $r_{2,t}r_{1a}$ (ratio of rotor exit tip to rotor inlet radius) had the greatest influence on the thermal efficiency of the system. Decreasing the mass flow rate both increased the turbine efficiency and increased the pressure drop across the turbine both of which enhanced the thermal efficiency. The optimized value of $r_{2,h}r_{2,t}$ and $r_{2,t}r_{1a}$ depended on the type of fluid. Wet fluids had an optimal performance with low values of $r_{2,t}r_{1a}$ but high values of $r_{2,h}r_{2,t}$. Dry fluids had an optimal thermal performance with low values of both $r_{2,h}r_{2,t}$ and $r_{2,t}r_{1a}$. Of the fluids studied it appears that dry fluids with low molecular mass and high critical temperature yielded the greatest thermal efficiency. Such fluids typically have low viscosity, allowing there to be less frictional losses in the turbine leading to better thermal efficiencies. Unfortunately, these fluids also

share the characteristic of being highly toxic. In order for the radial inflow turbine to scale with reasonable efficiency, a non-toxic dry fluid with low molecular mass and high critical temperature would need to be found.

Table of Contents

List of Figures

List of Tables

Acknowledgements

My experience as a graduate student at the University of California, Berkeley has been an incredibly rewarding experience both professionally and personally. I would like to extend my gratitude to all who have supported me on this journey.

I have been exceptionally fortunate to have an intellectually curious, socially impactful, interdisciplinary dissertation committee. I wish to express my most sincere appreciation to Professor Van P. Carey. As both my research advisor and dissertation chair, he has provided patient guidance, insightful mentorship, and authentic encouragement. Grateful thanks are extended to Professor Daniel M. Kammen for his inspirational global perspective on energy and extensive interdisciplinary collaboration. I thank Professor Samuel S. Mao for his encouragement in unique research applications and participation on both my qualifying exam

committee and dissertation committee. I also thank Professor Per F. Peterson for his participation on my dissertation committee and the valuable advice he offered.

In addition to my dissertation committee, I have had the pleasure of working with many outstanding professors. I would like to thank the other members of my qualifying committee for their time and mentorship: Professor Ralph Greif, Professor Omer Savas, and Professor Anna Lee Saxenian. I would also like to thank the professors that I have had the pleasure of teaching with: Professor Jyh-Yuan Chen, Professor Chris Dames, Professor Carlos Fernandez-Pello, Professor Michael Frenklach, and Dr. Hunter Mack.

My experimental work would not have been possible without the expertise of the ERSO Machine Shop and Mechanical Engineering Machine Shop. In particular, I am grateful for the fabrication work of Mr. Robert Amaral.

I would like to acknowledge and thank the sponsors of my research and international development: Haas School of Business Sustainable Products and Solutions Program, National Science Foundation, Soroptimist International, the Ralph A. Seban Heat Transfer Fellowship, and the Graduate Assembly at UC Berkeley.

I am truly blessed to have been able to share my journey at UC Berkeley with several incredible friends. I am thankful to all my colleagues in the Energy and Information Technologies Laboratory for their valuable research feedback and support. In particular, I would like to thank Sara Al-Beaini for her personal encouragement and laboratory assistance. I would also like to recognize the supportive friendships of Pamela Berkeley, Melissa and Alex Densmore, Vincent Escobedo, Brian Farley, Sue Kim, Kimberly Lau, Keith Miller, Eli Patten, and Ryan Sochol.

I never would have had the confidence to attempt an advanced degree if it wasn't for the love and support of my family. I thank my parents for believing in me before I was ready to believe in myself. I thank my sisters for challenging me with hopeful optimism and endless understanding.

Thank God!

I. Introduction

> "One thing I feel sure of and that is that the human race must finally utilize direct sun power or revert to barbarism. I would recommend all far-sighted engineers and inventors to work in this direction to their own profit, and the eternal welfare of the human race."
>
> Frank Shuman, Scientific America (Shuman, 1914)

Inventor Frank Shuman's call to action for solar energy research dates back to the start of WWI. Yet, he was not the first to recognize the potential for solar energy, specifically solar thermal. Written evidence of solar thermal research dates back to the 15th century with sketches from Leonardo da Vinci showing techniques for harnessing the sun's energy. In the 1700s, experimentation began with Swiss scientist Horace de Saussure and his 'hot box' which marks the world's first solar collector. It wasn't until the 1860s when French mathematician, August Mouchot, used solar energy to generate power in the world's first solar-powered steam engines. Shortly after, in 1891 Clarence Kemp patented the first commercial solar water heater and was able to sell 1,600 units in southern California alone (Jones & Bouamane, 2012). In the early 1900s, developments in solar thermal significantly slowed as major natural gas deposits were discovered. It wasn't until the 1970s oil crisis that there was refreshed vigor in solar thermal research (Jones & Bouamane, 2012). By the 1980s there were commercial utility solar thermal power plants. In 1994, the first distributed solar thermal generator was tied to a utility grid (Osborn & Collier, 1996). This marks a significant split in current solar thermal research. Although there is significant research being done in utility-scale solar thermal power plants, small-scale (5-10 kW) distributed solar thermal is an area of great interest.

As outlined in the Dept. of Energy publication "Basic Research Needs for Solar Energy Utilization," (Lewis & Crabtree, 2005) moderate temperature distributed solar thermal is an area where there is potential for significant innovation to reduce the cost of solar energy. The commercial efficiencies of solar thermal systems are at 20-35%. This offers a significant advantage over photovoltaics which currently have efficiencies between 10- 20% (Kalogirou, 2004). The case for small-scale solar Rankine systems is strongest when considering the use of rejected heat in a combined heat and power configuration. In this case, solar efficiencies in excess of 60% (combined heat and power) are possible with concentrating solar collectors at moderate temperatures (150-450°C) (Kalogirou, 2004) & (Kaushika, 1993). Thermal demands worldwide, including space heating and cooling, are a large fraction of total energy demands for customers using less than 10 kW peak power. Energy in the form of heat can also be stored in a more cost effective manner than electricity can be stored. Solar thermal technology can be manufactured using abundant and easily processed engineering materials such as steel, aluminum, glass and rubber (Pihl, Kushnir, Sanden, & Johnsson, 2012). For these reasons, solar thermal combined heat and power has potential to be exceptionally low-cost and environmentally benign.

Many technical challenges to small-scale solar thermal still exist. The thermal efficiency of a cycle can be improved by increasing the high-side temperature. However, in doing so, there are

several obstacles such as material limits and increased heat losses to the ambient. In order to address this challenge, a novel design on a solar absorber tube is discussed. This design allows for more efficient heat transfer, thus, reducing the outer wall temperature and thermal losses to the ambient. Another technical challenge to small-scale solar thermal is finding an appropriate small-scale expander. A parametric study of the radial-inflow turbine is analyzed for such an application. In addressing these two technical challenges, this dissertation hopes to encourage further research and demonstrate the feasibility of small-scale solar thermal combined heat and power generation.

II. Absorber Tube Analysis

Motivation

The most commonly used heat transfer fluid in commercial solar thermal plants is synthetic oil. However, recently there has been increasing interest in using water as the heat transfer fluid for DSG (direct steam generation). Although the high pressure of the steam in this circuit can sometimes be restrictive, Fernandez-Garcia (Fernandez-Garcia, Zarza, Valenzuela, & Perez, 2010) outlines several benefits of using DSG over synthetic oil. The maximum temperature of the cycle can be increased since it would no longer be governed by the current limit of 400^{o}C at which the thermal oils begin to degrade. Increasing the maximum temperature of the cycle allows for higher power cycle efficiencies, as well as lower fluid pumping parasitic losses (Price, 2009). DSG eliminates the need for an oil/steam heat exchanger and auxiliary thermal oil systems. Not only does this increase the overall plant efficiency but also reduces the investment and operating costs of the plant. According to a report by Altran Technologies, solar field investment costs could be cut by around 15% (Jaques, 2010). Lastly, environmental risks and chemical toxicity are reduced since there would be no leaks or fires from the thermal oil. One of the challenges in DSG technology is the reduced efficiency of the solar absorber tube as a result of the increased maximum temperature of the cycle. The hotter the solar absorber tube wall the greater the thermal losses are to the ambient. The novel absorber tube design that will be discussed in this chapter addresses this challenge by lowering the outer wall temperature and, thus, reducing the thermal losses to the ambient.

Literary Review

A number of investigators have explored solar absorber tube design to reduce thermal losses to the ambient. Raj et al. investigated the use of cylindrical inserts into the solar absorber tube (Raj, Srinivas, Natarajan, Kumar, Chengappa, & Deoras, 2013). Their results offered marginal improvements. Munoz and Abanades (Munoz & Abanades, 2011) show a 2% thermal efficiency increase by using internal helical fins to enhance heat transfer from the tube wall into the working fluid. Garcia-Valladares and Velázquez (García-Valladares & Velázquez, 2009) explored concentric counter flow circular heat exchangers for application in a solar thermal parabolic trough. No fins are used in their design. Depending on flow conditions, they showed improvement in absorber tube efficiency between 2.5-10%. Mastai et al proposed the likely expensive use of silica-carbon nanocomposites (Mastai, Polarz, & Antonietti, 2002). This chapter explores a novel solar absorber tube design for DSG in which concentric counter flow cylinders attached by strip fins reduces thermal losses to the ambient.

Nomenclature

$\boldsymbol{A}$	Surface area
B	Bias
$\boldsymbol{c_p}$	Specific heat at constant pressure
$\boldsymbol{C_D}$	Drag coefficient
$\boldsymbol{D}$	Diameter of single chamber tube
$\boldsymbol{D_h}$	Hydraulic diameter
$\boldsymbol{f}$	Friction factor
$\boldsymbol{F_{drag}}$	Force of drag
$\boldsymbol{g}$	Gravitational acceleration
$\boldsymbol{G}$	Mass flux
$\boldsymbol{h}$	Heat transfer coefficient
$\boldsymbol{h_{bend}}$	Distance from entry edge to end cover
$\boldsymbol{i}$	Enthalpy
$\boldsymbol{k}$	Thermal conductivity of tube
$\boldsymbol{k_{bend}}$	Correction factor for bend in annulus
$\boldsymbol{k_l}$	Thermal conductivity of working fluid
$\boldsymbol{l}$	Length of segment
$\boldsymbol{l_{bend}}$	Arc length of bend
$\boldsymbol{L}$	Length of the absorber tube
$\boldsymbol{\dot{m}}$	Mass flow rate
$\boldsymbol{n}$	Number of segments
$\boldsymbol{n_{fin}}$	Number of fins per segment
$\boldsymbol{P}$	Pressure
$\boldsymbol{Prec}$	Precision
$\boldsymbol{q}$"	Heat flux
$\boldsymbol{Q}$	Thermal energy
$\boldsymbol{r}$	Radius
$\boldsymbol{R_{bend}}$	Radius of curvature of bend
$\boldsymbol{s}$	Spacing between adjacent fins
$\boldsymbol{S}$	Suppression factor
$\boldsymbol{t_w}$	Thickness of tube wall
$\boldsymbol{t_{fin}}$	Thickness of fin $\left(A_{fin}/\left(n_{fin}l\right)\right)$
$\boldsymbol{T}$	Temperature
$\boldsymbol{u}$	Fluid velocity
$\boldsymbol{U}$	Uncertainty
$\boldsymbol{v}$	Specific volume
$\boldsymbol{x}$	Quality
$\boldsymbol{X}$	Martinelli parameter
$\boldsymbol{z}$	Axial coordinate
$\boldsymbol{z_o}$	Length of single tube extension

$\boldsymbol{\alpha}$	Void fraction
$\boldsymbol{\delta}$	Total resistance coefficient
$\boldsymbol{\delta_{el}}$	Thickness of cut edge
$\boldsymbol{\rho}$	Density
$\boldsymbol{\mu}$	Viscosity
$\boldsymbol{\lambda}$	Resistance coefficient
$\boldsymbol{\sigma}$	Surface tension
$\boldsymbol{r}$	Radius

Nondimensional

Bo	Boiling number
CR	Concentration ratio
Fr	Froude number
Nu	Nusselt number
Pr	Prandtl number
Re	Reynolds number $(u_m D_h/v)$
$\boldsymbol{r_{nd}}$	Radii ratio (r_i/r_o)
$\boldsymbol{\delta_{nd}}$	Ratio of the length of outer tube to length of inner tube $((L - z_o)/l)$

Subscript

amb	Ambient
CBD	Convective boiling dominant
fr	Friction
i	Inner
l	Liquid
le	Entire flow liquid only
loc	Local resistance
loss	Loss to ambient
m	Mean
NBD	Nucleate boiling dominant
nd	Nondimensional
o	Outer
sat	Saturated
solar	Input solar
v	Vapor
tp	Two phase
w	Wall

Description of Design

In a traditional design, three segments of heating (heating subcooled liquid, phase change heating, and superheating) would all be done in one or more single chamber tubes. During subcooled and phase change heating, the working fluid maintains moderate temperatures. However, during the superheating regime, the temperature of the working fluid increases and the heat transfer coefficient decreases corresponding to a significant increase in the outer wall temperature. The hotter the outer wall temperature results in greater losses to the ambient.

The effects may be reduced by encapsulating the single chamber tube in an evacuated glass chamber, as is often done in commercial use. Please note that the proposed design could also be encapsulated in an evacuated chamber to further reduce losses to the ambient or serve as a lower cost option that does not exist in an evacuated chamber.

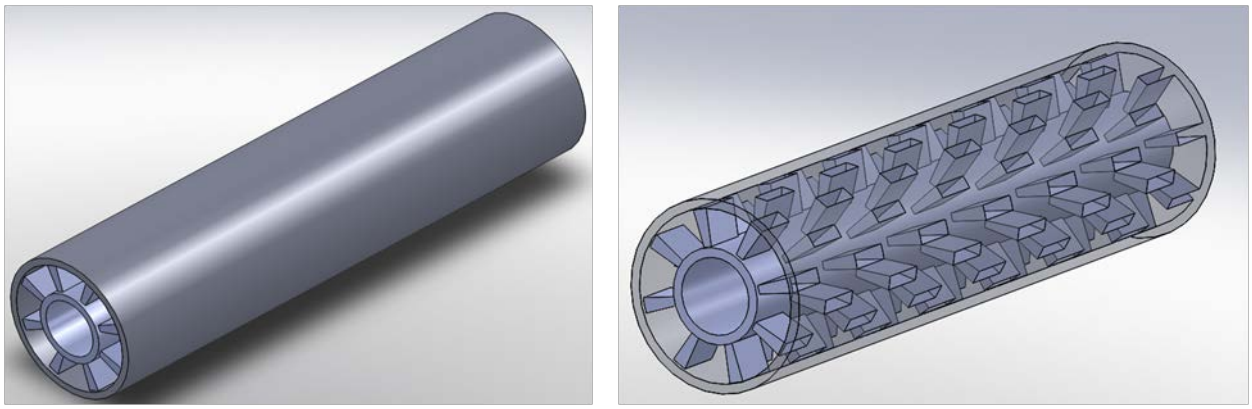

Figure 1: Dual chamber solar absorber tube design. Concentric cylinders are connected by rectangular fins. Fins may be offset as seen in the picture to the right where the outer wall is semi-transparent to better reveal the interior design.

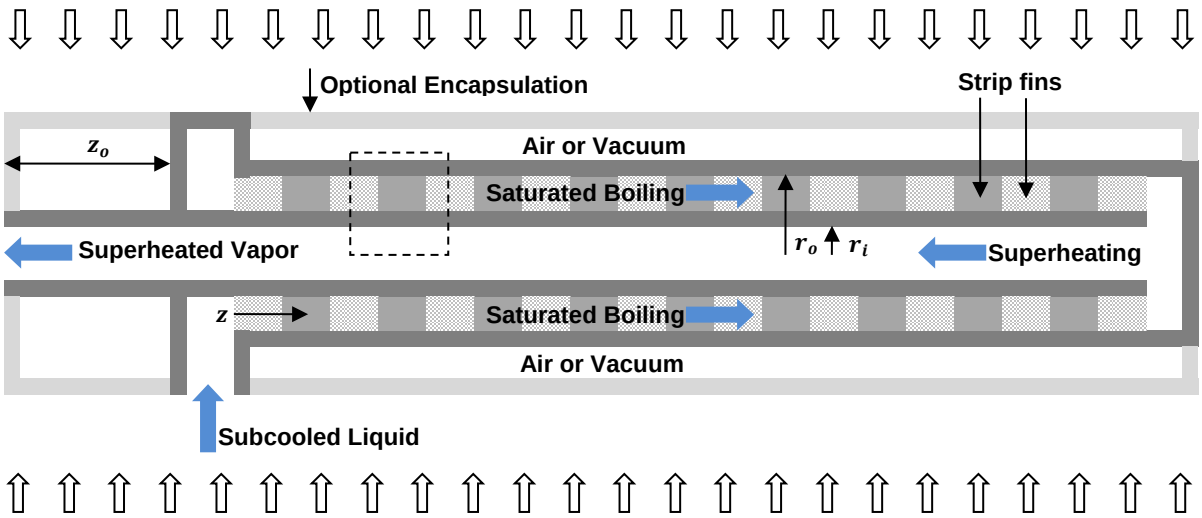

Figure 2: Longitudinal cross section of dual-chamber solar absorber tube. Detailed view of the region in the dotted square can be found in Fig. 4. Also, detailed depiction of two-phase flow regimes can be found in Figs. 52 and 56.

The proposed design either fully or partially encapsulates the single chamber tube in an outer annulus with fins connecting the two chambers as seen in Figs. 1-2. Subcooled liquid enters into the outer chamber (the annulus). The subcooled liquid is heated and phase change begins in this chamber. Therefore, the bulk fluid passing through the outer chamber is at or below saturation temperature. This moderate temperature largely dictates the outer wall temperature; thus, reducing the outer wall temperature relative to a single chamber design. In order to encourage heat transfer from the outer wall to the inner chamber, fins connect the two chamber walls. This allows a conduction path from the outer wall to the inner wall. After the fluid flows along the length of the outer chamber, it returns through the inner chamber. Fig. 2 shows a schematic of the fluid flow. Heat transfer from the fins in the outer chamber

allows heating to continue in the inner chamber. Phase change is completed and superheating of the steam occurs in the inner chamber. As the bulk temperature of the fluid in the inner chamber increases, heat will transfer from the inner chamber to the outer. To mitigate this, the sides of the fins and the outer portion of the inner chamber wall could be insulated. Please note that although the sides of the fins could be insulated, the surface areas connecting the fins to the inner and outer tube walls would not be. Hence, heat would be able to transfer radially into the inner chamber via the fins.

After some consideration, it was decided to also investigate the performance of the absorber tube with the fluid flow direction reversed. Fluid could enter the inner chamber and exit the outer chamber. The radial temperature gradient in this design is such that the coolest region is the fluid in the inner chamber and the hottest region is the outer wall with intermediate temperatures in between these regions. Localized insulation within the absorber tube would not be needed.

Depending on operating conditions, it is sometimes advantageous for the inner chamber to extend beyond the length of the outer chamber. Although the wall temperature in this extended region can be quite high, this allows for the solar heat flux to entirely go into increasing the temperature of the superheated gas as opposed to dominantly being used for phase change in the outer chamber. The outer chamber would be composed of several modular segments in order to provide optimal performance for a variety of applications.

Analytical & Computational Model

Model Assumptions

In the analysis that follows, axial conduction in both the fluid and the tube walls, as well as radial conduction in the tube walls, are found to be negligible and are ignored. This is true for both the single chamber and dual-chamber absorber tubes. According to Kays and Crawford (Kays, Crawford, & Weigand, 2005) axial conduction in a fluid can generally be neglected if the Peclet number is greater than 100. For each segment along the absorber tube, the Peclet number was tested and met this condition. By comparing the greatest wall temperature variation across consecutive segments, it was found that less than 5% of input heat flux goes to axial heat transfer in the tube walls. In order to test the significance of radial conduction in the tube walls, a simple resistive network in cylindrical coordinates was used. The tube walls are thin (less than a tenth of an inch) and highly conductive (aluminum with a conductivity of 255 W/mK). Based on these conditions, the temperature difference across the tube wall was found to be less than 0.3 K and considered negligible.

Single Chamber Absorber Tube Analysis

In order to a show how the dual chamber device is an improvement over the simple tube (single chamber), it is important to include the analysis of the simple tube for performance comparison. Fortunately, there has been sufficient work done, both analytically and experimentally, for a constant heat flux applied to a simple tube. The results that are later used for comparison are summarized in the following sections.

Pressure Drop

For single phase heating (heating either subcooled liquid or superheated gas), the pressure drop across a segment of tube is described by:

$$\frac{\Delta P}{l} = \frac{-f\rho u_m^2}{2D} \tag{1}$$

For laminar flow, the friction factor, f, is 64/Re. For turbulent flow, Bejan (Bejan, 1995) suggests the following empirical correlation for the friction factor:

$$f = 0.078\mathrm{Re}^{-0.25} \tag{2}$$

For saturated boiling, the Lockhart-Martinelli correlations for two-phase multipliers and the void fraction are used to compute the pressure drop (Lockhart & Martinelli, 1949). These correlations were chosen because they provide a good match to data from a series of studies of adiabatic two-phase flow in horizontal tubes. For the reader's convenience, the results are summarized here. First, the flow regime needs to be determined based on the Reynolds number for both the liquid and vapor phases.

$$\mathrm{Re_l} = \frac{G(1-x)D}{\mu_l} \tag{3}$$

$$Re_\mathrm{v} = \frac{G\mathrm{x}D}{\mu_v} \tag{4}$$

If the Reynolds number is less than 2300, it is assumed to be laminar flow. A friction factor for both the liquid and the vapor are defined based on the Reynolds number. Similar to single phase heating, the friction factor for laminar flow, f, is 64/Re. For turbulent flow, the friction factor is slightly different than that suggested by Bejan.

$$f = 0.079\mathrm{Re}^{-0.25} \tag{5}$$

Next, the Martinelli parameter, X, is computed.

$$X = \sqrt{\frac{(dP/dz)_l}{(dP/dz)_v}} \tag{6}$$

Where

$$\left(\frac{dP}{dz}\right)_l = \frac{-2f_l G^2(1-x)^2}{\rho_l D} \tag{7}$$

$$\left(\frac{dP}{dz}\right)_v = \frac{-2f_v G^2 x^2}{\rho_v D} \tag{8}$$

In the turbulent-turbulent case (when both the liquid and vapor are turbulent), the Martinelli parameter is adjusted according to the relationship provided by Martinelli and Nelson (Martinelli & Nelson, 1948).

$$X_{tt} = \left(\frac{\rho_v}{\rho_l}\right)^{0.571}\left(\frac{\mu_l}{\mu_v}\right)^{0.143}\left(\frac{1-x}{x}\right) \tag{9}$$

Next, the void faction, α, and its derivative are calculated using the correlations of Lockhart and Martinelli (Lockhart & Martinelli, 1949).

$$\alpha = \left[1 + 0.28\left(\frac{1-x}{x}\right)^{0.64}\left(\frac{\rho_v}{\rho_l}\right)^{0.36}\left(\frac{\mu_l}{\mu_v}\right)^{0.07}\right]^{-1} \tag{10}$$

$$\frac{d\alpha}{dx} = \left[1 + 0.28\left(\frac{1-x}{x}\right)^{0.64}\left(\frac{\rho_v}{\rho_l}\right)^{0.36}\left(\frac{\mu_l}{\mu_v}\right)^{0.07}\right]^{-2} * \left[0.1792\left(\frac{1-x}{x}\right)^{0.64}\left(\frac{\rho_v}{\rho_l}\right)^{0.36}\left(\frac{\mu_l}{\mu_v}\right)^{0.07}\right]\left(\frac{1-x}{x}\right)^{-0.36} x^{-2} \tag{11}$$

For the general case of separated flow, the pressure drop in a horizontal tube is:

$$-\left(\frac{dP}{dz}\right) = \emptyset_l^2\left[\frac{2f_l G^2(1-x)^2}{\rho_l D}\right] + G^2\frac{dx}{dz}\left\{\left[\frac{2xv_v}{\alpha} - \frac{2(1-x)v_l}{1-\alpha}\right] + \frac{d\alpha}{dx}\left[\frac{(1-x)^2 v_l}{(1-\alpha)^2} - \frac{x^2 v_v}{\alpha^2}\right]\right\} \tag{12}$$

Where

$$\emptyset_l^2 = 1 + \frac{C}{X} + \frac{1}{X^2} \tag{13}$$

X is the Martinelli parameter that has previously been defined. The constant, C, is dependent on the flow regime of both the liquid and gas separate flows. Its value can be determined in the following table.

Table 1: Two Phase Flow Constant Based on Flow Regime

Liquid	Gas	C
Turbulent	Turbulent	20
Laminar	Turbulent	12
Turbulent	Laminar	10
Laminar	Laminar	5

Each individual segment in the analysis is assumed to have a constant heat flux at the wall. With this assumption, the change in quality as a function of position along the tube can be written as follows:

$$\frac{dx}{dz} = \frac{\pi D q''}{\dot{m} i_{lv}} \tag{14}$$

Now, all the terms in Eqn. 12 have been defined and the pressure drop can be calculated for the saturated boiling taking into account both frictional losses and pressure drop from fluid acceleration.

Heat Transfer

It is assumed that there is a constant and uniform surface heat flux. By knowing the pressure and mean single phase fluid temperatures at the inlet and exit of the absorber tube, we can

compute the inlet and exit enthalpies. These enthalpies and the mass flow rate can be used to calculate the total heat transfer into the tube:

$$\dot{Q}_{in} = \dot{m}(i_{exit} - i_{inlet}) \tag{15}$$

Then, using the tube geometry, the heat flux on the outer surface of the tube can be found to be:

$$q" = \frac{\dot{Q}_{in}}{2\pi r_o L} \tag{16}$$

The absorber tube is broken into *n* segments. For each segment, the enthalpy of the previous segment is known. The mean temperature is approximated as the bulk temperature at the inlet of the segment. This is a conservative approximation that would slightly underestimate the wall temperature for the single chamber. This is a reasonable approximation since the segment size is small and there is greater uncertainty in the heat transfer coefficient, especially in the two-phase flow analysis. For the first segment, the enthalpy and bulk (mean) temperature are known from the inlet conditions. For each segment, the following procedure is used starting with the inlet segment:

1. Solve for the wall temperature of the given segment:

$$T_w = T_m + \frac{q"}{h} \tag{17}$$

2. Solve for the enthalpy at the exit of the segment:

$$i = \frac{q"2\pi rl}{\dot{m}} + i_{previous} \tag{18}$$

3. Based on the enthalpy and pressure, the bulk temperature and quality at the exit of the segment can be solved.
4. Proceed to the next segment.

The heat transfer coefficient used in step 1 would be determined based on phase and flow regime. For single phase heating (heating either subcooled liquid or superheated gas), empirical relations proposed by Gnielinksi (Gnielinski, 1975) would be used for turbulent flow. The Gnielinksi correlation was chosen based on its universal acceptance and that it accounts for both wall roughness and transitional flow conditions. For your convenience, the relations are listed below:

For turbulent flow (Re > 2300):

$$F = \frac{1}{(1.82log(Re) - 1.64)^2} \tag{19}$$

$$Nu = \frac{(F/8)(Re - 1000)Pr}{1 + \left(12.7(F/8)^{1/2}(Pr^{2/3} - 1)\right)} \tag{20}$$

$$h = \frac{Nuk_l}{D} \tag{21}$$

For laminar flow (Re<2300), from basic heat transfer theory, the Nusselt number for a tube with constant surface heat flux is 4.36. This would be used in the previous equation to find the appropriate heat transfer coefficient.

For two-phase heating, Kandlikar's correlation for saturated flow boiling was chosen based on its robust accuracy for a broad spectrum of flow conditions (Kandlikar, 1991). Kandlikar (Kandlikar, 1991) verified his correlation against experimentally obtained data for water flow to a mean deviation of 16%. Several key points of the analysis are summarized below.

For Kandlikar's correlation (Kandlikar, 1991), the heat transfer coefficient is computed for both nucleate boiling dominant regimes (h_{NBD}) and convective boiling dominant regimes (h_{CBD}). Whichever is largest is used for the heat transfer coefficient. Each regime is computed as follows:

$$h_{NBD} = 0.6683\left(\frac{\rho_l}{\rho_v}\right)^{0.1} x^{0.16}(1-x)^{0.64} f_2(Fr_{le}) h_{le} + 1058 Bo^{0.7} F_K (1-x)^{0.8} h_{le} \tag{22}$$

$$h_{CBD} = 1.136\left(\frac{\rho_l}{\rho_v}\right)^{0.45} x^{0.72}(1-x)^{0.08} f_2(Fr_{le}) h_{le} + 667.2 Bo^{0.7} F_K (1-x)^{0.8} h_{le} \tag{23}$$

where F_K is 1.00 for water and the boiling number, *Bo*, is defined as:

$$Bo = \frac{q"}{Gi_{lv}} \tag{24}$$

The heat transfer coefficient, h_{le}, is calculated based on Reynolds number as if the entire flow was liquid, Re_{le}:

$$Re_{le} = \frac{GD}{\mu_l} \tag{25}$$

For Re_{le} <2300 a Nusselt number of 4.36 is used in Eqn. 21. For Re_{le} between 2300 and 10^4, Gnielinski's (Gnielinski, 1975) correlation is used:

$$h_{le} = \left(\frac{k_l}{D}\right)\frac{(Re_{le}-1000)Pr_l(f/2)}{1+12.7\left(Pr_l^{2/3}-1\right)(f/2)^{0.5}} \tag{26}$$

Where

$$f = [1.58ln(Re_{le}) - 3.28]^{-2} \tag{27}$$

The function $f_2(Fr_{le})$ can be computed based on the Froude number, Fr_{le}.

$$f_2(Fr_{le}) = (25Fr_{le})^{0.3}\ for\ Fr_{le} < 0.04 \tag{28}$$

$$f_2(Fr_{le}) = 1\ for\ Fr_{le} \geq 0.04 \tag{29}$$

Where the Froude number is defined as

$$Fr_{le} = \frac{G^2}{\rho_l^2 g D} \tag{30}$$

Kandlikar's correlation (Kandlikar, 1991) is only valid for qualities less than 0.7. For qualities between 0.7 and 1, linear interpolation based on quality would be used between the heat transfer coefficient found at a quality of 0.7 and the heat transfer coefficient if the entire flow was single phase saturated vapor. As the quality increases, eventually the liquid inventory drops to a point when the tube wall surface is no longer entirely wetted by a liquid film. This phenomenon is referred to as partial dry out. The dry portions do not participate in the vaporization process. The result of this is a decrease in the mean heat transfer coefficient averaged along the wall. According to Figs. 7-8 in "Full-Core Test Method for Experimental Determination of Convective Boiling Heat Transfer Coefficients in Tubes of Crossflow Compact Evaporators," (Marseille, Carey, & Estergreen, 1988) this relationship is roughly linear for qualities between 0.7 and 1. The experimental findings of Marseille, Carey and Estergreen validate the linear interpolation method used for qualities greater than 0.7 in this model.

Dual Chamber Absorber Tube Analysis: Fluid Enters Inner Chamber

Pressure Drop

Inner Chamber

The pressure drop in the inner chamber is calculated using the same analytical methods as described for the single chamber absorber tube.

Outer Chamber

The pressure drop in the outer chamber is from form drag and frictional losses. To calculate the effect of drag, Joshi and Webb (Joshi & Webb, 1987) suggest using a drag coefficient, C_D, equal to 0.8. The drag force can be calculated as

$$F_{drag} = \frac{1}{2} C_D \rho u_m^2 A_{frontal,fin} \tag{31}$$

and the pressure drop from form drag can then be computed by

$$\Delta P_{form} = \frac{-F_{drag}}{A_{annulus}} \tag{32}$$

Where $A_{frontal,fin}$ is the frontal area of the fins and $A_{annulus}$ is the cross-sectional area of the annulus.

The frictional losses for turbulent single phase heating and phase change can be computed using the empirical relationships defined for the single chamber using the hydraulic diameter instead of the tube diameter. For laminar single phase flow, the frictional losses can be found as the sum of analytical losses found for flow in an annulus and flow over a flat plate (for the fins). Lundberg et al. (Lundberg, McCuen, & Reynolds, 1963) found the friction factor for laminar flow in an annulus to be as follows. Lundberg et al correlations were chosen because

they apply to a broad spectrum of fluid flows as they are based in fundamental fluid dynamic principles.

$$f_{annulus} = \frac{16(1 - r_{nd})^2}{\mathrm{Re}M} \tag{33}$$

Where

$$M = 1 + r_{nd}^2 - B \tag{34}$$

$$B = \frac{r_{nd}^2 - 1}{\ln(\mathrm{r_{nd}})} \tag{35}$$

For each fin, the frictional losses can be described by the following equation. This is twice the frictional losses for laminar flow over a flat plate as shown by Kays and Crawford (Kays, Crawford, & Weigand, 2005) to account for both sides of the fin parallel to the laminar fluid flow. Since there isn't a correlation available for an annulus with fins, it was decided to add the pressure losses from the individual components in the outer chamber. Therefore, in analyzing the fins as a separate entity, it is reasonable to use the correlation from Kays and Crawford (Kays, Crawford, & Weigand, 2005).

$$f_{fin} = \frac{2.656}{\left(\frac{u_m l}{\upsilon}\right)^{1/2}} \tag{36}$$

Bend

The pressure drop when the fluid moves between the inner and outer chambers in the bend can be computed based on two factors. The first and most significant is the fluid changing direction by 180°. Geary (Geary, 1975) suggests that that the pressure drop in 180° bend can be calculated as follows:

$$\Delta P_{bend} = \frac{f_{bend} L_{bend} {G_i}^2 x^2}{2 D_i \rho_v} \tag{37}$$

Where

$$f_{bend} = \frac{a\sqrt{Re_v}}{exp\left(0.215 \frac{2R_{bend}}{D_i}\right) x^{1.25}} \tag{38}$$

This correlation was chosen because it could be applied to both single and two-phase flow. The values for the mass flux, diameter, quality, density, and Reynolds number are all taken from the inner chamber segment closest to the bend. The constant, a, has a value of 8.03 x 10^{-4}. The radius of the bend, R_{bend}, is taken as the average of the radius of the inner chamber and the radius of the outer chamber. The length of the bend, L_{bend}, is approximated as the sum of the circumferences of two quarter circles, one with the outer diameter and one with the inner diameter:

$$L_{bend} = \frac{\pi D_o}{4} + \frac{\pi D_i}{4} \tag{39}$$

Since the cross-sectional area changes between the inner and outer chambers, there is also a pressure loss similar to that experienced by a nozzle. This pressure loss can be computed as follows:

$$\Delta P = \left(\frac{1}{2}\rho u_m^2\right)_{inner} - \left(\frac{1}{2}\rho u_m^2\right)_{outer} \tag{40}$$

Where values in the first set of parentheses are taken at the inner chamber segment closest to the bend and the values in the second set are taken at the outer chamber segment closest to the bend.

Heat Transfer

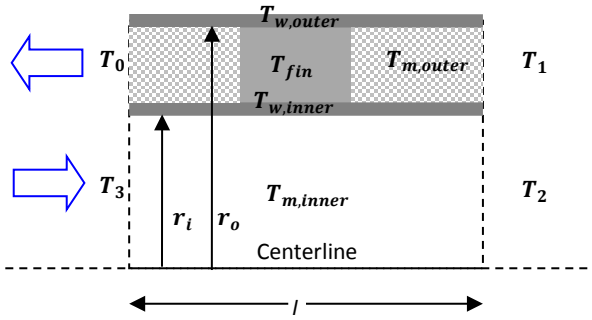

Figure 3: One segment of the dual-chamber solar absorber tube with temperatures defined. Fluid enters inner chamber.

Energy Balance Analysis

It is assumed that there is a constant and uniform surface heat flux. By knowing the pressure and mean single phase fluid temperatures at the inlet and exit of the absorber tube, we can compute the inlet and exit enthalpies. These enthalpies and the mass flow rate can be used to calculate the total heat transfer into the tube:

$$\dot{Q}_{in} = \dot{m}(i_{exit} - i_{inlet}) \tag{41}$$

Then, using the tube geometry, the heat flux on the outer surface of the tube can be found to be:

$$q" = \frac{\dot{Q}_{in}}{2\pi r_o L} \tag{42}$$

After several iterations of analytical models, the model that best represented the experimental results assumed a constant inner wall temperature. Since the inner chamber is dominated by the boiling process and boiling occurs at a single temperature, this assumption appears reasonable. However, some care needs to be given to accurately predict the inner wall temperature and perform an energy balance along the absorber tube. The following procedure is used to find the inner wall temperature and the axial distribution of the outer wall temperature along the dual chamber absorber tube:

1. The absorber tube is broken into *n* segments of length *l* as seen in Fig. 3.
2. A value for the inner wall temperature is guessed.

3. The heat transfer coefficient in the outer chamber, h_1, can be determined based on the fluid properties at the exit of the segment. This is discussed in greater detail in the next section.
4. The heat transfer coefficient in the inner chamber, h_3, can be determined based on the fluid properties at the inlet of the segment using correlations described for a single chamber tube.
5. Solve the simultaneous equations listed in Eqns. 43 –56 based on energy conservation in the two chambers.
6. Proceed to the next segment. The inlet of the outer chamber from the previous segment is the exit to the next segment. The exit of the inner chamber from the previous segment is the inlet of the next segment. Repeat from Step 3.
7. The last segment in the tube corresponds to where the fluid turns. The fluid exits the inner chamber and enters the outer chamber. Calculate the difference between the enthalpy leaving the inner chamber (i_2) and entering the outer chamber (i_1). While the difference is greater than 0.001, adjust the guessed inner wall temperature and return to Step 2. The Newton-Raphson method is used for accelerated convergence.

There are 14 unknowns to solve for simultaneously. They are i_{inner}, i_{outer}, i_1, i_2, $T_{m,inner}$, $T_{m,outer}$, T_1, T_2, $T_{w,outer}$, T_{fin}, $x_{m,inner}$, $x_{m,outer}$, x_1, and x_2. Based on either the inlet conditions to the absorber tube or from the previous segment, the enthalpies at locations 0 and 3 are known, i_0 and i_3. The enthalpies for the mean bulk fluid in the inner and outer chambers and be calculated as the average of the inlet and exit enthalpies to each chamber:

$$i_{m,inner} = \frac{i_2 + i_3}{2} \tag{43}$$

$$i_{m,outer} = \frac{i_0 + i_1}{2} \tag{44}$$

The heat transfer into the fluid in both chambers must be equal to the heat transfer into the segment:

$$q"2\pi r_o l = \dot{m}(i_3 - i_2) + \dot{m}(i_1 - i_0) \tag{45}$$

Taking the bulk fluid of the inner chamber as the control volume, only convection from the inner chamber wall contributes to the heat transfer into the fluid:

$$\dot{m}(i_3 - i_2) = h_{inner} 2\pi r_i l\left(T_{w,inner} - T_{m,inner}\right) \tag{46}$$

Taking the bulk fluid of the outer chamber as the control volume, there is convection from three surfaces (the outer wall, the inner wall, and the fins). Notice that there is a factor of two associated with the convection from the fin to account for convection on both sides of the fin. Also, the height of the fin is difference between the outer and inner radii. This energy balance can be expressed as:

$$\dot{m}(i_1 - i_0) = h_{outer}A_{w,outer}\left(T_{w,outer} - T_{m,outer}\right) + h_{outer}A_{w,inner}\left(T_{w,inner} - T_{m,outer}\right) + 2n_{fin}h_{outer}l(r_o - r_i)\left(T_{fin} - T_{m,outer}\right) \quad (47)$$

Where only the areas of the wall exposed to the fluid is considered and the area of the wall attached to the fins is neglected:

$$A_{w,outer} = 2\pi r_o l - n_{fin}t_{fin}l \quad (48)$$

$$A_{w,inner} = 2\pi r_i l - n_{fin}t_{fin}l \quad (49)$$

To calculate the temperature of the fin, there is conduction from the outer wall and to the inner wall as well as convection to the bulk fluid in the outer chamber. This can be expressed as:

$$\frac{n_{fin}kt_{fin}l\left(T_{w,outer} - T_{fin}\right)}{(r_o - r_i)/2} = \frac{n_{fin}kt_{fin}l\left(T_{fin} - T_{w,inner}\right)}{(r_o - r_i)/2} + 2n_{fin}h_{outer}l(r_o - r_i)\left(T_{fin} - T_{m,outer}\right) \quad (50)$$

Given that the pressure is known analytically, the temperature, enthalpy and quality can be related. Since the same equations would be used at the various locations in the segment, let the subscript j represent 1, 2, inner and outer.

If the fluid is saturated:

$$T_j = T_{sat} \quad (51)$$

$$i_j = i_l + x_j(i_v - i_l) \quad (52)$$

If the fluid is subcooled liquid:

$$i_j = \left(4.1894 \times 10^3\right)T_j - \left(1.1443 \times 10^6\right) \quad (53)$$

$$x_j = 0 \quad (54)$$

If the fluid is a superheated gas:

$$i_j = \left(2.01673 \times 10^3\right)T_j + \left(1.92341 \times 10^6\right) \quad (55)$$

$$x_j = 1 \quad (56)$$

The relationships between the enthalpy and temperature in Eqns. 53 and 55 were found using a linear curve fit for data from the Thermophysical Properties of Fluid Systems provided by the National Institute of Standards and Technology (NIST, 1992). The data was taken at atmospheric pressure and a temperature range of 25C – 100C for subcooled liquid water and 100C – 150C for superheated steam.

Based on quality information from the previous segment, the phase at all j locations is estimated. Then, the computed enthalpy value is checked against the magnitudes of the enthalpies of saturated liquid and saturated gas. If the estimated phase is incorrect, adjustments are made as necessary.

Heat Transfer Coefficient

For all regimes (laminar/turbulent and single/dual phase), empirical relations used in the single chamber absorber tube may be used. However, care should be taken to use the hydraulic diameter to account for the annular shape and the presence of fins in the outer chamber.

Dual Chamber Absorber Tube Analysis: Fluid Enters Outer Chamber

Pressure Drop

The pressure losses can be calculated using the same analysis for the dual chamber absorber tube with the fluid entering the inner chamber. The only modification is that the values for the mass flux, mean fluid velocity, diameter, quality, density, and Reynolds number for Eqns. 31-40 are all taken from the exit of the outer chamber segment.

Heat Transfer

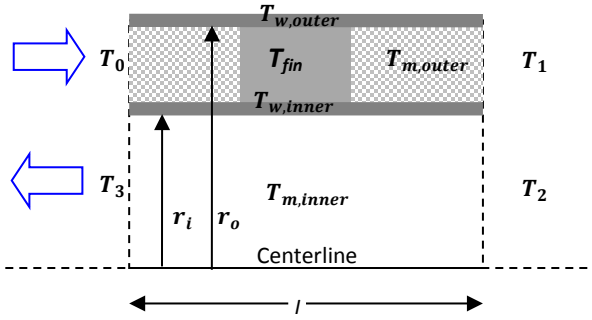

Figure 4: One segment of the dual-chamber solar absorber tube with temperatures defined. Fluid enters outer chamber.

Energy Balance Analysis

Unlike the analysis for the dual chamber absorber tube with the fluid entering the inner chamber, a different analytical model needs to be used to account for the change in flow direction. After several iterations of analytical models, the model that best represented the experimental results assumed a constant outer wall temperature. Recall that in the case of the reverse flow it was a constant inner wall temperature. Now, the outer chamber is dominated by the boiling process and since boiling occurs at a single temperature, this assumption seems reasonable. Once again, some care needs to be given to accurately predict the outer wall temperature and perform an energy balance along the absorber tube. The following procedure is used to find the outer wall temperature and the energy balance along the dual chamber absorber tube:

1. The absorber tube is broken into *n* segments of length *l* as seen in Fig. 4.
2. A value for the outer wall temperature is guessed.

3. The heat transfer coefficient in the outer chamber, h_1, can be determined based on the fluid properties at the inlet of the segment.
4. The heat transfer coefficient in the inner chamber, h_3, can be determined based on the fluid properties at the outlet of the segment using correlations described for a single chamber tube.
5. Solve the system of equations listed in Eqns. 43-44 and Eqns. 51-61 based on energy conservation in the two chambers. Note that some of these equations are different than the analysis in the reverse flow direction. Reasons for this are discussed shortly.
6. Proceed to the next segment. The outlet of the outer chamber from the previous segment is the inlet to the next segment. The inlet of the inner chamber from the previous segment is the exit of the next segment. Repeat from Step 3.
7. The last segment in the tube corresponds to where the fluid turns. The fluid exits the outer chamber and enters the inner chamber. Calculate the difference between the enthalpy leaving the outer chamber (i_1) and entering the inner chamber (i_2). While the difference is greater than 0.001, adjust the guessed outer wall temperature and return to Step 2. The Newton-Raphson method is used for accelerated convergence.

By fixing the outer wall temperature, one is unable to also restrict the surface heat flux on the outer wall as this would over-define the system of equations. A new system of equations was needed. It was decided to simplify the analysis by neglecting the convective heat transfer from both the fins and the inner tube wall into the fluid in the outer chamber. Based on experimental results and estimating the temperature of the fin as the mean temperature between the inner and outer wall, it was found that these convective heat transfers accounted for less than 10 percent of the heat transfer into the fluid in the outer chamber. The heat transfer into the fluid in the outer chamber is dominated by 90 percent as convective heat transfer from the outer wall. The outer wall is significantly hotter and has more area exposed to the outer chamber bulk fluid.

There are 14 unknowns to solve for simultaneously. They are i_{inner}, i_{outer}, i_1, i_2, $T_{m,inner}$, $T_{m,outer}$, T_1, T_2, $T_{w,inner}$, $T_{fin,base}$, $x_{m,inner}$, $x_{m,outer}$, x_1, and x_2. Based on either the inlet conditions to the absorber tube or from the previous segment, the enthalpies at locations 0 and 3 are known, i_0 and i_3. The enthalpies for the mean bulk fluid in the inner and outer chambers and be calculated as the average of the inlet and exit enthalpies to each chamber. These can be computed the same as in the reversed flow situation and can be seen in Eqns. 43 and 44. Also, the previously used relationships for temperature, enthalpy and quality in Eqns. 51- 56 are used again. The energy balance equations that differ from the analysis of the reverse flow are as follows.

Using the bulk fluid in the outer chamber as a control volume, only convection from the exposed inner surface of the outer wall contributes to the heat transfer into the fluid:

$$\dot{m}(i_1 - i_0) = h_{outer} A_{w,outer} \left(T_{w,outer} - T_{m,outer}\right) \tag{57}$$

Similarly, by taking the bulk fluid of the inner chamber as the control volume, only convection from the inner chamber wall contributes to the heat transfer into the fluid:

$$\dot{m}(i_2 - i_3) = h_{inner} 2\pi r_i l\left(T_{w,inner} - T_{m,inner}\right) \quad (58)$$

Heat is transferred via conduction through the fins to the inner chamber wall. Heat is then transferred via convection from the inner chamber wall to the bulk fluid in the inner chamber. Since only a fraction of the inner wall surface area is exposed to the fins, a new parameter for the temperature at the base of the fin, $T_{fin,base}$, was introduced and used in the following energy balance.

$$n_{fin} k t_{fin} l\left(T_{w,outer} - T_{fin,base}\right) = h_{inner} 2\pi r_i l\left(T_{w,inner} - T_{m,inner}\right) \quad (59)$$

Since the inner chamber wall is thin, one can neglect radial conduction. If the inner wall didn't participate in the heat transfer analysis, the total heat transfer from the base of the fins to the bulk fluid would be computed based on the cross-sectional area of the fins and the temperature of the base of the fins:

$$\dot{Q}_{inner} = h_{inner} n_{fin} t_{fin} l\left(T_{fin,base} - T_{m,inner}\right) \quad (60)$$

Since the inner wall is present, the heat transfer from the fins is assumed to be evenly distributed around the inner chamber wall. The heat transfer from the inner wall is the right-hand side of Eqn. 59 and Eqn. 60. These two heat transfers must be the same. By setting them equal to one another, the temperature of the base of the fin can be found and completes the needed system of equations:

$$T_{fin,base} = T_{m,inner} + \frac{2\pi r_i \left(T_{w,inner} - T_{m,inner}\right)}{n_{fin} t_{fin}} \quad (61)$$

Heat Transfer Coefficient

For all regimes (laminar/turbulent and single/dual phase), empirical relations used in the single chamber absorber tube may be used for to compute the heat transfer coefficient in the inner chamber.

For single phase laminar flow (Re<2300) in the outer chamber, the heat transfer coefficient is different than the reverse flow situation since the wall temperature is held constant instead of the surface heat flux. From basic heat transfer theory, the Nusselt number for a tube with constant wall temperature is 3.66. For single phase laminar flow in the outer chamber, a Nusselt number of 3.66 and the hydraulic diameter are used in Eqn 21. For single phase turbulent flow in the outer chamber, the heat transfer coefficient is found using the same correlations as the reverse flow.

Two phase flow in the outer chamber was dominated by nucleate boiling. Validation for this boiling regime is later discussed in the section title "Discussion of Absorber Tube Results." Previously, the two phase heat transfer coefficient was found using Kandlikar's correlation (Kandlikar, 1991). Kandlikar's correlation (Kandlikar, 1991) is used for broad spectrum of boiling incorporating both nucleate and convective boiling. Since saturated boiling in the outer chamber was almost entirely nucleate boiling, the Kandlikar correlation (Kandlikar, 1991) failed to capture the fluid behavior accurately. Instead, it was found that the Stephan and Abdelsalam correlation for pool boiling (exclusively nucleate boiling) more accurately predicted the fluid behavior (Stephan & Abdelsalam, 1980). Based on both dimensional analysis and optimal fits to

experimental data, Stephan and Abdelsalam (Stephan & Abdelsalam, 1980) proposed the following correlation for water with a mean absolute error of 11.3%:

$$q" = \{C_1(T_w - T_{sat}(P))\}^{1/0.327} \quad (62)$$

Where C_1 is 0.7 for 1 atm based on Fig. 5 in Stephan and Abdelsalam's journal article (Stephan & Abdelsalam, 1980).

Recall from basic convective heat transfer that

$$q" = h(T_w - T_m) \quad (63)$$

During the boiling process the mean fluid temperature is the saturation temperature at the given pressure. By equating Eqns. 62 and 63, the heat transfer coefficient can be obtains as

$$h = C_1(T_w - T_{sat}(P))^{(1/0.327)-1} \quad (64)$$

Experimental Methodology

Preliminary Nondimensional Analysis of Absorber Tube

A nondimensional analysis of the absorber tube was completed to give insight into two nondimensional values: r_{nd} and δ_{nd}. The radii radio, r_{nd}, is the ratio of the inner chamber radius to the outer chamber radius giving insight to the relative size of the two chambers. The next value, δ_{nd}, is the thickness of the fin relative to the length of the fin. This provided insight into the relative shape of the fin, as well as the portion of the outer wall that is connected to the fins. The results of the nondimensional analysis influenced the design choices for the experimental absorber tube configuration.

Cycle Definition for 10kW Case Study

This preliminary analysis was performed on a 10 kW combined heat and power system. For a combined heat and power system, it is necessary that the rejected temperature from the Rankine cycle is high enough to be able to create usable heat. Typical household hot water is kept at approximately 50^0C. A heat exchanger would be used so that the fluid in the closed Rankine cycle loop could condense while heating domestic hot water. To ensure a driving temperature difference of 15^0C, the temperature in the condenser was fixed at 65^0C. In other words, the minimum temperature of the Rankine cycle was fixed at 65^0C. The pressure ratio is fixed at 10. The following is a summary of the system constraints and idealizations of the Rankine cycle:

1. The minimum temperature is fixed at 65^0C.
2. The inlet to the pump is saturated liquid.
3. The exit to the turbine is saturated vapor.
4. The pump efficiency is 90%.
5. The turbine efficiency is 85%.
6. The pressure ratio is fixed at 10.
7. Just to the left of the saturation dome, the fluid is assumed to be incompressible.

Absorber Tube Characteristics

In order to produce 10 kW for the cycle described above, the evaporator would have the following characteristics:

1. The pressure of the evaporator is 2.47 atm (corresponding saturation temperature is 127^{o}C).
2. The mass flow rate through the evaporator is 0.025kg/s.
3. The temperature at the inlet of the evaporator is 65^{o}C.
4. The temperature at the exit of the evaporator is 276^{o}C.

The absorber tube was further defined as:

1. The evaporator is defined by 5 solar absorber tubes, each with a mass flow rate of 0.005 kg/s to produce 2kW each.
2. When analyzing the dual chamber design, water enters the outer chamber and exits the inner chamber.
3. The outer radius of the dual chamber solar absorber tube is fixed at one inch. The inner radius and, therefore, the radius of the single chamber absorber tube are defined by r_{nd}.
4. The material of the absorber tubes is aluminum and has a conductivity of 255 W/mK.
5. The ambient air is at 25^{o}C.
6. The heat transfer coefficient to the ambient, h_{loss}, is assumed to be 25 W/m^{2}K and includes effects of both convection and radiation from the surface of the absorber tube.
7. The number of radially symmetric fins in the outer chamber is five.
8. Typical concentration ratios for parabolic troughs are 8-80; here a concentration ratio of 25 is chosen for an absorber tube of 1'' radius resulting in an input solar power per length of absorber tube of 4 kW/m.

Table 2. Summary of Absorber Tube Design Constraints

Parameter	Assigned Value
Mass Flow Rate	0.025 kg/s
Inlet Temperature	65^{o}C
Exit Temperature	276 ^{o}C
Inlet Pressure	2.47 atm
Outer Radius	1 inch
Tube Conductivity	255 W/mK
Ambient Air Temperature	25^{o}C
Heat Transfer Coefficient to Ambient	25 W/m^{2}K
Number of Radially Symmetric Fins	5
Input Solar Power Per Length	4 kW/m

Computational Model

The preliminary design provided insights for the fabrication of the experimentally tested absorber tube. The computation model that was used in this analysis is subsequently refined based on experimental results. Hence, there are several differences in the model described

here and the model previously discussed in "Analytical and Computational Models." Also, in this computational model, the inlet and exit conditions are fixed but the length of the absorber tube is not. Instead of comparing the axial wall temperature for a fixed length absorber tube, this model compares the needed absorber tube length to achieve the desired exit condition for the 10 kW case study. The methods previously described to calculate the heat transfer coefficient of the bulk fluid are used without modification, except that Kandlikar's model (Kandlikar, 1991) is used to calculate the heat transfer coefficient for two-phase flow in both chambers.

Single Chamber Model

The computational model for the single chamber absorber tube with an unknown length follows this procedure.

1. Guess the needed length of the absorber tube.
2. The absorber tube is broken into *n* segments. For each segment, the enthalpy of the previous segment is known. For the first segment, the enthalpy and bulk temperature are known from the inlet conditions.
3. Guess the wall temperature of the segment under consideration.
4. Calculate the heat flux that enters the fluid. For theoretical comparisons, an average heat loss coefficient can be estimated, h_{loss}, which takes into account effects from conduction, convection and radiation. This can be used to calculate the heat flux that is being lost to the environment.

$$q"_{loss} = h_{loss}(T_w - T_{amb}) \tag{65}$$

   The solar heat flux that enters the absorber tube is a function of the collector geometry (concentration ratio, *CR*), collector efficiency, and incident solar radiation.

$$q"_{input} = \eta_{collector} CR q"_{solar} \tag{66}$$

   Then, the heat flux that enters the fluid can be evaluated as

$$q" = q"_{input} - q"_{loss} \tag{67}$$

5. Solve for the wall temperature:

$$T_w = T_m + \frac{q"}{h} \tag{68}$$

6. Check that the difference between the guessed wall temperature and the wall temperature solved for in the previous step is less than 0.001°C. If this criterion is not satisfied, return to step 3 with a new estimate for the wall temperature.
7. Solve for the enthalpy at the exit of the segment:

$$i = \frac{q"2\pi rl}{\dot{m}} + i_{previous} \tag{69}$$

8. Based on the enthalpy, the bulk temperature and quality can be solved.
9. Proceed to the next segment.
10. The enthalpy at the exit of the final segment must be within 0.001 kJ/kg of the desired case study exit condition. If this criterion is not satisfied, return to step 1 with a new

estimate for the length of the absorber tube. The Newton-Raphson method is used for accelerated convergence.

Dual Chamber Model

The dual chamber model actually differs significantly from the model described in the section titled "Analytical and Computational Models." The nondimensional analysis was completed before the experimental results showed that fixing either the inner or outer wall temperature (based on flow direction) was an appropriate approximation yielding better results than the model described below. In this model, the fin is not at a uniform temperature but instead modeled as having two temperatures, $T_{fin,1}$ on the outer wall surface and $T_{fin,3}$ on the inner wall surface. Please see Fig. 5.

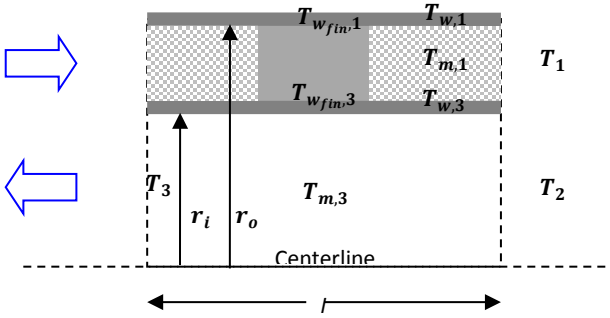

Figure 5: One segment of dual chamber solar absorber tube with temperatures defined for preliminary nondimensional analysis.

1. Guess the needed length of the absorber tube.
2. The absorber tube is broken into *n* segments. For each segment, the enthalpy of the previous segment is known. For the first segment, the enthalpy and bulk temperature are known from the inlet conditions.
3. Calculate the total heat transfer into the fluid based on the inlet and exit conditions of the dual chamber absorber tube.
4. Guess the input heat flux, q''_{input}.
5. Knowing the inlet and exit enthalpies, the bulk fluid temperatures and qualities can be computed (T_o, x_o, T_3, x_3).
6. The heat transfer coefficient in the outer chamber, h_1, can be determined based on the fluid properties at the inlet of the segment.
7. The heat transfer coefficient in the inner chamber, h_3, can be determined based on the fluid properties at the exit of the segment using correlations described for a single chamber tube.
8. Solve the simultaneous equations listed in Eqns. 74-85 based on energy conservation in the two chambers.
9. Calculate the heat lost to the ambient for the segment:

$$\dot{Q}_{loss,segment} = h_{loss}\left(A_{w,o} - A_{fin}\right)\left(T_{w,1} - T_{amb}\right) + h_{loss}A_{fin}\left(T_{fin,1} - T_{amb}\right) \tag{70}$$

10. Proceed to the next segment. The exit of the outer chamber from the previous segment is the inlet to the next segment. The inlet of the inner chamber from the previous segment is the exit of the next segment. Repeat from Step 5.

11. The last segment in the tube corresponds to where the fluid turns. The fluid exits the outer chamber and enters the inner chamber. Calculate the difference between the enthalpy leaving the outer chamber (i_1) and the enthalpy entering the inner chamber (i_2). While the difference is greater than 0.001 kJ/kg, adjust the guessed inlet heat flux and return to Step 4.
12. Calculate the total heat loss to the environment along the entire absorber tube:

$$\dot{Q}_{loss,total} = \sum_{n} \dot{Q}_{loss,segment} \tag{71}$$

13. Calculate the net heat transfer into the fluid:

$$\dot{Q}_{in} = q"_{input} n\left(A_{w,o} - A_{fin}\right) - \dot{Q}_{loss,total} \tag{72}$$

14. Calculate the enthalpy at the exit of the absorber tube based on the inlet condition and net heat transfer into the fluid:

$$i_{exit,calculated} = i_{inlet} + \frac{\dot{Q}_{in}}{\dot{m}} \tag{73}$$

15. The enthalpy at the exit of the final segment must be within 0.001 kJ/kg of the desired case study exit condition. If this criterion is not satisfied, return to step 1 with a new estimate for the length of the absorber tube. The Newton-Raphson method is used for accelerated convergence.

The simultaneous equations to be solved in Step 8 are shown here. There is an energy balance of the portion of the outer wall that is not connected to a fin:

$$\begin{aligned} q"_{input}\left(A_{w,o} - A_{fin}\right) + \frac{n_{fin} k t_w l}{s/2}\left(T_{w_{fin},1} - T_{w,1}\right) \\ = h_1\left(A_{w,o} - A_{fin}\right)\left(T_{w,1} - T_{m,1}\right) \\ + h_{loss}\left(A_{w,o} - A_{fin}\right)\left(T_{w,1} - T_{amb}\right) \end{aligned} \tag{74}$$

The energy balance of the fin:

$$\begin{aligned} q"A_{fin} = \frac{k A_{fin}}{r_o(1 - r_{nd})}\left(T_{w_{fin},1} - T_{w_{fin},3}\right) + \frac{n_{fin} k t_w l}{s/2}\left(T_{w_{fin},1} - T_{w,1}\right) \\ + h_{loss} A_{fin}\left(T_{w_{fin},1} - T_{amb}\right) \end{aligned} \tag{75}$$

The energy balance for the bulk fluid in the outer chamber:

$$\dot{m}(i_1 - i_o) = h_1\left(A_{w,o} - A_{fin}\right)\left(T_{w,1} - T_{m,1}\right) \tag{76}$$

The energy balance for the bulk fluid in the inner chamber:

$$\dot{m}(i_3 - i_2) = h_3 A_{fin}\left(T_{w_{fin},3} - T_{m,3}\right) \tag{77}$$

Calculate the mean enthalpies:

$$i_{m,1} = \frac{i_o + i_1}{2} \tag{78}$$

$$i_{m,3} = \frac{i_2 + i_3}{2} \tag{79}$$

Calculate the mean temperature of the bulk fluid and the corresponding qualities:

If i_m is saturated:

$$T_m = T_{sat} \tag{80}$$

$$i_m = i_l + x(i_v - i_l) \tag{81}$$

If i_m is subcooled liquid:

$$i_m = (4.1894 \times 10^3)T_m - (1.1443 \times 10^6) \tag{82}$$

$$x = 0 \tag{83}$$

If i_m is superheated gas:

$$i_m = (2.01673 \times 10^3)T_m + (1.92341 \times 10^6) \tag{84}$$

$$x = 1 \tag{85}$$

Results for Interior Segment Design

In order to compare the performance of the various dual chamber designs with the traditional single chamber solar absorber tube, the needed length of the absorber tube to achieve 10 kW of power was compared. The shorter the needed absorber tube implies the shorter the needed collector. Alternatively, for the same length of collector, a greater power output could be achieved.

As can be seen in Fig. 6, adjusting δ_{nd} between 0.7 and 1.0 shows significant change to the needed length of the dual-chamber absorber tube (over 10%). Although the optimum δ_{nd} occurs between 0.85 and 1, there does not appear to be a correlation between the radii ratio and the optimum δ_{nd}.

For each radii ratio explored (r_{nd} = 0.75, 0.80, 0.85 and 0.90), δ_{nd} was varied to find the optimum combination that minimized the length of the dual-chamber solar absorber tube. It was found that increasing δ_{nd} between 0.85 and 1, depending on the radii ratio, minimized the length of the dual-chamber tube. This length is compared to the needed length of a single chamber absorber tube. The radius of the single chamber absorber tube is taken to be the inner radius of the dual chamber tube. Essentially, this comparison allows us to see the benefit of encapsulating an existing single chamber tube with a finned outer annulus. The results can be seen in Figs. 7-8.

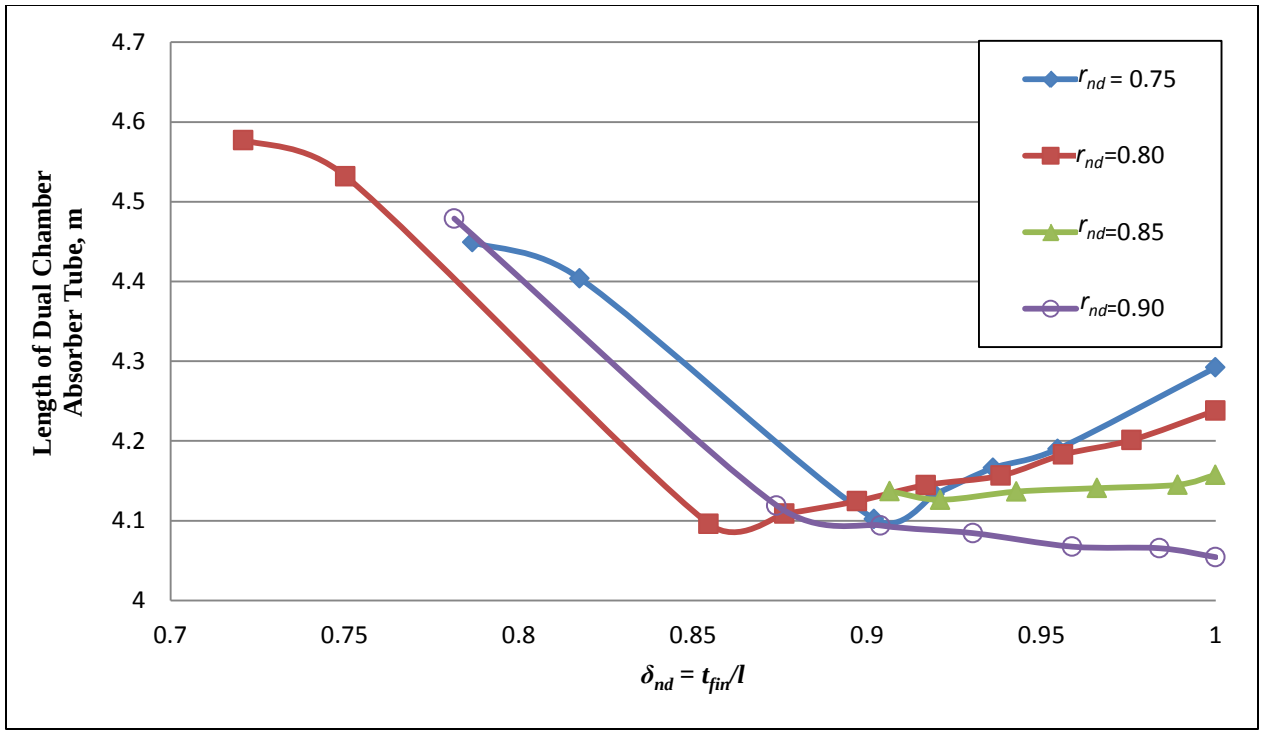

Figure 6: Predicted length of dual chamber solar absorber tube needed to produce 2 kW based on design constraints listed in Table 2. Various values of δ_{nd} and r_{nd} were explored.

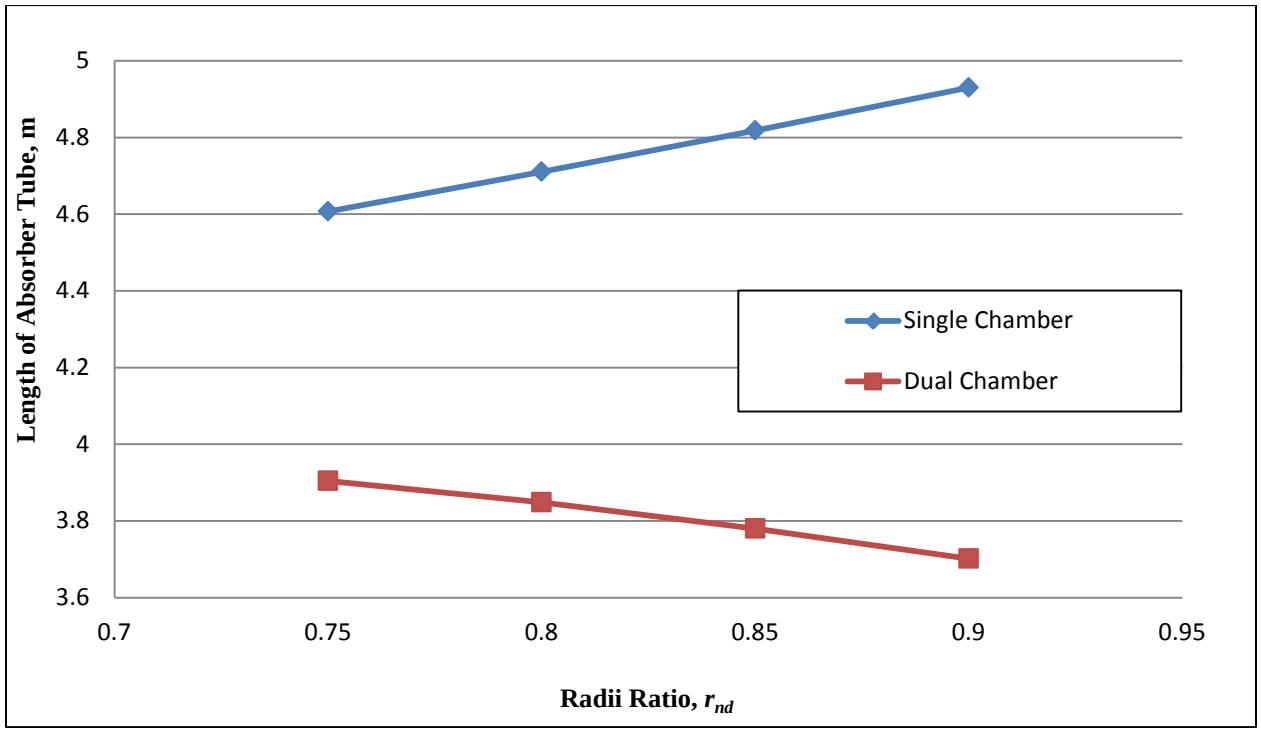

Figure 7: Comparison between the predicted length of a dual chamber solar absorber tube and a single chamber tube needed to produce 2 kW based on the design constraints listed in Table 2. δ_{nd} and r_{nd} were both varied.

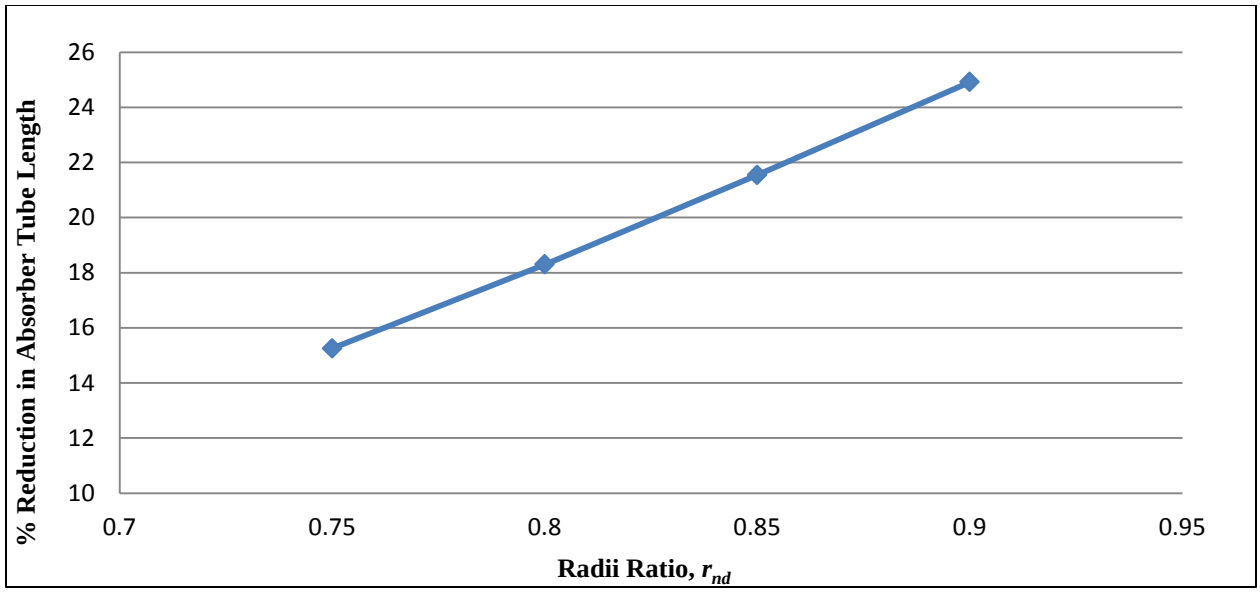

Figure 8: Percent reduction in the predicted absorber tube length by replacing a traditional single chamber absorber tube with a dual chamber solar absorber tube based on design constraints listed in Table 2. δ_{nd} and r_{nd} were varied.

For the design space considered, a dual chamber solar absorber tube with r_{nd} of 0.9 and δ_{nd} of 1 allowed for the shortest predicted length of the needed collector. Fig. 9 shows the temperature profiles of the bulk fluid and outer wall for this configuration. Five collectors at a length of 3.7 meters each would be required to produce 10 kW. This is a 25% reduction in the needed length of the collector had a single chamber absorber tube been used instead. From Fig. 9 it is clear that the dual chamber absorber tube reduces the outer wall temperature, which in turn reduced the thermal losses to the ambient.

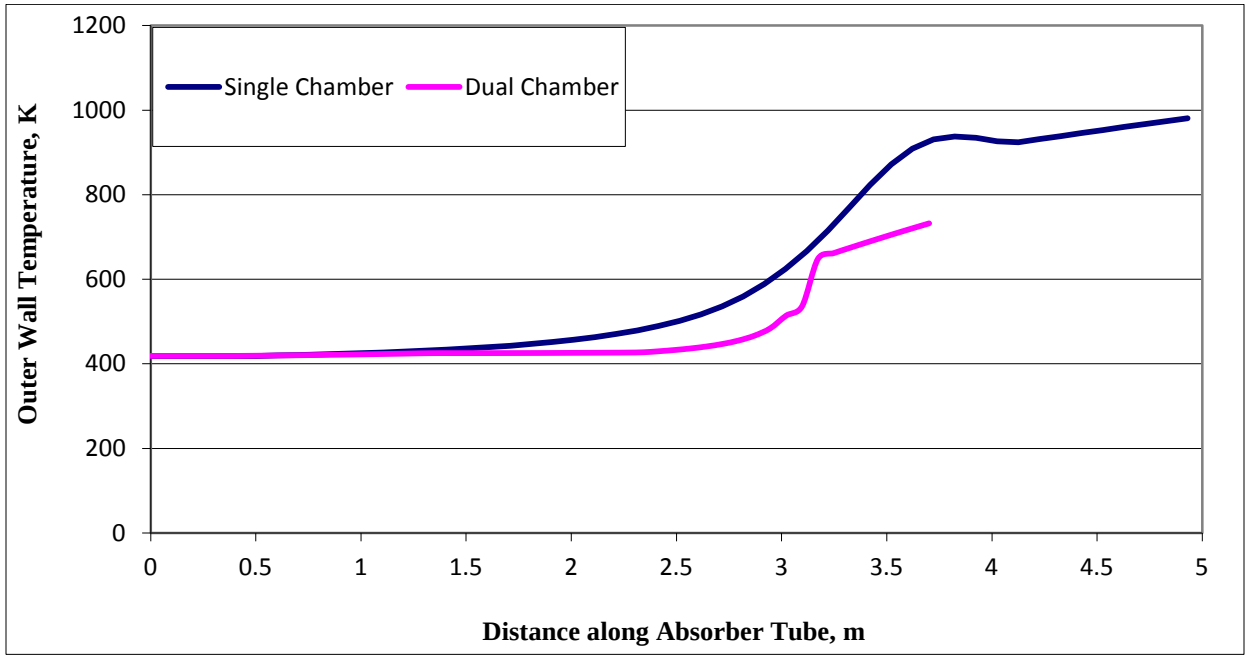

Figure 9: Comparison between the outer wall temperature of the dual chamber solar absorber tube and the traditional single chamber tube to produce 2 kW based on design constraints listed in Table 2. Tube geometry for the dual chamber tube is defined by δ_{nd} of 1 and r_{nd} of 0.9.

The dual chamber solar absorber tube with a finned outer annulus was shown to be effective at reducing the thermal losses to the ambient by reducing the outer wall temperature. For the 10 kW case study it was shown that replacing a traditional single chamber solar absorber tube with a dual chamber absorber tube would result in a 25% reduction in the predicted length of the needed collector. These promising results encourage further investigation of this novel evaporator design. One assumption that warrants further investigation is the practicality of the insulated surfaces. If the insulation was removed or only partially effective, the performance of the dual-chamber absorber tube would worsen. Another topic of interest is extending the inner chamber beyond the length of the outer chamber. This has potential to provide greater performance for the dual-chamber tube by improving the heating of the inner chamber.

The preliminary nondimensional analysis provided some insight into the construction of the experimental absorber tube. First, it showed that a high radii ratio offered superior results. However, there is a practical machine limit. Using the equipment available, a clearance of at least 4 mm was required between chamber walls and each wall needed to be a minimum thickness of 2 mm. This translated to a maximum radii ratio of 2/3. For the nondimensional parameter δ_{nd}, it was seen that the performance improved by having thick fins relative to the length of the fin. However, experimentally, both inline and strip fin assemblies were to be tested. To prevent blockage in the strip fin assembly, the fins could not be too thick. Ultimately, the fin thickness was limited to 5 mm and δ_{nd} was fixed at 0.18. For δ_{nd} it was seen that the performance depended very little on length of segment. After convergence was met, continuing to increase the number of segments and, therefore, decrease each segment length, showed no difference in performance. This is attributed to the fact that the fluid primarily behaved turbulently since the presence of the fins would trip the flow and the boiling process is quite chaotic generating additional turbulence. Hence, the boundary layer was uniformly thin throughout.

Design of Annular Turn

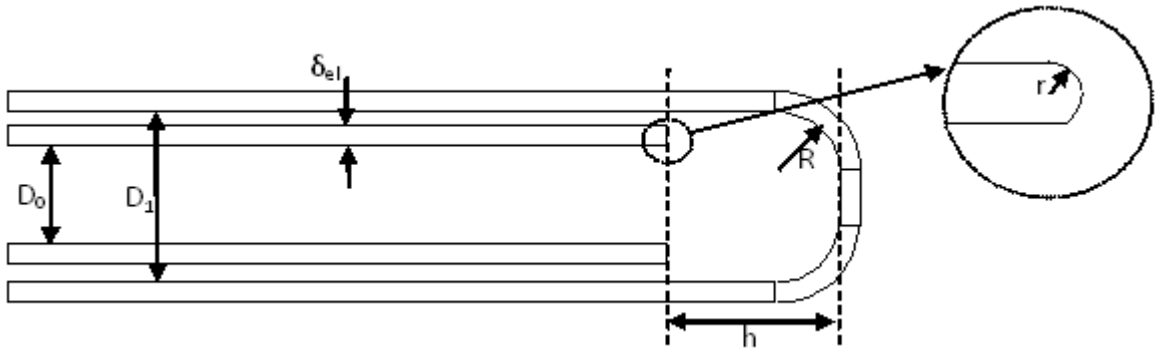

Figure 10: Diagram of pertinent parameters to annular turn design.

At the end of the absorber tube, the fluid needs to reverse direction. Although there is no heating in the segment where the fluid reverses direction, there are pressure losses. Analysis was done to minimize these pressure losses based on nondimensional analyses by Idelchik (Idelchik, 1994). Please refer to Fig. 10 for pertinent geometries used in this analysis. The pressure loss can be computed as follows:

$$\Delta P = \delta\left(\frac{\rho u_m^2}{2}\right) \tag{86}$$

where the total resistance coefficient, δ, is defined as the sum of the local resistance of the bend and the friction coefficient.

$$\delta = \delta_{fr} + \delta_{loc} \tag{87}$$

The friction coefficient can be calculated by:

$$\delta_{fr} = k_{bend}\lambda\left(\frac{l_{bend}}{D_h}\right) \tag{88}$$

Where D_h is the average hydraulic diameter of the inner and outer chambers and l_{bend} is the arc length calculated as

$$l_{bend} = \frac{\pi}{2}\left(\frac{D_1 - D_0}{2} + \frac{D_0}{2}\right) \tag{89}$$

The resistance coefficient, λ, needs to be computed based on flow regime. Below are the equations to be used for laminar and turbulent flow regimes.

For laminar flows (Re<2300):

$$\lambda = 64/Re \tag{90}$$

For turbulent flows:

$$\lambda = \frac{1}{(1.8log(Re) - 1.64)^2} \tag{91}$$

The correction factor, k_{bend}, accounts for the annular design. It also needs to be calculated based on flow regime.

For laminar flows (Re<2300):

$$k_{bend} = \frac{1 - (D_0/D_1)^2}{1 + (D_0/D_1)^2 + [1 - (D_0/D_1)^2]/ln(D_0/D_1)} \tag{92}$$

For turbulent flows:

$$k_{bend} = \left(\frac{0.02D_0}{D_1} + 0.98\right)\left(\frac{1}{\lambda} - 0.27(D_0/D_1) + 0.1\right) \tag{93}$$

The coefficient of the local hydraulic resistance, δ_{loc}, of an annular turn through 180^o depends on the relative distance from the entry edge of the inner tube up to the end cover (hood) of the outer circular tube (h_{bend}/D_0), the area ratio between the outer and inner tubes, the relative thickness of the cut edge to the inner tube diameter (δ_{el}/D_0), and the relative curvature radius of the cover (R_{bend}/D_1). Of these, the nondimensional parameter that most affects the pressure loss is h_{bend}/D_0.

The relative thickness of the cut edge to the inner tube diameter (δ_{el}/D_0) and the area ratio between the outer and inner tubes are fixed by the design limitation discussed for the interior segment nondimensional analysis. The optimum curvature radius of the end cover (R_{bend}/D_1) is 0.18-0.35 for flow exiting the inner tube and 0.2 – 0.45 for flow exiting the outer annulus. Since the design will be tested for both flow directions and there is overlap for ratios 0.2-0.35, the curvature radius of the end cover (R_{bend}/D_1) was selected to be 0.3 for the experimental design.

The most important parameter in the turn is the relative distance from the entry edge of the inner tube up to the end cover (hood) of the outer circular tube (h_{bend}/D_0). It is important to carefully select this parameter not only because it most strongly influences pressure losses but also it can result in flow instability. The instability can be explained by periodic blowing-off and entrainment by the flow of the separating eddy at the outer wall and at the inner wall of the annular turn. The optimum value of h_{bend}/D_0 for fluid exiting the inner tube is 0.23 – 0.27 and in this range the local resistance in the bend, δ_{loc} , is 1.70. Additionally, the flow is unstable when h_{bend}/D_0 is between 0.28-1.4. When the fluid is in the reverse direction, the optimum value of h_{bend}/D_0 is between 0.40 – 0.62 with the local resistance in the bend being 0.24. The flow is unstable when h_{bend}/D_0 is between 0.60-2.0. Unlike the previous parameter, there is no overlap in the optimum value of h_{bend}/D_0 for both flow directions. Since the local resistance in the bend is much greater when the flow exits the inner tube than in the reverse direction, it was decided to design based on the flow exiting the inner tube and to choose h_{bend}/D_0 to be 0.25. This value is stable for both flow directions.

Fabrication of Dual Chamber Absorber Tube

The absorber tube was fabricated in ERSO machine shop in Cory Hall at the University of California, Berkeley. It was constructed using AL-6061. The following are the final design diagrams submitted to the machine shop after a series of revisions to simplify the manufacturing process. Some of these revisions are summarized here. A diffuser segment was added to promote more radially uniform fluid flow. An o-ring design was replaced by a lip and groove design for connecting the segments of the absorber tube. This was chosen because of difficulty finding appropriately sized o-rings. Teflon was used between the lip and groove design to ensure there were no leaks. Two ANSI 10-24 threaded rods connected the diffuser chamber with the turn segment to provide structure and stability to the design.

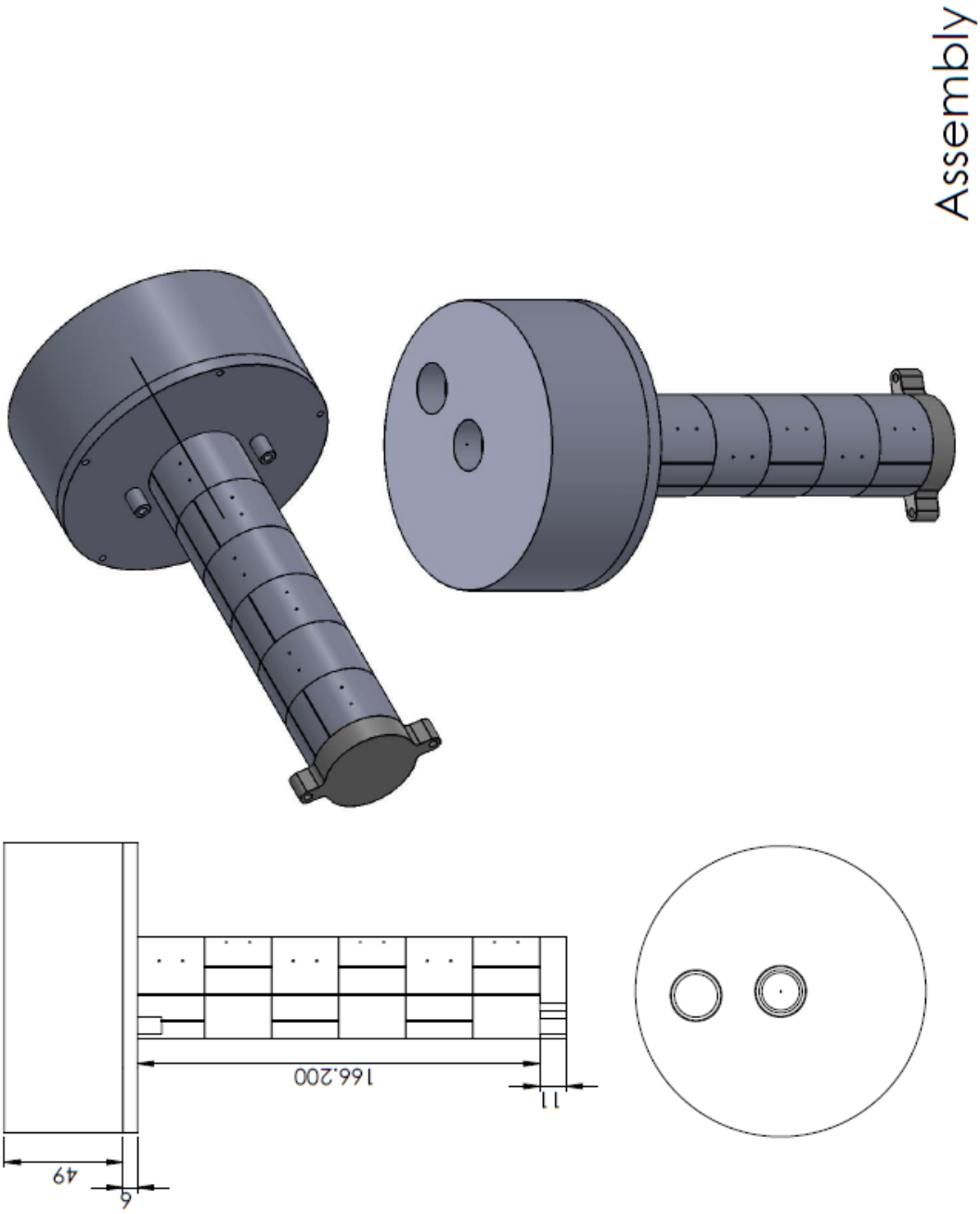

Figure 11: Assembly of absorber tube for experimental validation. All units in mm. Assembly consist of inlet/outlet port, inlet/outlet port cap, 6 interior segments and a turn segment. Two ANSI 10-24 threaded rods connect the inlet/outlet port cap to the turn segment. Axial etchings in the interior segments aid in segment alignment. Pictured here is strip fin alignment. Absorber tube is made of Al-6061.

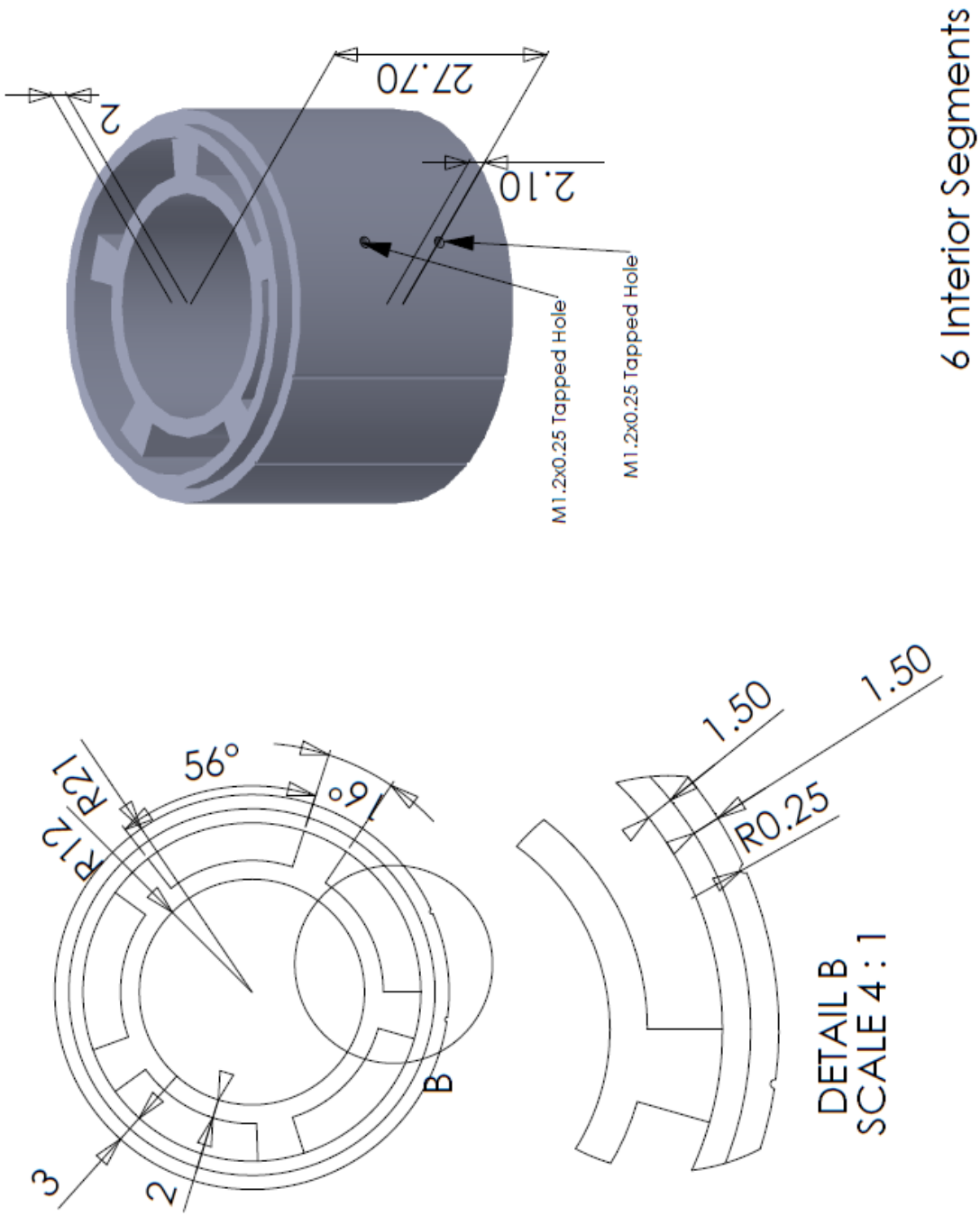

Figure 12: Interior Segment. Six interior segments are used in the assembly. All dimensions are in mm. Detail B shows the axial etchings above the center of a fin and the center of the adjacent cavity. These etchings are used for segment alignment. The tapped holes are for the insertion of thermocouples to collect data on the inner wall temperature. Material used is Al-6061.

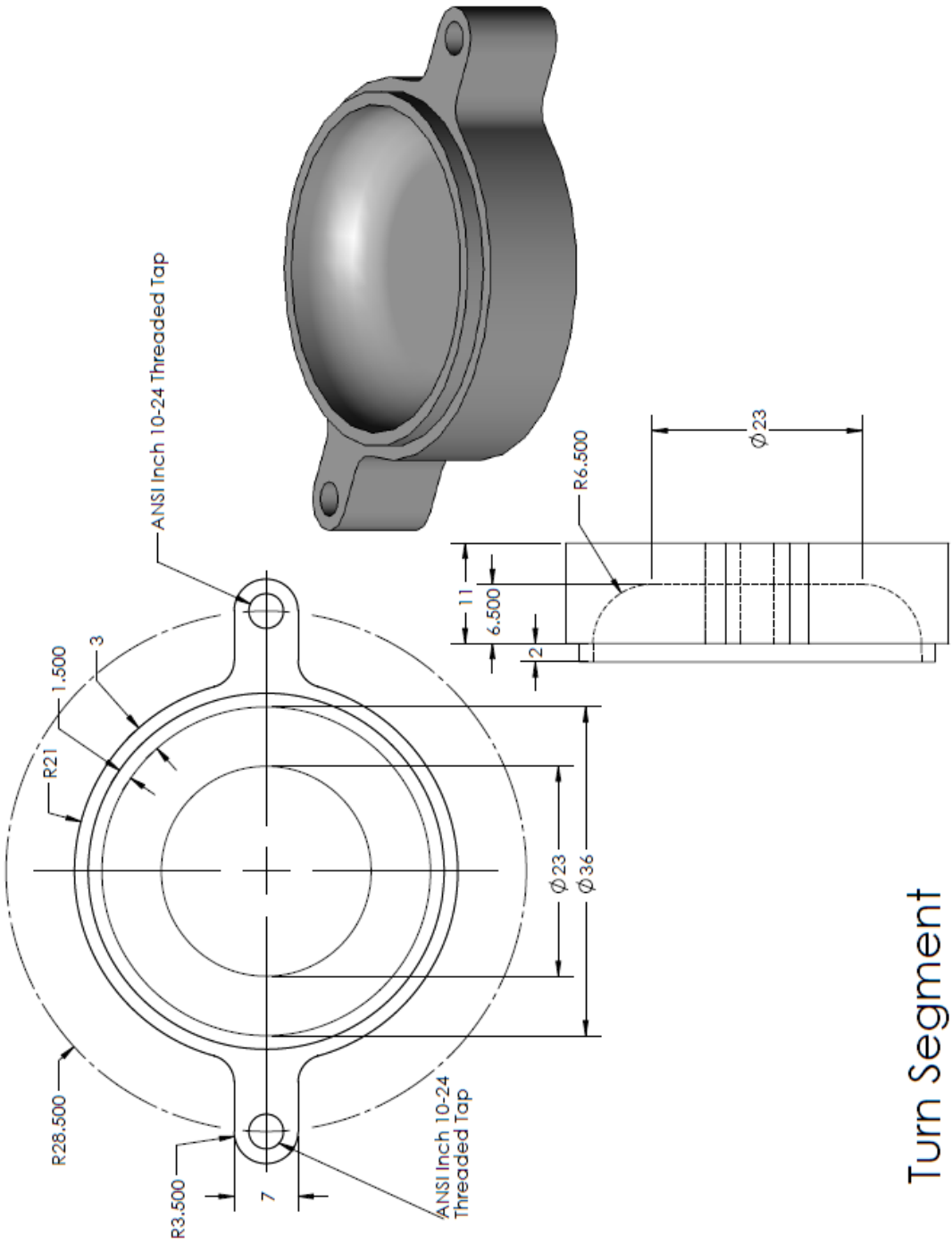

Figure 13: Turn Segment. All dimensions are in mm unless otherwise indicated. The threaded tapped holes allow for the threaded rod to connect to the inlet/outlet port cap. The lip fits into the groove of the adjacent interior segment with Teflon in between to reduce leaks. The material used is Al-6061.

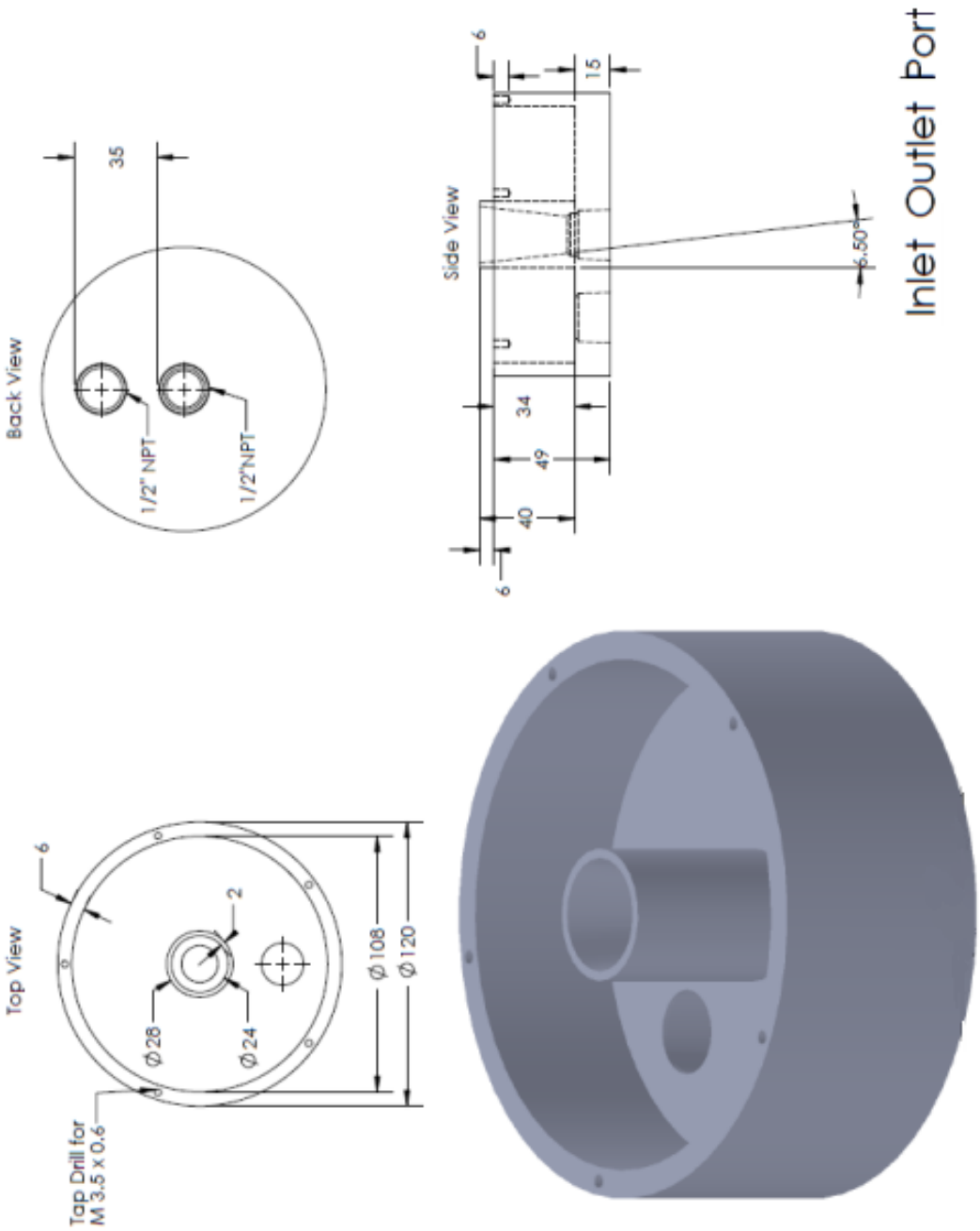

Figure 14: Inlet/Outlet Port. Units are in mm unless otherwise indicated. Compression fitted connectors are used to connect the tubing into the ½" NPT holes. When the flow direction is changed, the port remains the same and only the tubing is changed. The material used is Al-6061.

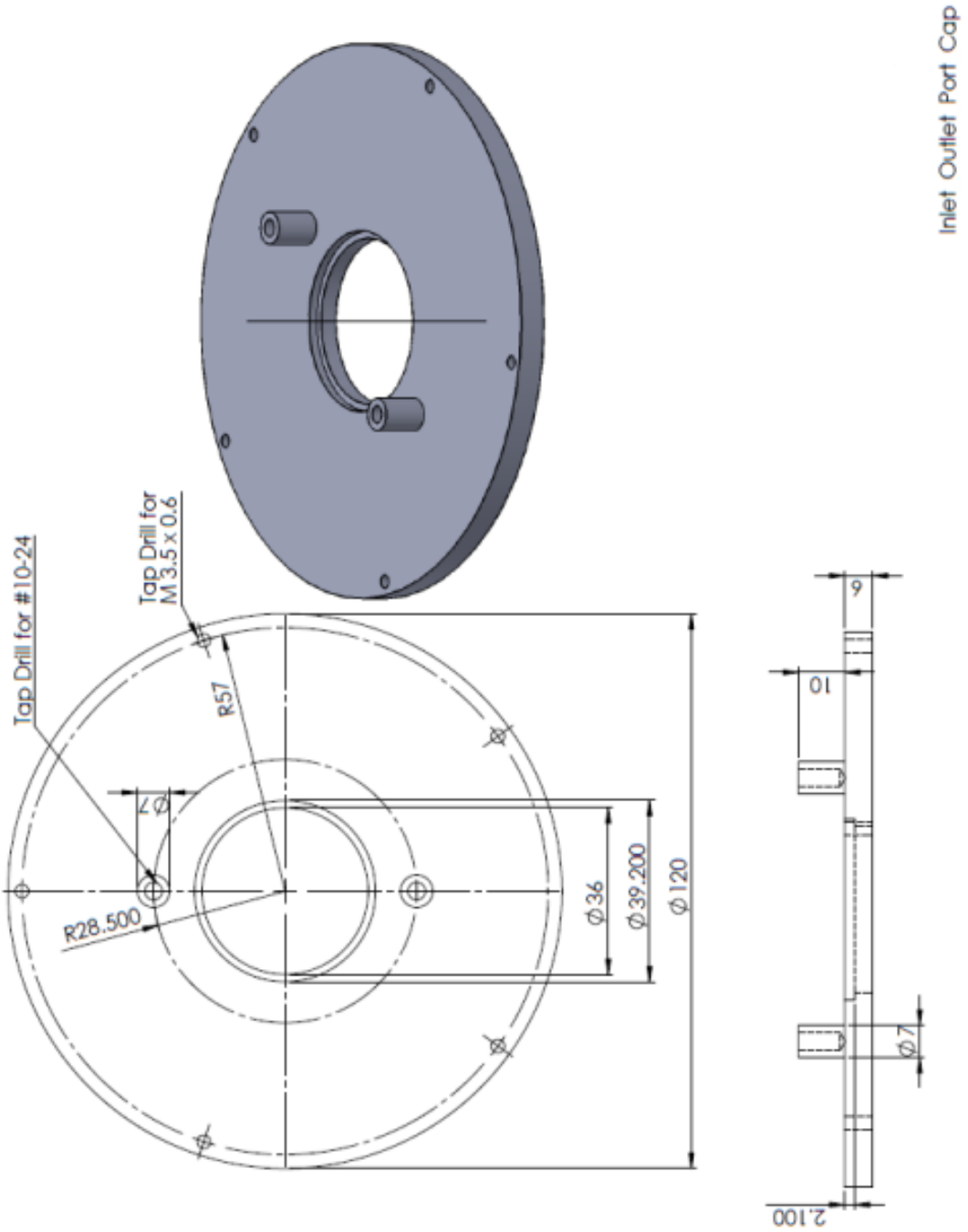

Figure 15: Inlet/Oulet Port Cap. All dimensions are in mm unless otherwise indicated. The cap is screwed into the inlet/outlet port piece with gasket sealant to ensure a leak-free fit. Teflon is used to provide leak resistance between the cap and the adjacent interior segment. Teflon is used because the inlet segments are rotated to different alignments for experimentation; whereas, gasket sealant is used to connect pieces that are fixed. The material used is Al-6061.

Experimental Set Up

Fig. 16 shows the experimental set-up used to test the fabricated dual chamber absorber tube. A 2-L flask was filled halfway with water to serve as a reservoir. A flask was chosen over a beaker since the narrow opening reduced water losses from evaporation. Despite this, periodically more water would be added to maintain the reservoir at 1-L. 1/8" inner diameter thick plastic tubing was used to extract water from the reservoir to the pump. A Medium Flow Variable-Flow Peristalic Pump from Fisher Scientific was selected for its moderate cost and range of mass flow rates. As a parastilic pump, the flow rate was intrinsically irregular. To mitigate this, customer support from Fisher Scientific suggested coiling about a meter of tubing prior to flow application. This was done prior to entering a Cole-Parmer 150-mm Correlated Flowmeter, Aluminum with 316 SS float. The flow meter read a steady flow rate.

After leaving the flow meter, the flow would enter a brass T-junction compression fitting connecting the plastic tubing to the inlet port of the fabricated absorber tube. The perpendicular insert of the T-junction embedded a K-NPT-G-72 Omega thermocouple into fluid, providing the inlet fluid temperature into the absorber tube. Depending on the flow direction, the T-junction would be connected to either the outer chamber or inner chamber of the inlet/outlet port. The Inlet/Outlet port cap was secured to the Inlet/outlet port with Form A gasket sealant from Permatex. The fluid would then travel through the inlet/outlet port segment and the flow would become radially uniform. Then, the fluid would travel through the interior segments and turn 180^0 at the end of the absorber tube. The flow would then return in the opposite chamber and exit through the other port. Upon exiting the absorber tube, the vapor would pass through an identical brass T-junction with another K-NPT-G-72 Omega thermocouple acquiring the fluid exit temperature. The vapor then entered a second brass T-junction with a Type 1008 Stainless Steel-Case Pressure Gage from Ashcroft and a compression fit 1/8" diameter plastic tubing. This plastic tubing was then coiled at the bottom of the reservoir allowing the vapor to heat the reservoir and partially condense before exiting the plastic tube and entering the bulk fluid in the reservoir.

The interior segments of the absorber tube were heated by the High Watt Density Duo-Tape from HTS/Amptek. The heating tape was selected for its flexibility that allowed for easy contour onto the surface of the absorber tube and the high heat flux of 13 W/in^2 that would allow complete vaporization under test conditions. Rigid high-temperature 2" thick fiberglass pipe insulation from McMaster-Carr was selected for insulating the absorber tube. It was selected for its low thermal conductivity (0.23 W/m^2K) and high temperature tolerance (850^0F). Unfortunately, during testing, the insulation caught on fire while in operation well below its specified limits. After speaking with the manufacturer, it was decided to use the insulation only on the inlet/outlet port and not in direct contact with the heating tape.

In addition to the two K-NPT-G-72 Omega thermocouples gathering inlet and outlet fluid temperatures, 19 GG-K-36-SLE-50 Omega thermocouples were place on the absorber tube walls. 9 of these thermocouples were attached to the inner wall via small 1.2 mm diameter holes through the fins. A portion of the outer sleeve of the 9 interior thermocouples was removed so that the thermocouple could fit through the hole. The remaining 10 thermocouples were attached to the outer wall of the absorber tube, of which 5 were attached on the outer

wall above a fin and the other 5 were attached on the outer wall above a cavity. The thermocouples were attached to the walls using Omegabond 400. Omegabond 400 was selected for its high temperature resistance (2600^{o}F) and high thermal conductivity (11 Btu-in/sq.ft./hr/^{o}F). All 19 thermocouples were arc welded by Sara Beaini.

All of the thermocouples attached to the absorber tube walls were connected to a 20 position 2-pole silver plated make-before-break rotary switch from Omega. This rotary switch would allow one thermocouple reading to enter the 4-channel NI 9211 DAQ board from National Instruments. Two of the remaining channels of the DAQ connected to the inlet and outlet fluid temperature thermocouples. The last channel on the DAQ connected to a thermocouple gathering room temperature data.

Experimental Protocol

The following procedure was used to gather experimental data.

1. Turn on pump to desired mass flow rate and check for leaks.
2. Plug in heating tape.
3. Allow system to reach steady state. This would typically take about 2 hours.
4. Record one minute of temperature data at an interval of one second for each thermocouple using the rotary switch to change the thermocouple of interest being connected to the DAQ board.
5. After having gone through all the thermocouples, repeat Step 5 for the first four thermocouples analyzed to confirm that the system is at steady state.

Experimental Uncertainty

An uncertainty analysis was completed using the Journal of Heat Transfer Policy on Reporting Uncertainties in Experimental Measurements and Results (Kim, Simon, & Viskanta, 1993) for uncertainty in both the temperature and mass flow rate. The uncertainty, *U*, is defined by the following equation where *B* is the bias limit and *Prec* is the precision limit.

$$U = \sqrt{B^2 + Prec^2} \tag{94}$$

To determine the uncertainty in the temperature measurements, thermocouples were placed in boiling water. The DAQ board collected data at 15 second intervals obtaining a total of 334 samples. The average temperature of these samples was 100.0834^{o}C, showing a bias limit of 0.0834^{o}C. 90% of the data fell within +/- 0.9^{o}C of the average temperature. Therefore, the precision limit was 0.9^{o}C. The uncertainty in temperature was calculated based on Eqn. 94 to be 0.904. Based on significant figures, it is reasonable to consider the uncertainty in temperature measurements to be +/- 1^{o}C.

To determine the uncertainty in the mass flow rate measurements, the water discharged from the pump was weighed at one minute time intervals at a flow meter reading of 0.169 g/s. Thirty samples were collected. The average mass flow rate of the samples was 0.1587 g/s, showing a bias limit of 0.0103 g/s. 90% of the data was within 0.03 g/s of the average, showing a precision limit of 0.03 g/s. Based on Eqn. 94, the uncertainty in the mass flow rate was calculated to be 3 x10^{-5} kg/s.

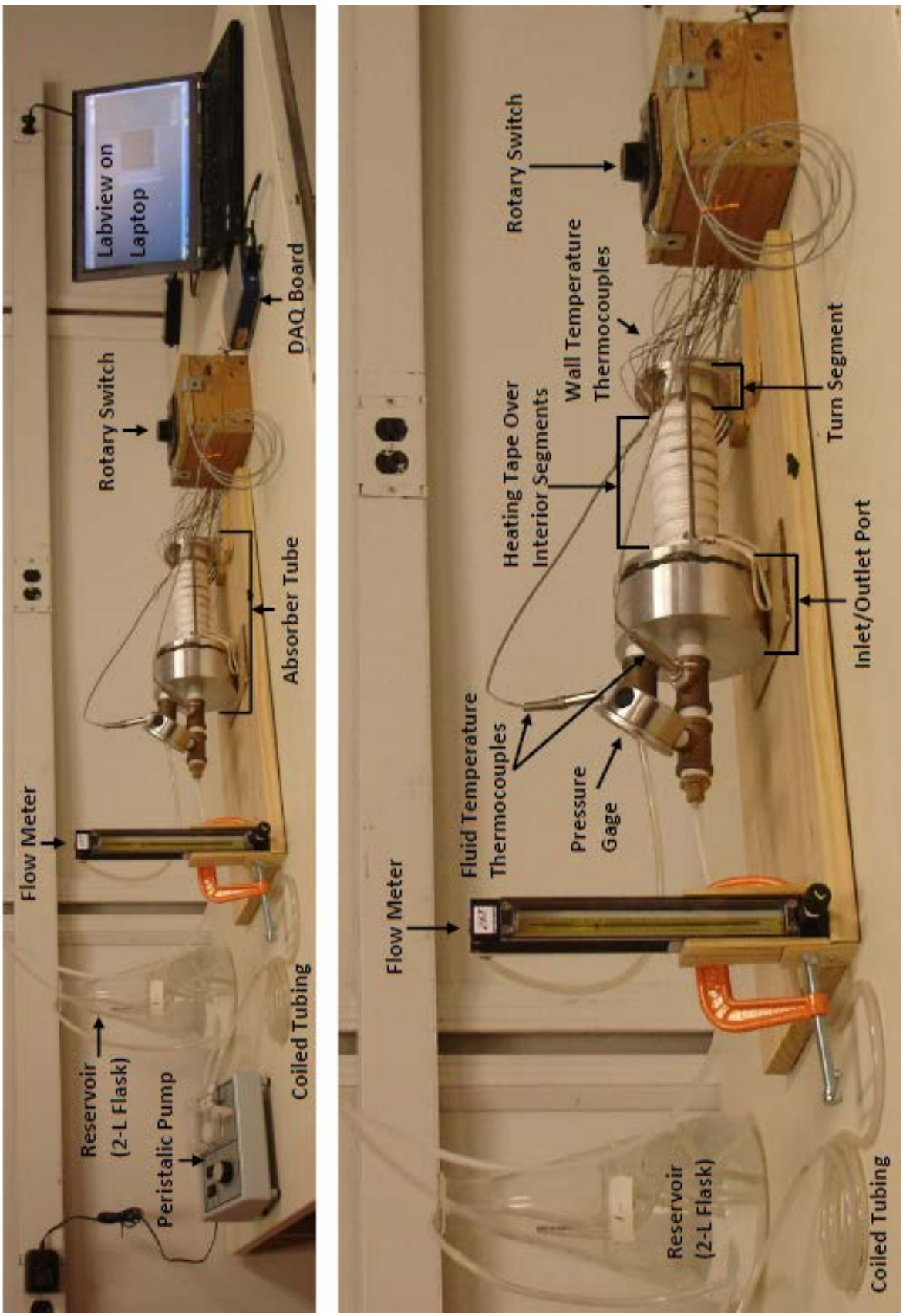

Figure 16: Experimental Set-Up

Experimental Validation of Analytical Model

In order to compare the experimental results and the analytical model, the percent difference has been defined as follows:

$$Percent\ Difference = \frac{|Experimental\ Result - Theoretical\ Prediction|}{Experimental\ Result} \quad (95)$$

Dual Chamber Absorber Tube: Fluid Enters Inner Chamber

Variation with Mass Flow Rate

The mass flow rate was varied between 0.09 g/s and 0.25 g/s. This range ensured that the pump did not stall and that the fluid exiting the absorber tube was entirely vapor. All tests were performed at atmospheric pressure. A summary of the test conditions can be seen in Table 3.

Table 3: Test Conditions For Fluid Entering Inner Chamber

Mass Flow Rate (g/s)	Fin Alignment	Inlet Fluid Temperature (C)	Exit Fluid Temperature (C)	Ambient Temperature (C)
0.09	Offset	72.9	100.5	25.1
0.17	Offset	71.0	100.4	24.9
0.17	Aligned	93.7	100.1	26.9
0.22	Offset	72.8	100.5	26.4
0.25	Offset	73.8	100.5	27.3
0.25	Aligned	91.8	100.1	26.7

In the following plots, the experimentally obtained data is compared the theoretical values from the computational model. The size of the experimental data markers and error bars show the uncertainty in the temperature based on the analysis done in the section titled "Experimental Uncertainty." The uncertainty in the inlet and exit fluid temperatures and the mass flow rate affected input parameters into the computational model. To account for this uncertainty, several iterations of the computational model were run modifying each parameter based on uncertainty until all permutations were achieved. The maximum and minimum theoretical temperature profiles were plotted. For all plots in this section, the segments were positioned to allow strip fin alignment in the outer chamber.

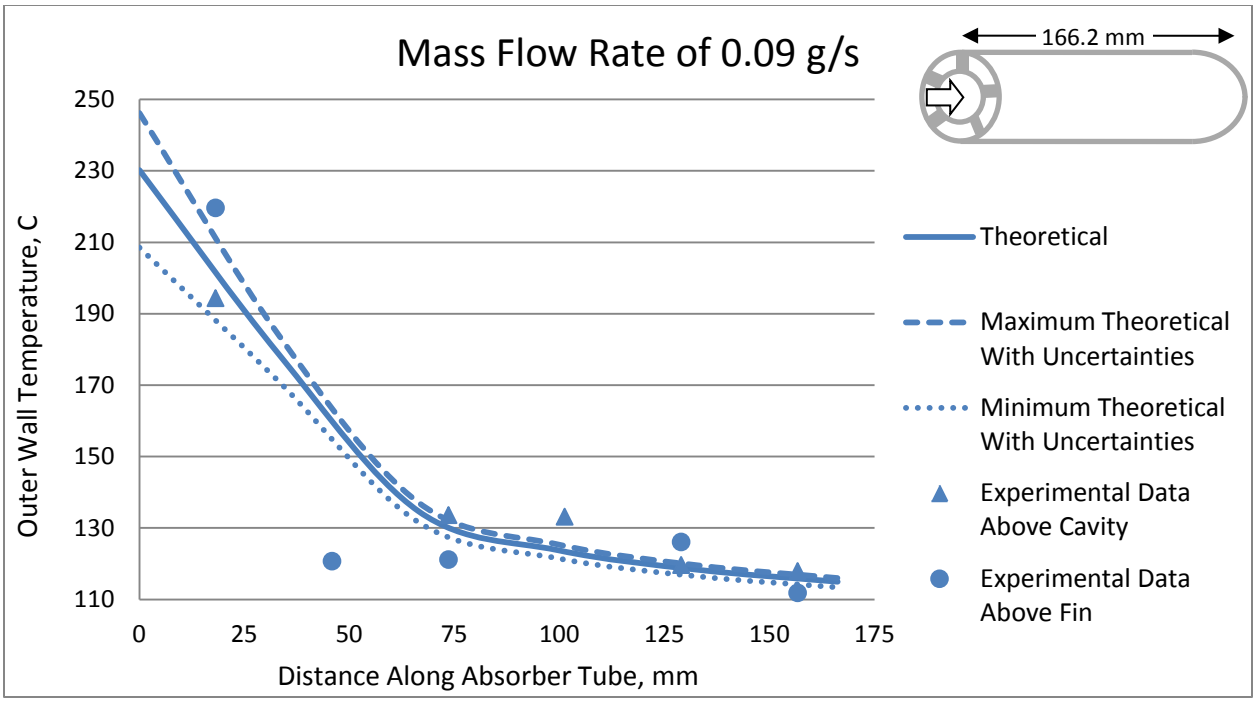

Figure 17: Experimental outer wall temperature compared to computational theoretical values. Water enters the inner chamber at 0.09 g/s at 72.9C and leaves the outer chamber at 100.5C. Strip fin alignment in outer chamber. Uncertainty in mass flow rate and inlet and outlet fluid temperatures creates uncertainty in computational model as shown by the dotted and dashed curves. Uncertainty in the thermocouples attached to the outer wall is half the height of the experimental data markers. The ambient temperature is 25.1C. The inlet pressure is 1 atm.

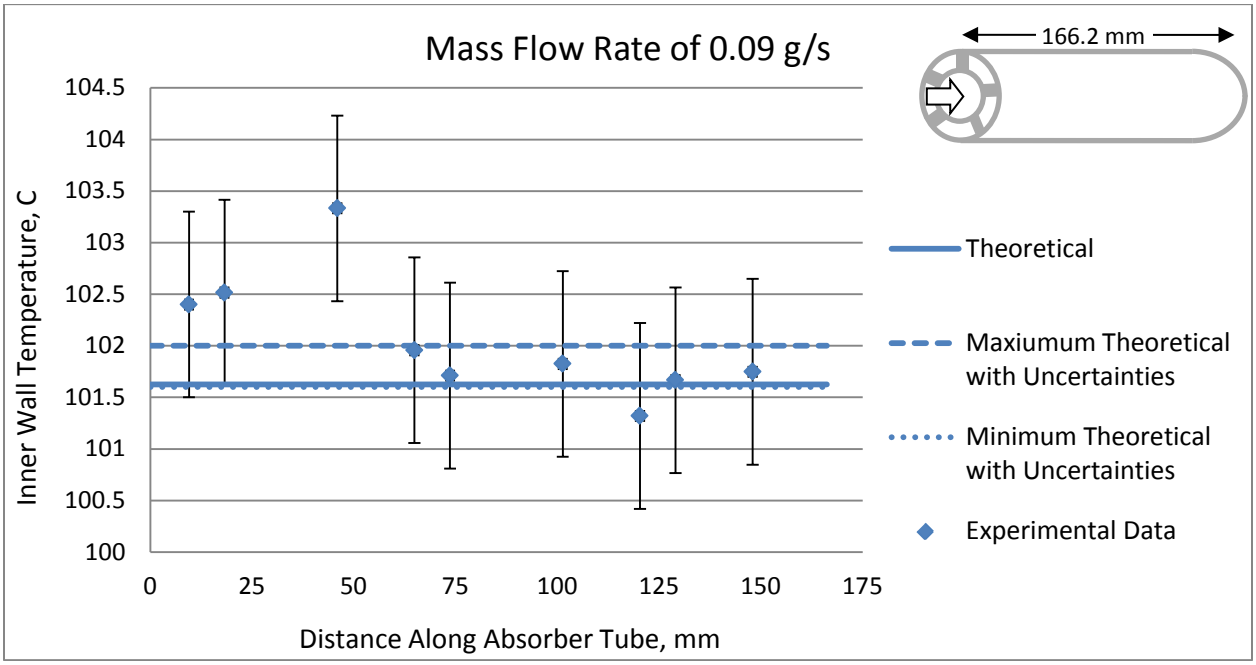

Figure 18: Experimental inner wall temperature compared to computational theoretical value. Water enters the inner chamber at 0.09 g/s at 72.9C and leaves the outer chamber at 100.5C. Strip fin alignment in outer chamber. Uncertainty in mass flow rate and inlet and outlet fluid temperatures creates uncertainty in computational model as shown by the dotted and dashed curves. Uncertainty in the thermocouples attached to the inner wall is shown by error bars. The ambient temperature is 25.1C. The inlet pressure is 1 atm.

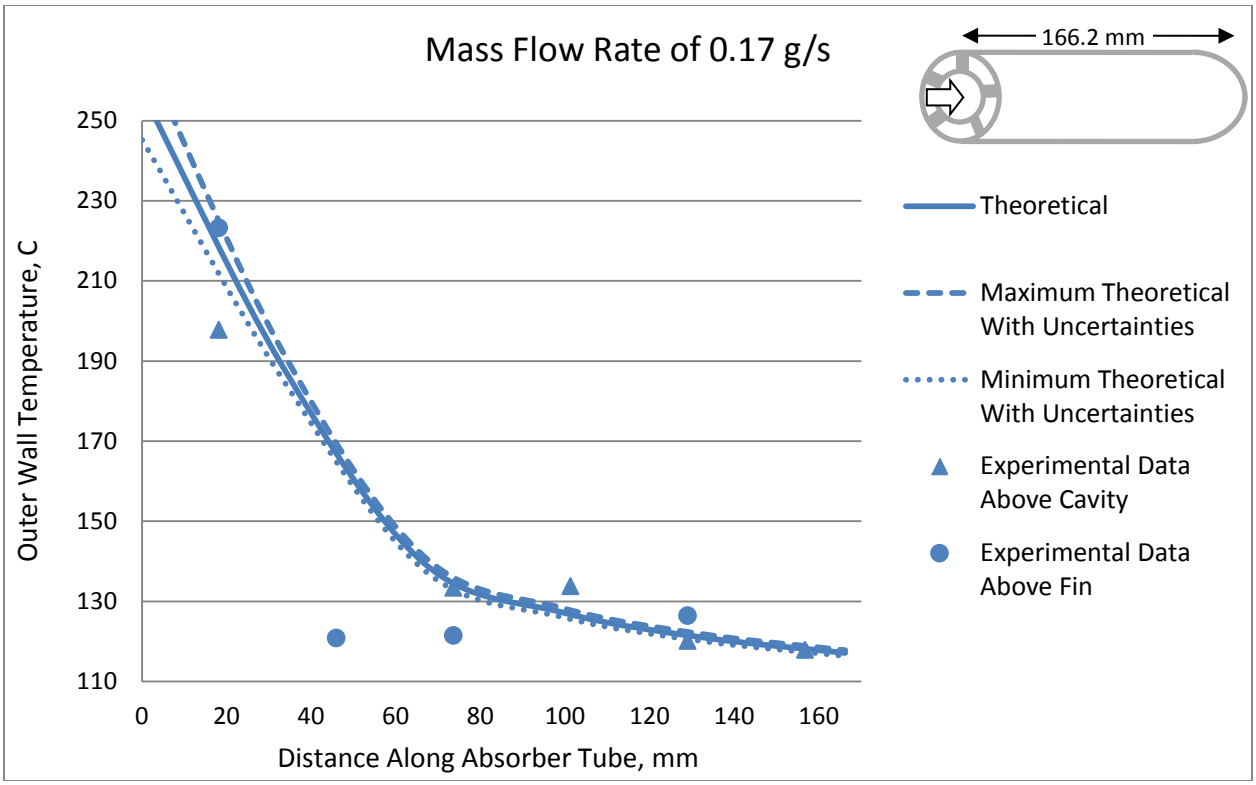

Figure 19: Experimental outer wall temperature compared to computational theoretical values. Water enters the inner chamber at 0.17 g/s at 71.0C and leaves the outer chamber at 100.4C. Strip fin alignment in outer chamber. Uncertainty in mass flow rate and inlet and outlet fluid temperatures creates uncertainty in computational model as shown by the dotted and dashed curves. Uncertainty in the thermocouples attached to the outer wall is half the height of the experimental data markers. The ambient temperature is 24.9C. The inlet pressure is 1 atm.

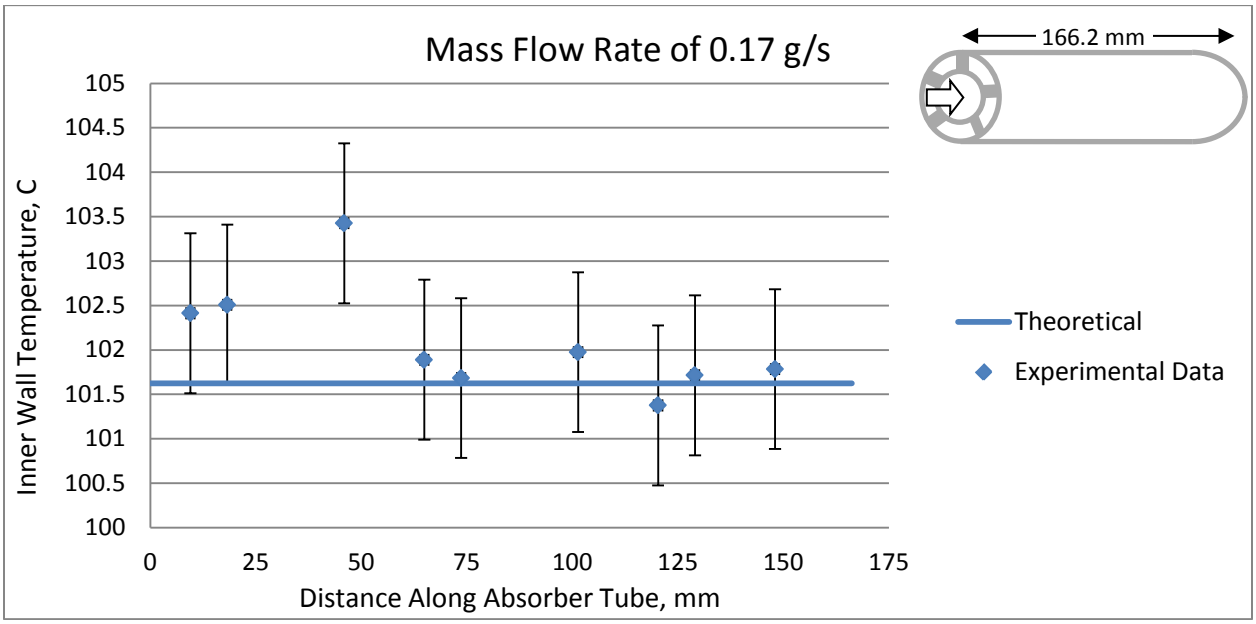

Figure 20: Experimental inner wall temperature compared to computational theoretical value. Water enters the inner chamber at 0.17 g/s at 71.0C and leaves the outer chamber at 100.4C. Strip fin alignment in outer chamber. Uncertainty in mass flow rate and inlet and outlet fluid temperatures yielded the same results as the theoretical model without the uncertainties. Uncertainty in the thermocouples attached to the inner wall is shown by error bars. The ambient temperature is 24.9C. The inlet pressure is 1 atm.

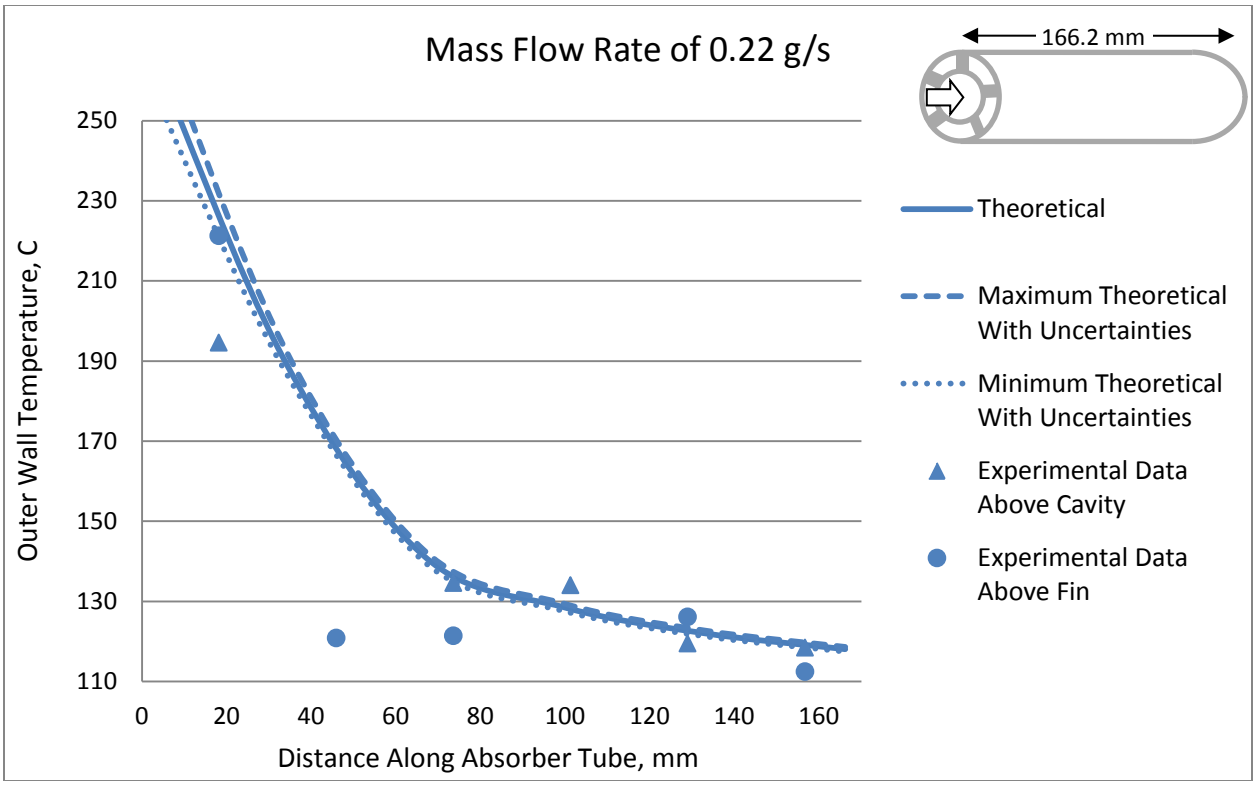

Figure 21: Experimental outer wall temperature compared to computational theoretical values. Water enters the inner chamber at 0.22 g/s at 72.8C and leaves the outer chamber at 100.5C. Strip fin alignment in outer chamber. Uncertainty in mass flow rate and inlet and outlet fluid temperatures creates uncertainty in computational model as shown by the dotted and dashed curves. Uncertainty in the thermocouples attached to the outer wall is half the height of the experimental data markers. The ambient temperature is 26.4C. The inlet pressure is 1 atm.

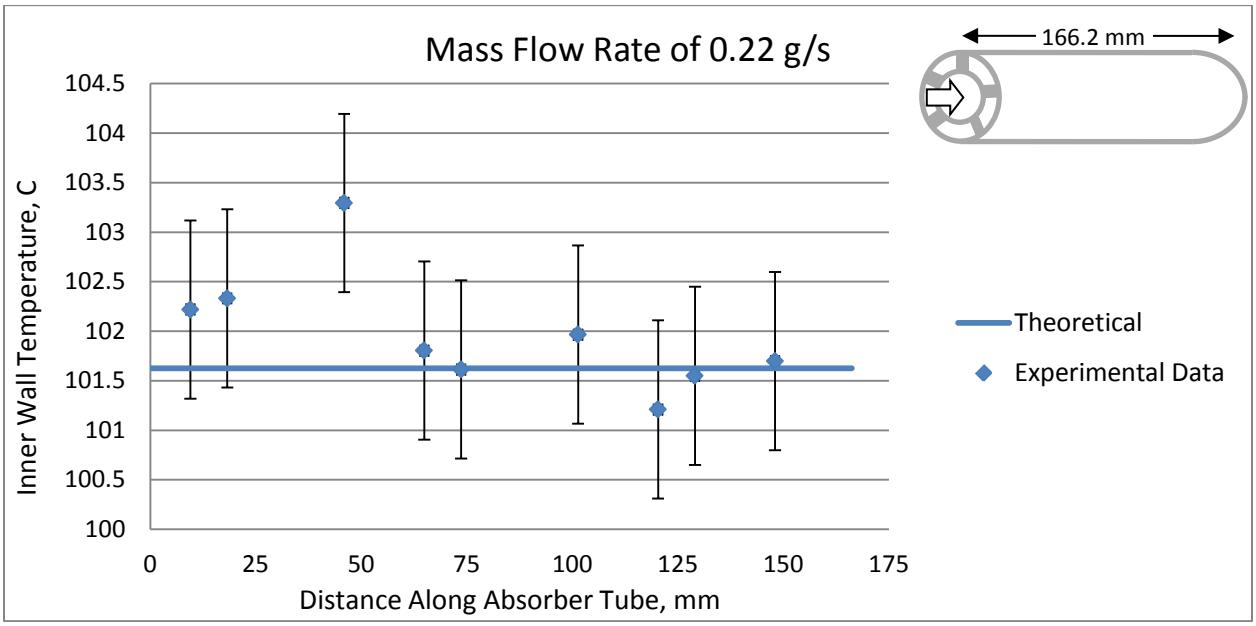

Figure 22: Experimental inner wall temperature compared to computational theoretical value. Water enters the inner chamber at 0.22 g/s at 72.8C and leaves the outer chamber at 100.5C. Strip fin alignment in outer chamber. Uncertainty in mass flow rate and inlet and outlet fluid temperatures yielded the same results as the theoretical model without the uncertainties. Uncertainty in the thermocouples attached to the inner wall is shown by error bars. The ambient temperature is 26.4C. The inlet pressure is 1 atm.

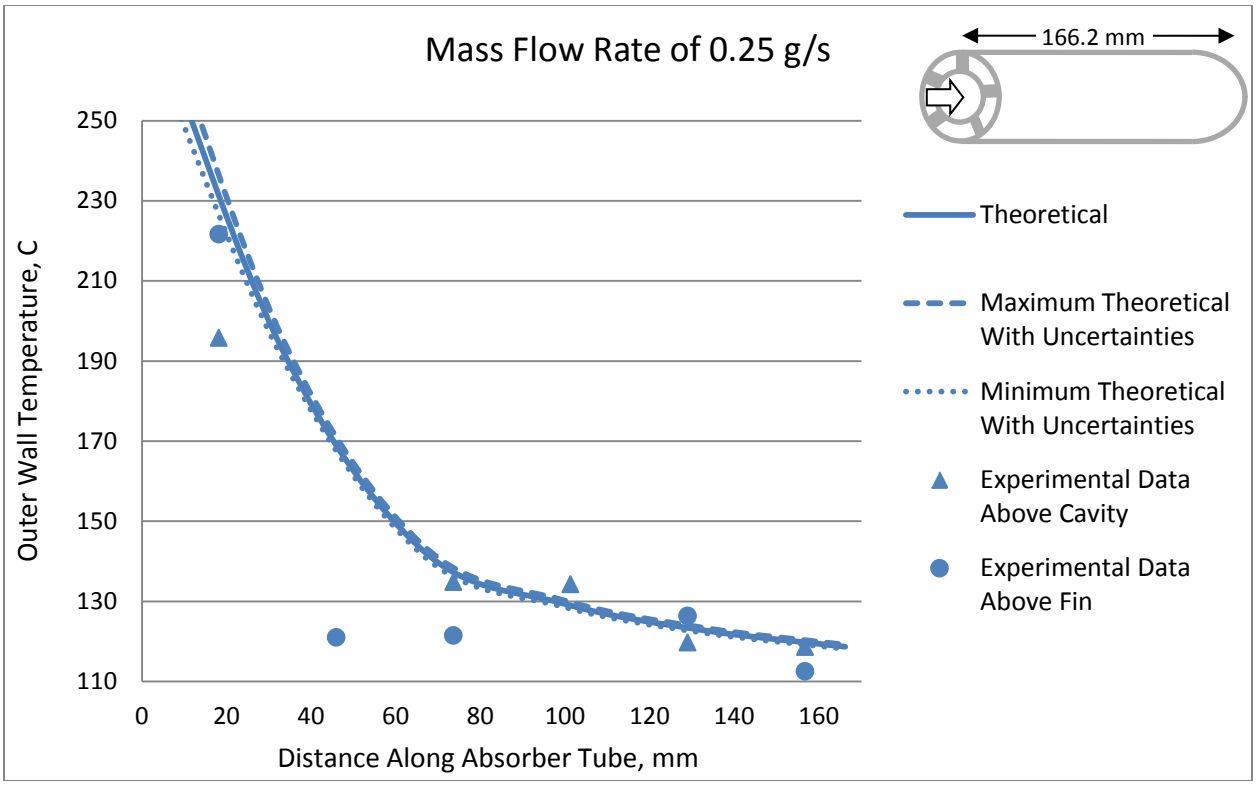

Figure 23: Experimental outer wall temperature compared to computational theoretical values. Water enters the inner chamber at 0.25 g/s at 73.8C and leaves the outer chamber at 100.5C. Strip fin alignment in outer chamber. Uncertainty in mass flow rate and inlet and outlet fluid temperatures creates uncertainty in computational model as shown by the dotted and dashed curves. Uncertainty in the thermocouples attached to the outer wall is half the height of the experimental data markers. The ambient temperature is 27.3C. The inlet pressure is 1 atm.

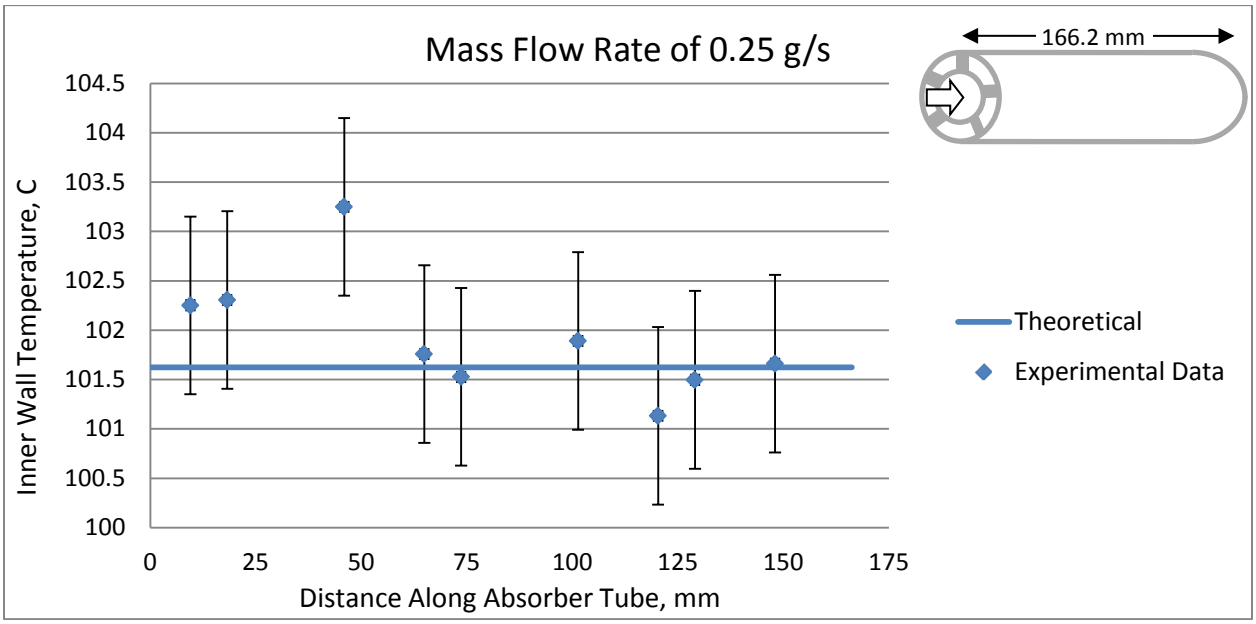

Figure 24: Experimental inner wall temperature compared to computational theoretical value. Water enters the inner chamber at 0.25 g/s at 73.8C and leaves the outer chamber at 100.5C. Strip fin alignment in outer chamber. Uncertainty in mass flow rate and inlet and outlet fluid temperatures yielded the same results as the theoretical model without the uncertainties. Uncertainty in the thermocouples attached to the inner wall is shown by error bars. The ambient temperature is 27.3C. The inlet pressure is 1 atm.

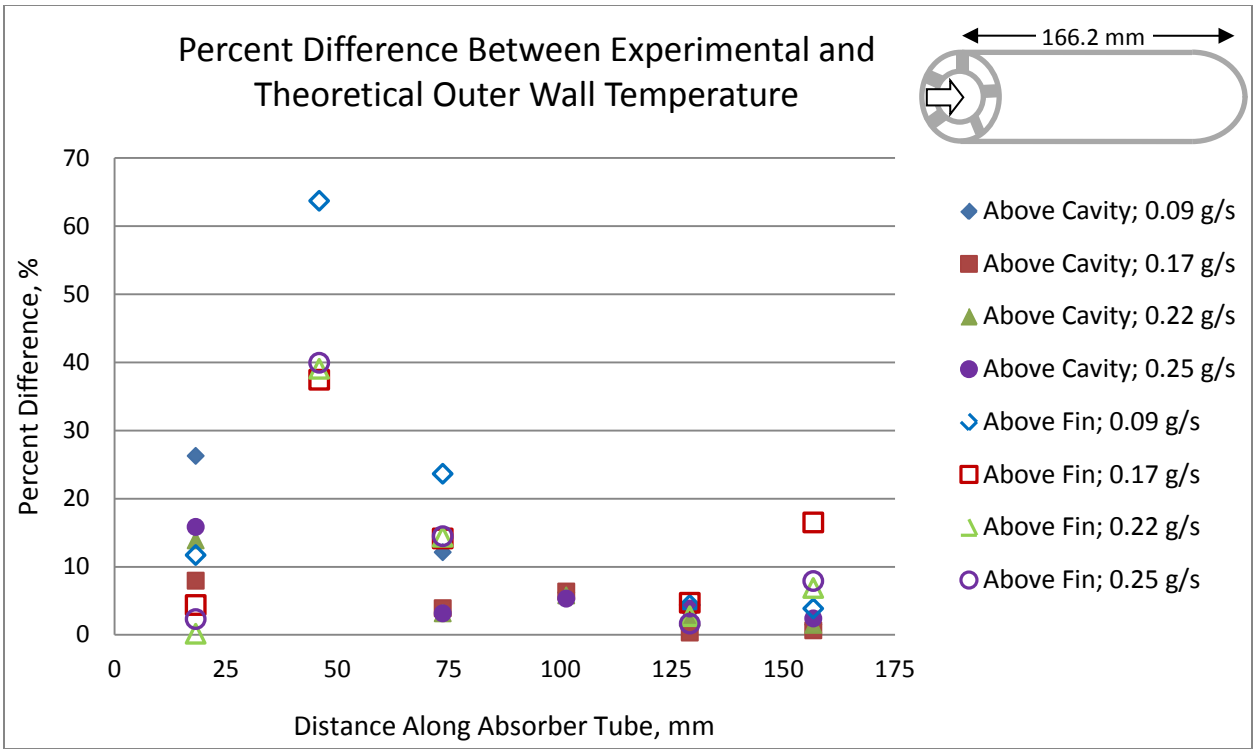

Figure 25: Percent difference between experimental and theoretical outer wall temperature along the absorber tube for all tested mass flow rates. The filled markers represent outer wall temperature data for a region above a cavity. The unfilled markers represent the outer wall temperature data for a region above a fin. Fluid enters the inner chamber first. Strip fin alignment in the outer chamber. Test conditions presented in Table 3.

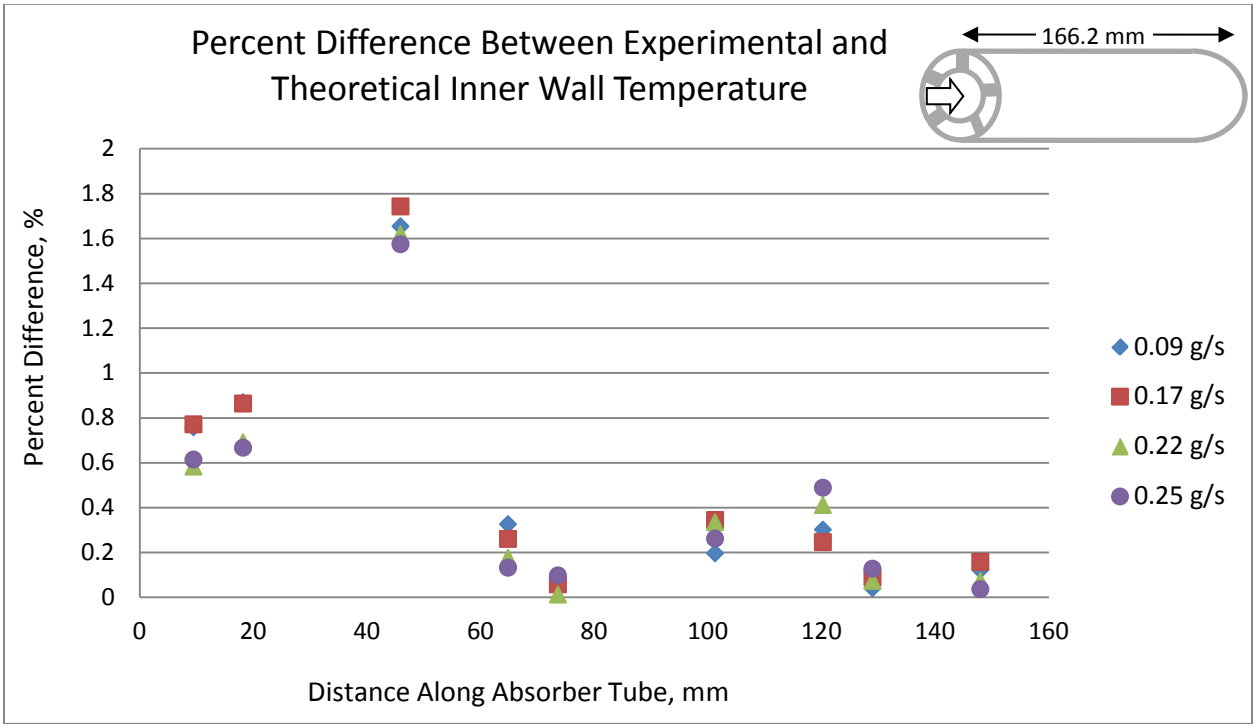

Figure 26: Percent difference between experimental and theoretical inner wall temperature along the absorber tube for all tested mass flow rates. Fluid enters the inner chamber first. Strip fin alignment in the outer chamber. Test conditions presented in Table 3.

Overall there appears to be very good agreement between the computational model and the experimental data as seen in Figs. 17 – 26. For all mass flow rates studied, there is particularly strong agreement for the inner wall temperature with a percent difference of less than 2%. Water enters the inner chamber as a subcooled liquid. Single phase subcooled heating and two phase saturated boiling with qualities below 0.2 occur in the inner chamber as seen if Fig. 50 in section "Discussion of Absorber Tube Results". The saturated boiling process dominates the inner chamber and the inner chamber wall is held at an almost constant 2 degree wall superheat as is confirmed by experimental data.

Conversely, the outer wall temperature shows moderate agreement between the computational and experimental data. 90% of all experimental data for the temperature of the outer wall agrees within 30% to the computational model. 82.5% of the experimental data agrees within 16%. It is important to realize that there are inherent limitations to the accuracy of the computational model. The computational model used relies heavily on the Kandlikar model for saturated boiling, which was found to agree with water data to a mean deviation of 16% (Kandlikar, 1991). Hence, the accuracy of the outer wall temperature is more or less as would be expected. There are a few data points when the difference between the computational model and experimental data of the outer wall temperature is greater than 30%. This occurs at places along the absorber tube that experience high quality saturated boiling (qualities greater than 0.7). Please see Fig. 50 in the section titled "Discussion of Absorber Tube Results." It is important to note that at qualities greater than 0.7 the Kandlikar model (Kandlikar, 1991) is no longer valid. To account for this, linear interpolation based on quality was used for qualities greater than 0.7. Although the linear behavior of the average heat transfer coefficient is observed by other scientists (Marseille, Carey, & Estergreen, 1988), the irregularity and shredding of liquid droplet make the local heat transfer coefficient in this region difficult to predict.

Variation with Fin Alignment

Offset strip fin compact heat exchangers are a popular design configuration to increase the heat transfer coefficient. Manglik and Bergles (Manglik & Bergles, 1995) provide a thorough literature review on offset-strip fins. Offset strip fins force the boundary layer to restart, thus, reducing the average boundary layer thickness. In order to test the benefit of using offset strip fins, two experimental configurations were compared at two mass flow rates (0.17 g/s and 0.25 g/s). In the first configuration, the fins in the outer chamber are aligned. In the second configuration, the segments are rotated so that the fin offset is uniform and equal to half the fin spacing. Fig. 1 shows the offset fin configuration.

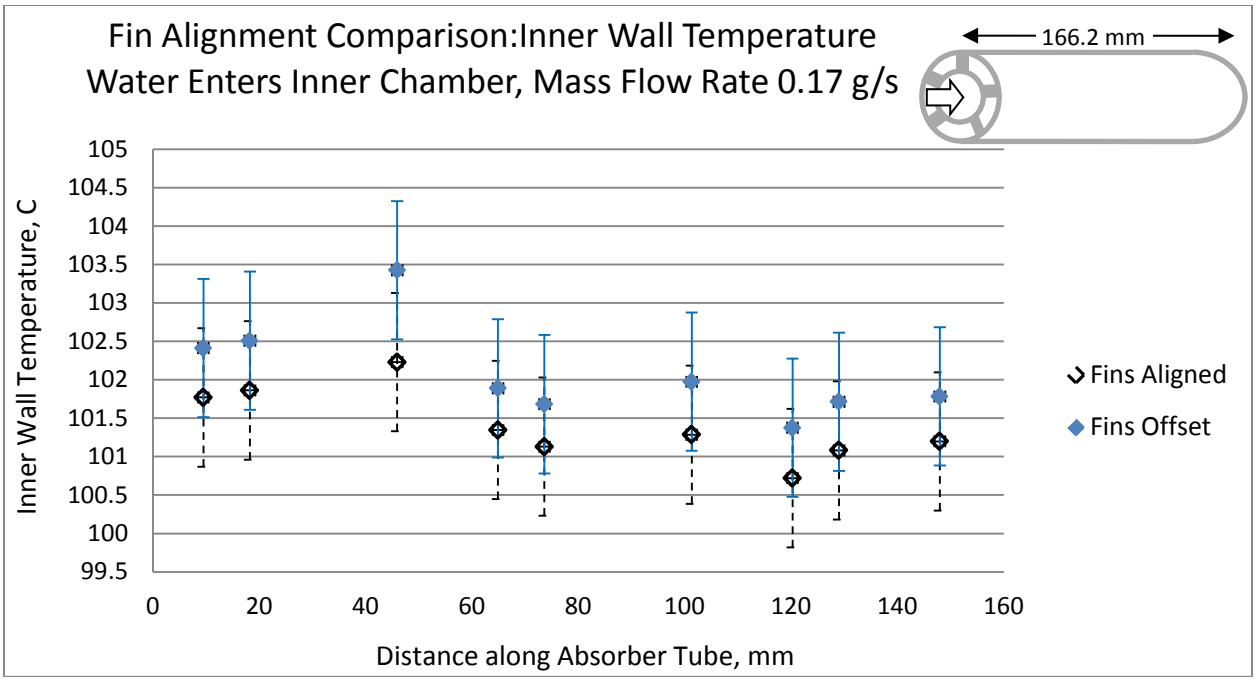

Figure 27: Experimental data of inner wall temperature for two outer chamber fin configurations: aligned and offset. Water enters the inner chamber at 0.17 g/s. For the aligned fin configuration, water enters the absorber tube at 93.7C and exits at 100.1C with an ambient temperature of 26.9C. For the strip fin configuration, water enters the absorber tube at 71.0C and exits at 100.4C with an ambient temperature of 24.9C. Uncertainty in the thermocouples attached to the inner wall is shown by solid blue error bars for offset fins and dashed black error bars for aligned fins. The pressure at the inlet is 1 atm.

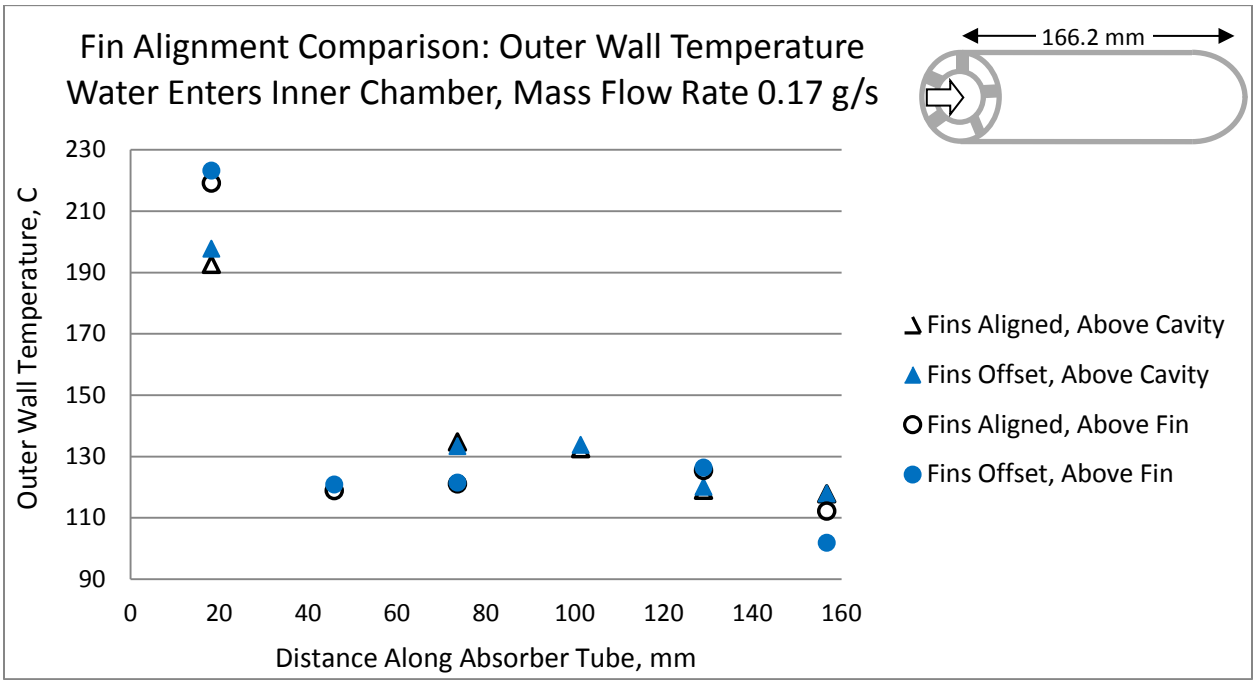

Figure 28: Experimental data of outer wall temperature for two outer chamber fin configurations: aligned and offset. Water enters the inner chamber at 0.17 g/s. For the aligned fin configuration, water enters the absorber tube at 93.7C and exits at 100.1C with an ambient temperature of 26.9C. For the strip fin configuration, water enters the absorber tube at 71.0C and exits at 100.4C with an ambient temperature of 24.9C. Uncertainty in the thermocouples attached to the outer wall is half the height of the experimental data markers. The pressure at the inlet is 1 atm.

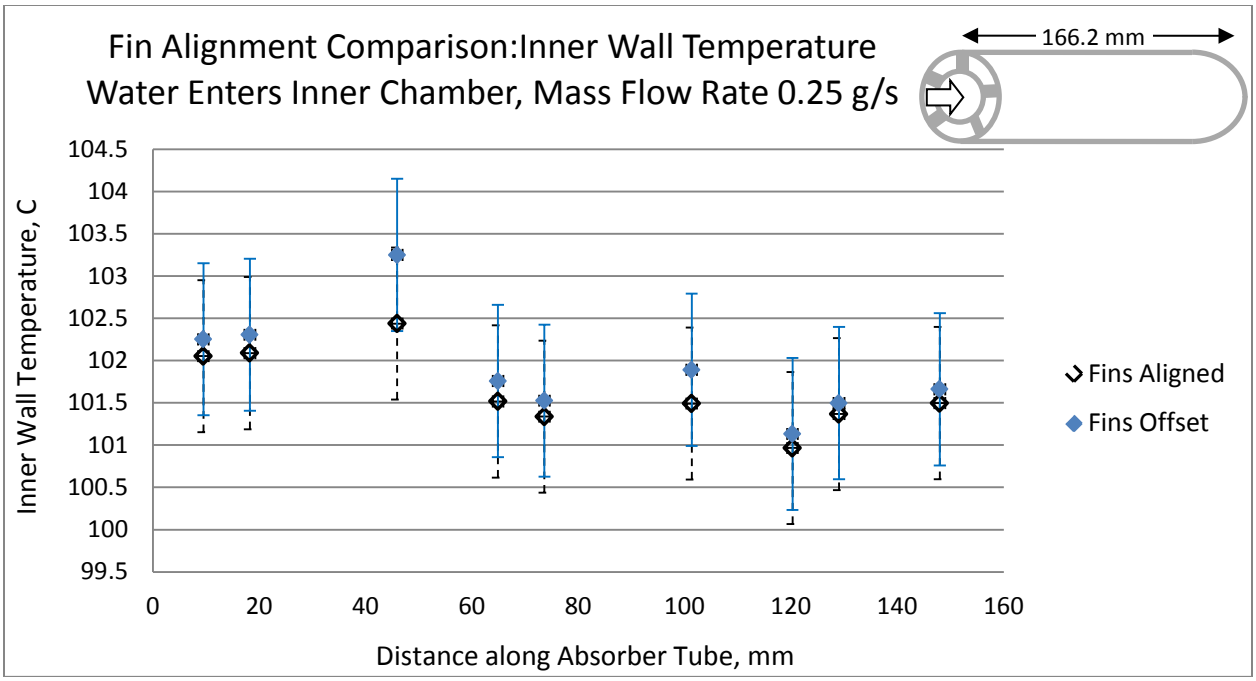

Figure 29: Experimental data of inner wall temperature for two outer chamber fin configurations: aligned and offset. Water enters the inner chamber at 0.25 g/s. For the aligned fin configuration, water enters the absorber tube at 91.8C and exits at 100.1C with an ambient temperature of 26.7C. For the strip fin configuration, water enters the absorber tube at 73.8C and exits at 100.5C with an ambient temperature of 27.3C. Uncertainty in the thermocouples attached to the inner wall is shown by solid blue error bars for offset fins and dashed black error bars for aligned fins. The pressure at the inlet is 1 atm.

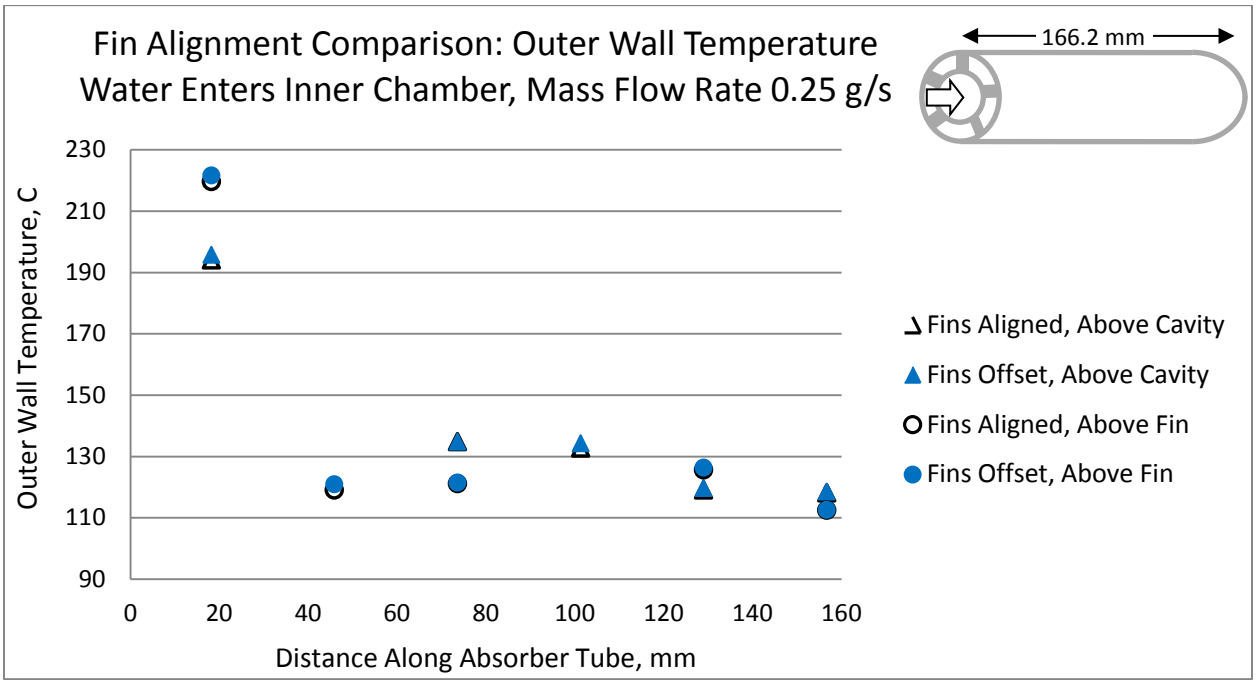

Figure 30: Experimental data of outer wall temperature for two outer chamber fin configurations: aligned and offset. Water enters the inner chamber at 0.25 g/s. For the aligned fin configuration, water enters the absorber tube at 91.8C and exits at 100.1C with an ambient temperature of 26.7C. For the strip fin configuration, water enters the absorber tube at 73.8C and exits at 100.5C with an ambient temperature of 27.3C. Uncertainty in the thermocouples attached to the outer wall is half the height of the experimental data markers. The pressure at the inlet is 1 atm.

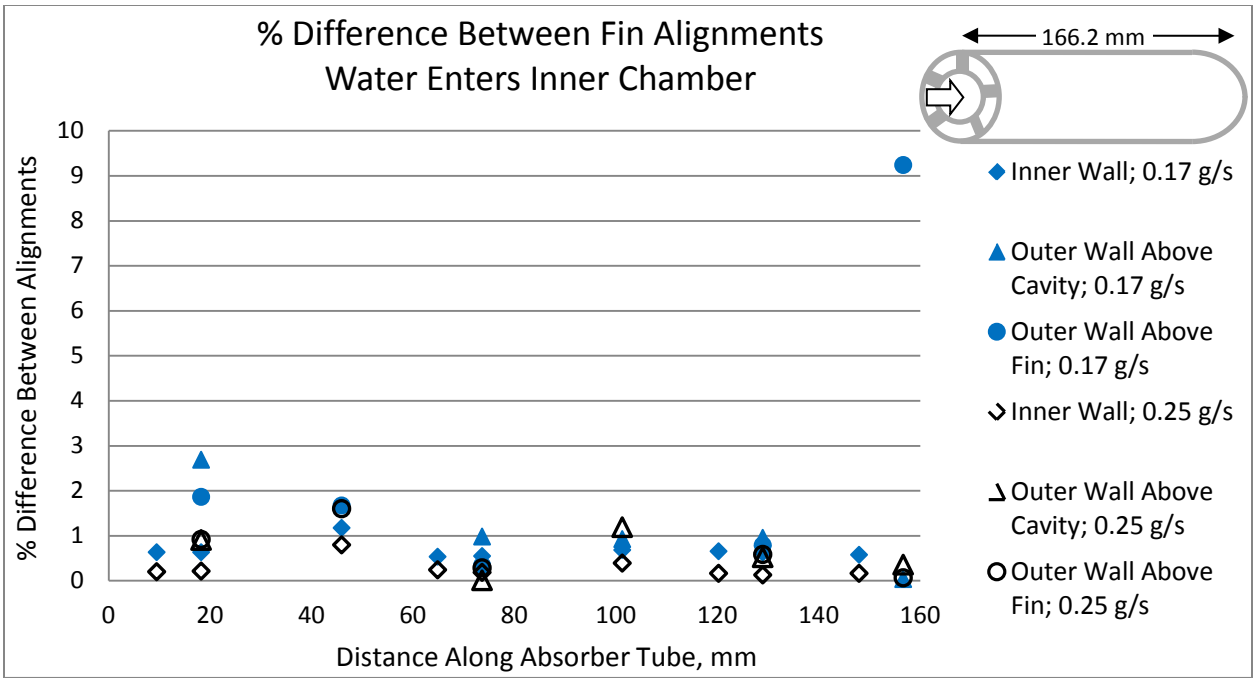

Figure 31: Percent difference between experimental data for two outer chamber fin configurations: aligned and offset. Inner and outer wall temperatures considered. Water enters the inner chamber at 0.17 g/s and 0.25 g/s. Fluid and ambient temperatures are as reported in Table 4.

In Fig. 31, 97% of the data shows less than 3% difference between wall temperatures for aligned and offset fin configurations. Additionally, Figs. 27 -30 show that difference in wall temperature is within the uncertainty of the thermocouples for all but one data point. This would suggest that there is little performance difference between the two configurations. At steady state conditions, the inlet fluid temperature that allows for complete vaporization in the absorber tube is different between the two fin configurations. With this discrepancy, some may question the results presented in Fig. 31. However, table 4 shows that despite different fluid inlet temperatures, the absorber tube in both fin configurations achieves similar heat transfer, with the offset fin alignment offering less than a 5% improvement over the aligned fin configuration. The offset fin alignment experiences increased pressure losses from form drag and increased difficulty in manufacturing.

Table 4: Heat Transfer Performance for Aligned and Offset Fin Configurations

Mass Flow Rate	Fin Alignment	Inlet Fluid Temperature (C)	Exit Fluid Temperature (C)	Ambient Temperature (C)	Heat Transfer Through Tube (W)	Improvement with Offset Fin Alignment
0.17g/s	Aligned	93.7	100.1	26.9	388.1	--
0.17g/s	Offset	71.0	100.4	24.9	404.4	4.2%
0.25g/s	Aligned	91.8	100.1	26.7	572.8	--
0.25g/s	Offset	73.8	100.5	27.3	591.9	3.3%

Dual Chamber Absorber Tube: Fluid Enters Outer Chamber

Variation with Mass Flow Rate

The mass flow rate was varied between 0.09 g/s and 0.28 g/s. This range ensured that the pump did not stall and that the fluid exiting the absorber tube was entirely vapor. In the following plots, the experimentally obtained data is compared to the theoretical values from the computational model. Uncertainty is presented similar to the plots previously presented in the section for the reverse flow. For all plots in this section, the segments were positioned to allow strip fin alignment in the outer chamber. A summary of the test conditions can be seen in Table 5.

Table 5: Test Conditions when Fluid Enters the Outer Chamber

Mass Flow Rate (g/s)	Fin Alignment	Inlet Fluid Temperature (C)	Exit Fluid Temperature (C)	Ambient Temperature (C)
0.09	Offset	85.7	100.2	29.1
0.17	Aligned	79.9	100.4	24.0
0.17	Offset	66.7	100.7	25.6
0.20	Offset	84.8	100.2	28.8
0.23	Aligned	77.9	100.4	23.6
0.23	Offset	66.5	100.7	25.2
0.28	Offset	65.5	100.8	25.1

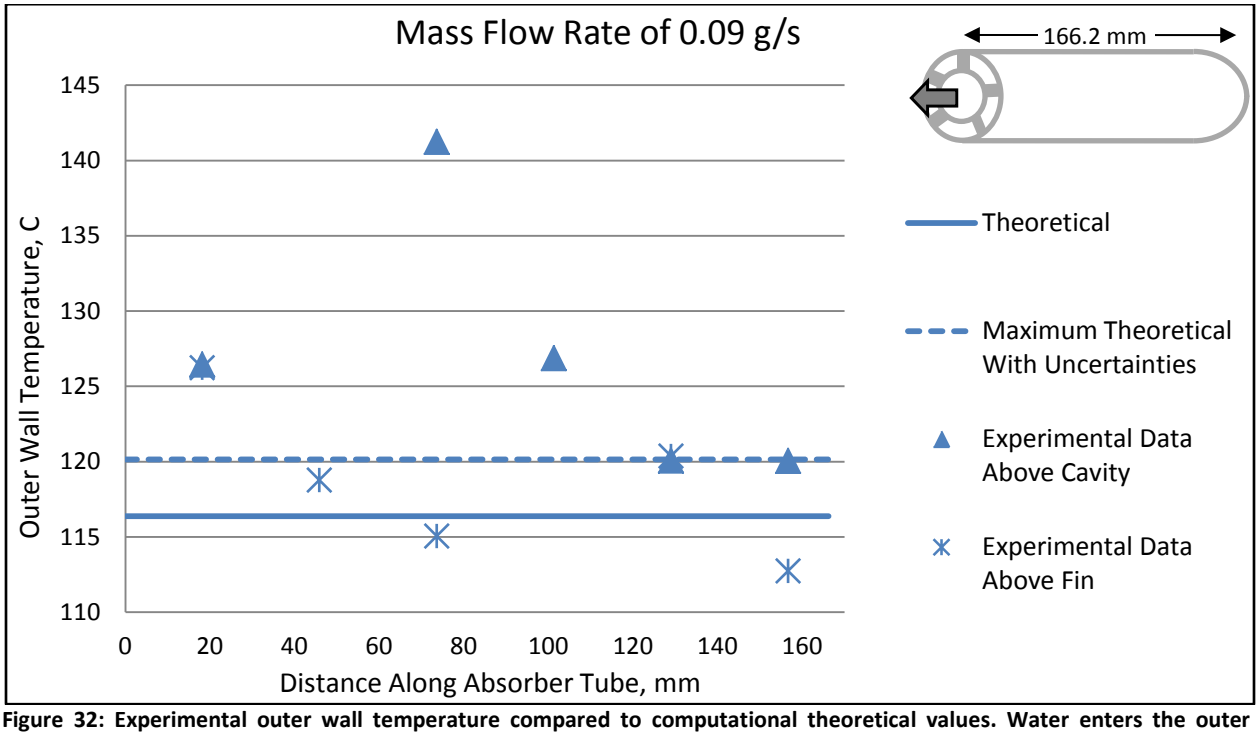

Figure 32: Experimental outer wall temperature compared to computational theoretical values. Water enters the outer chamber at 0.09 g/s at 85.7C and leaves the inner chamber at 100.2C. Strip fin alignment in outer chamber. Uncertainty in mass flow rate and inlet and outlet fluid temperatures creates uncertainty in computational model as shown by the dashed line. Uncertainty in the thermocouples attached to the outer wall is the height of the experimental data markers. The ambient temperature is 29.1C. The inlet pressure is 1 atm.

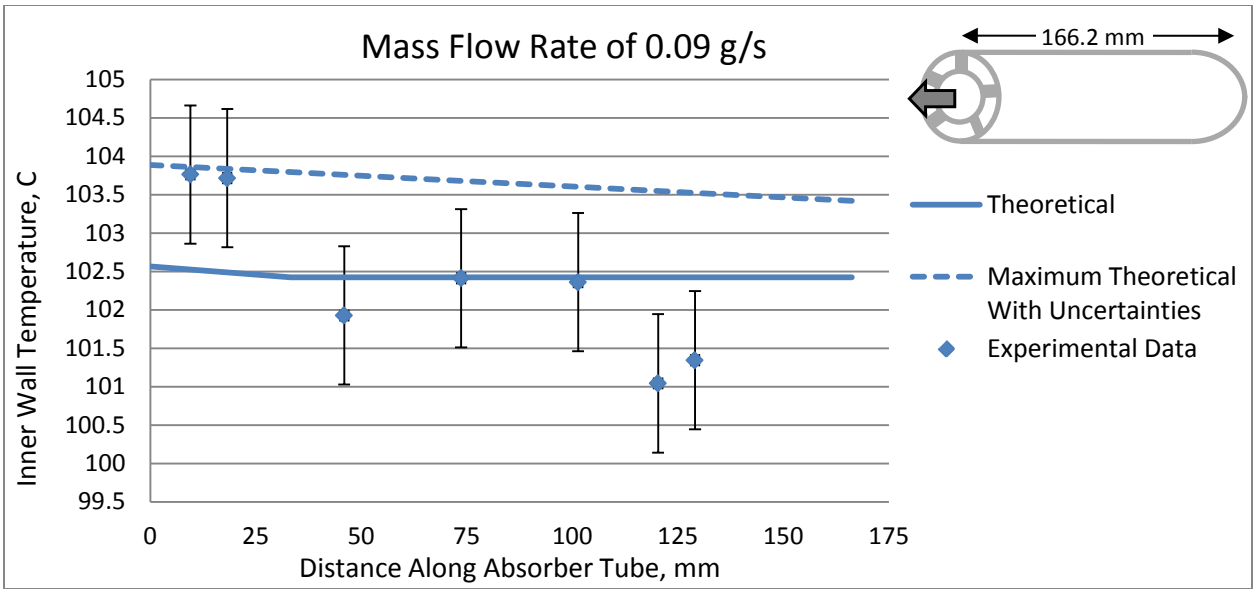

Figure 33: Experimental inner wall temperature compared to computational theoretical value. Water enters the outer chamber at 0.09 g/s at 85.7C and leaves the inner chamber at 100.2C. Strip fin alignment in outer chamber. Uncertainty in mass flow rate and inlet and outlet fluid temperatures creates uncertainty in computational model as shown by the dashed line. Uncertainty in the thermocouples attached to the inner wall is shown by error bars. The ambient temperature is 29.1C. The inlet pressure is 1 atm.

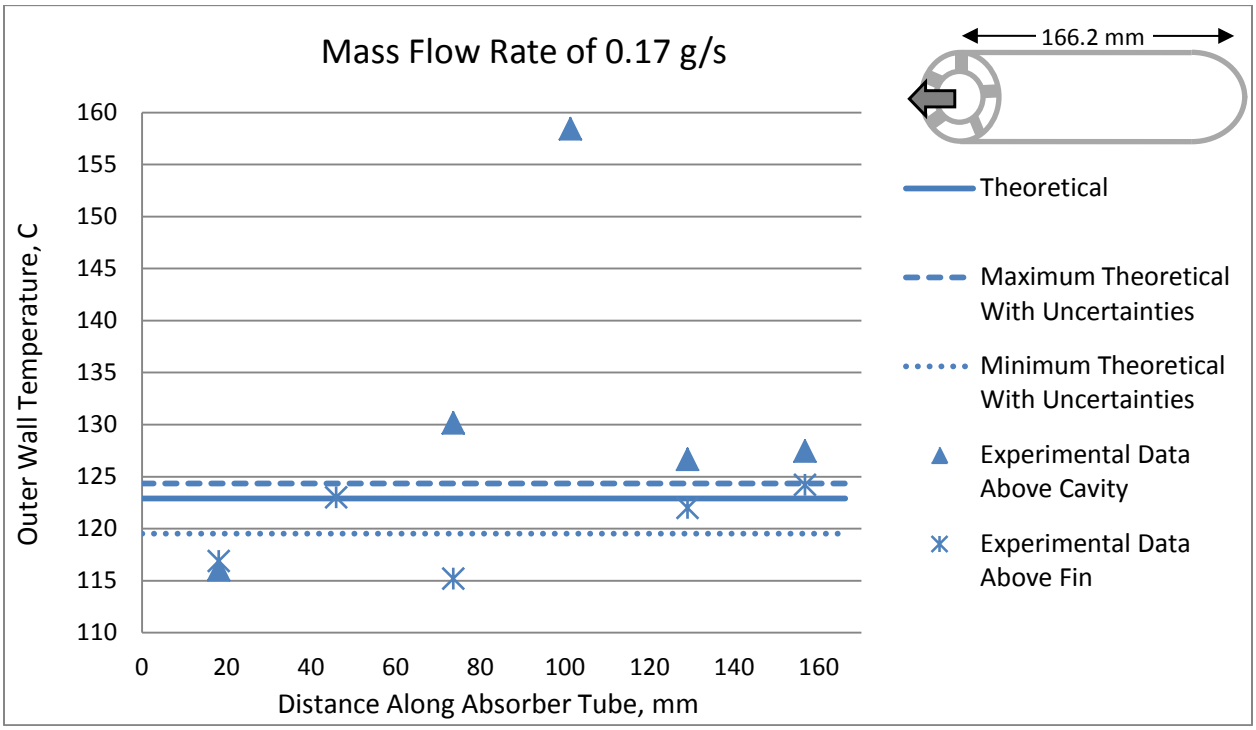

Figure 34: Experimental outer wall temperature compared to computational theoretical values. Water enters the outer chamber at 0.17 g/s at 66.7C and leaves the inner chamber at 100.6C. Strip fin alignment in outer chamber. Uncertainty in mass flow rate and inlet and outlet fluid temperatures creates uncertainty in computational model as shown by the dashed and dotted lines. Uncertainty in the thermocouples attached to the outer wall is the height of the experimental data markers. The ambient temperature is 25.6C. The inlet pressure is 1 atm.

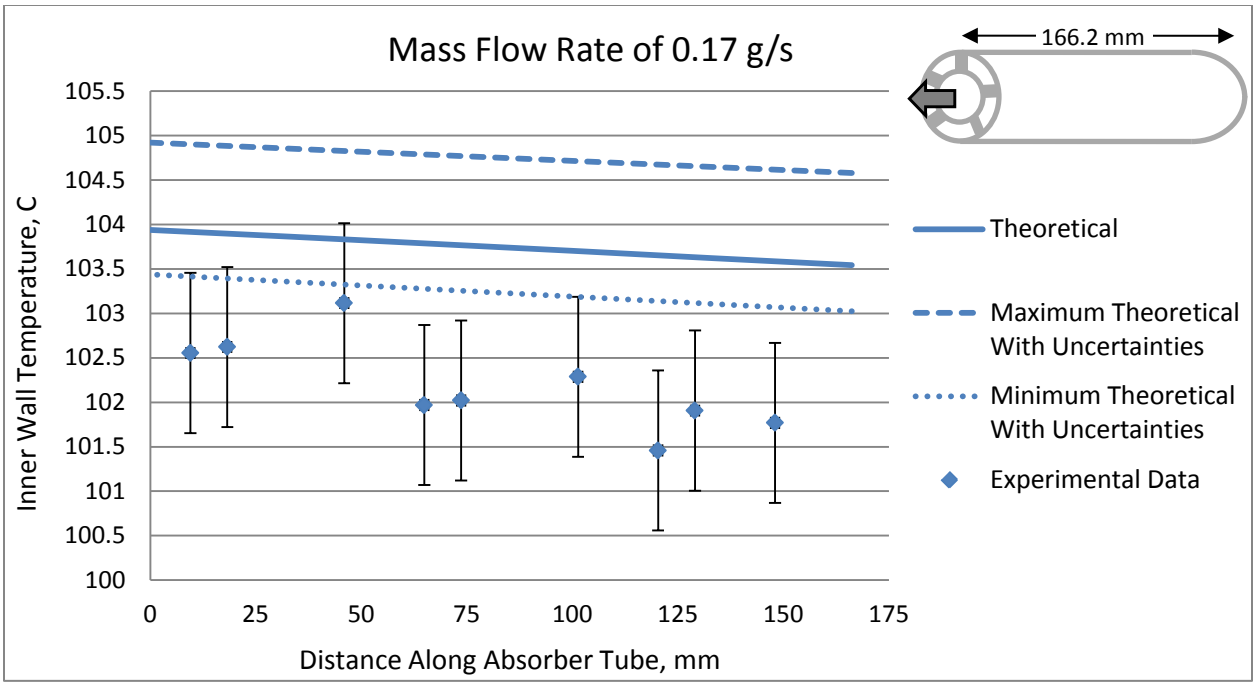

Figure 35: Experimental inner wall temperature compared to computational theoretical value. Water enters the outer chamber at 0.17 g/s at 66.7C and leaves the inner chamber at 100.6C. Strip fin alignment in outer chamber. Uncertainty in mass flow rate and inlet and outlet fluid temperatures creates uncertainty in computational model as shown by the dashed and dotted lines. Uncertainty in the thermocouples attached to the inner wall is shown by error bars. The ambient temperature is 25.6C. The inlet pressure is 1 atm.

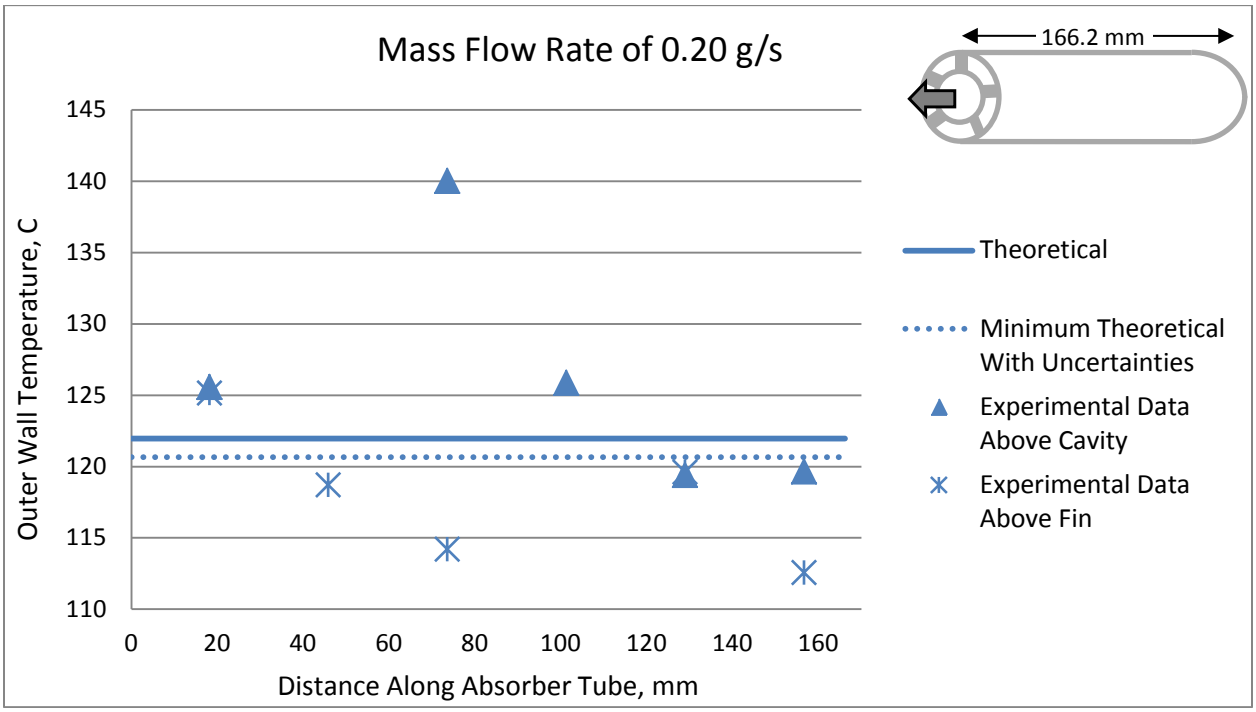

Figure 36: Experimental outer wall temperature compared to computational theoretical values. Water enters the outer chamber at 0.20 g/s at 84.8C and leaves the inner chamber at 100.2C. Strip fin alignment in outer chamber. Uncertainty in mass flow rate and inlet and outlet fluid temperatures creates uncertainty in computational model as shown by the dotted line. Uncertainty in the thermocouples attached to the outer wall is the height of the experimental data markers. The ambient temperature is 28.8C. The inlet pressure is 1 atm.

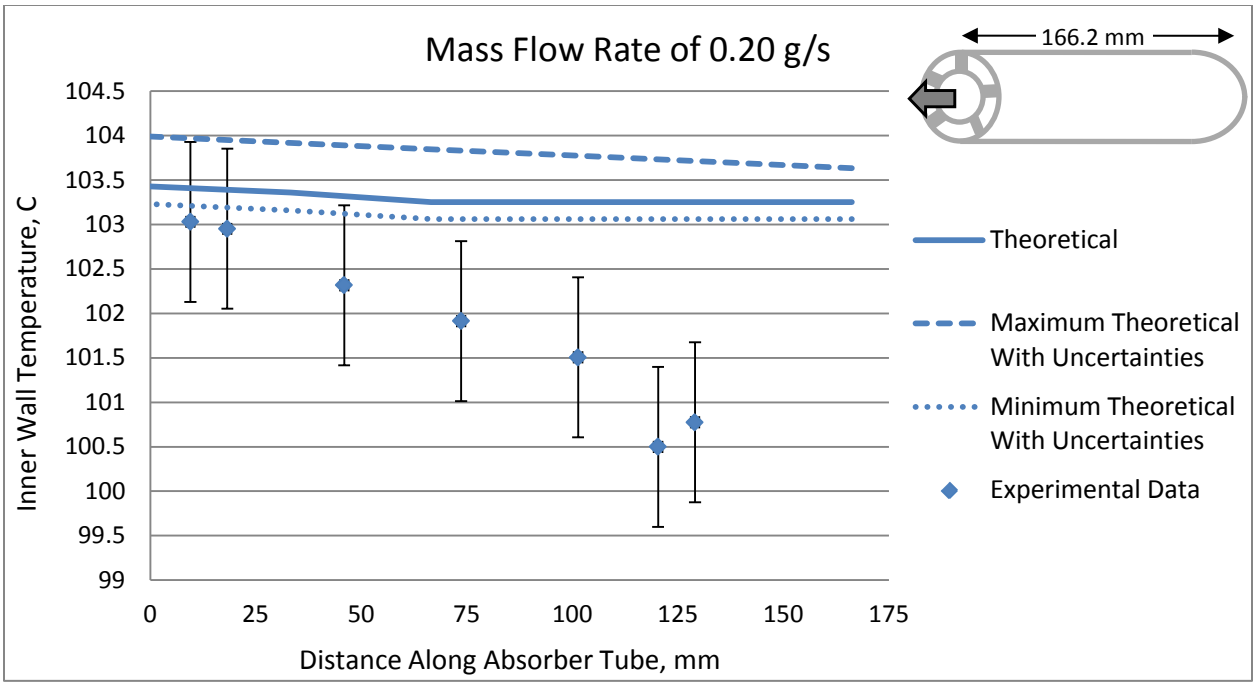

Figure 37: Experimental inner wall temperature compared to computational theoretical value. Water enters the outer chamber at 0.20 g/s at 84.4C and leaves the inner chamber at 100.2C. Strip fin alignment in outer chamber. Uncertainty in mass flow rate and inlet and outlet fluid temperatures creates uncertainty in computational model as shown by the dashed and dotted lines. Uncertainty in the thermocouples attached to the inner wall is shown by error bars. The ambient temperature is 28.8C. The inlet pressure is 1 atm.

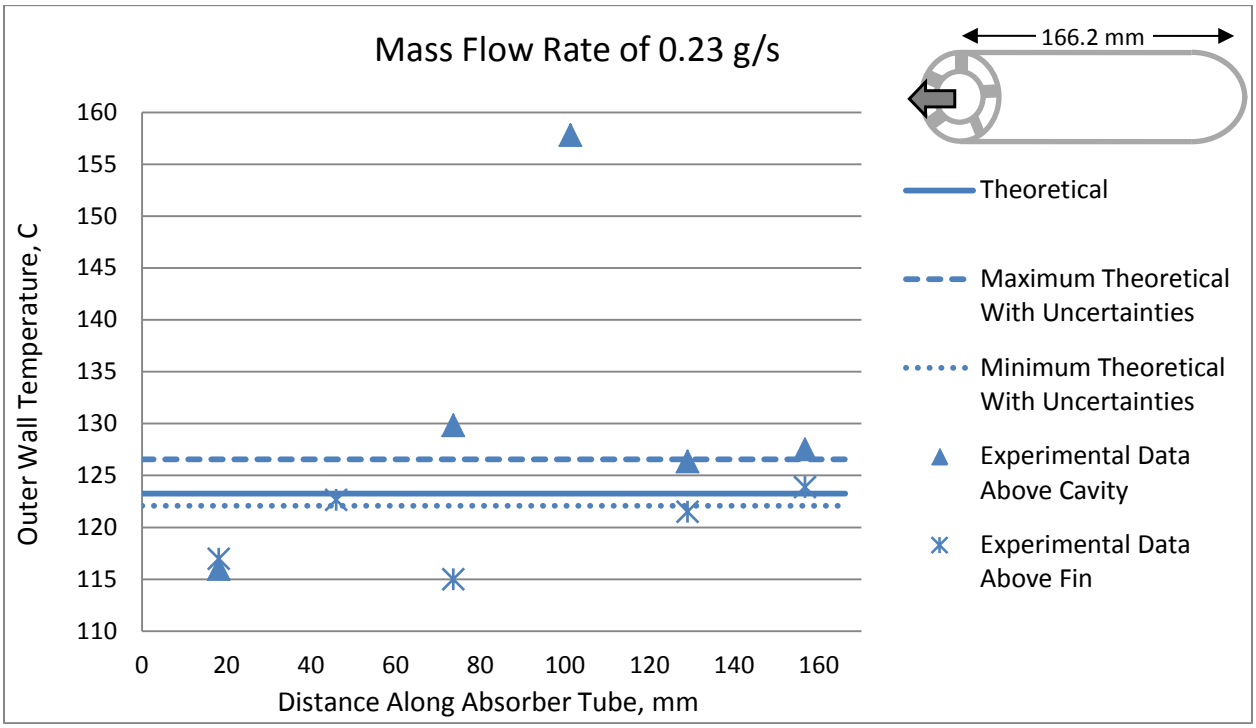

Figure 38: Experimental outer wall temperature compared to computational theoretical values. Water enters the outer chamber at 0.23 g/s at 66.5C and leaves the inner chamber at 100.7C. Strip fin alignment in outer chamber. Uncertainty in mass flow rate and inlet and outlet fluid temperatures creates uncertainty in computational model as shown by the dashed and dotted lines. Uncertainty in the thermocouples attached to the outer wall is the height of the experimental data markers. The ambient temperature is 25.2C. The inlet pressure is 1 atm.

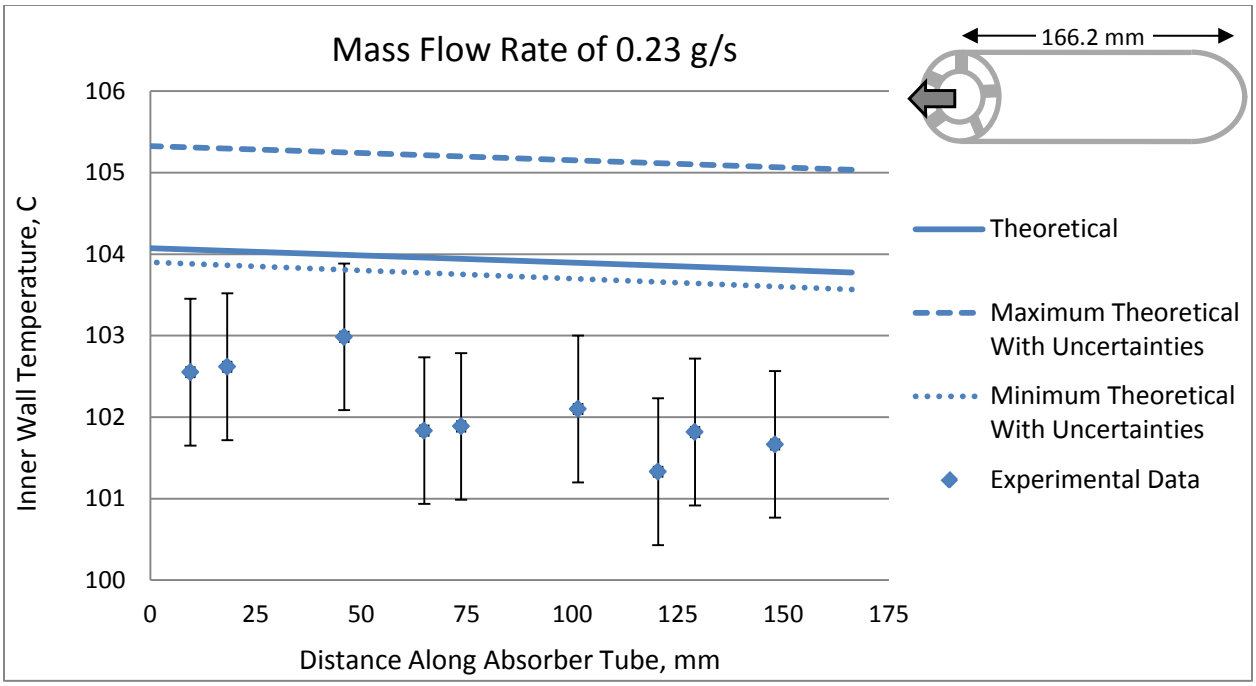

Figure 39: Experimental inner wall temperature compared to computational theoretical value. Water enters the outer chamber at 0.23 g/s at 66.5C and leaves the inner chamber at 100.7C. Strip fin alignment in outer chamber. Uncertainty in mass flow rate and inlet and outlet fluid temperatures creates uncertainty in computational model as shown by the dashed and dotted lines. Uncertainty in the thermocouples attached to the inner wall is shown by error bars. The ambient temperature is 25.2C. The inlet pressure is 1 atm.

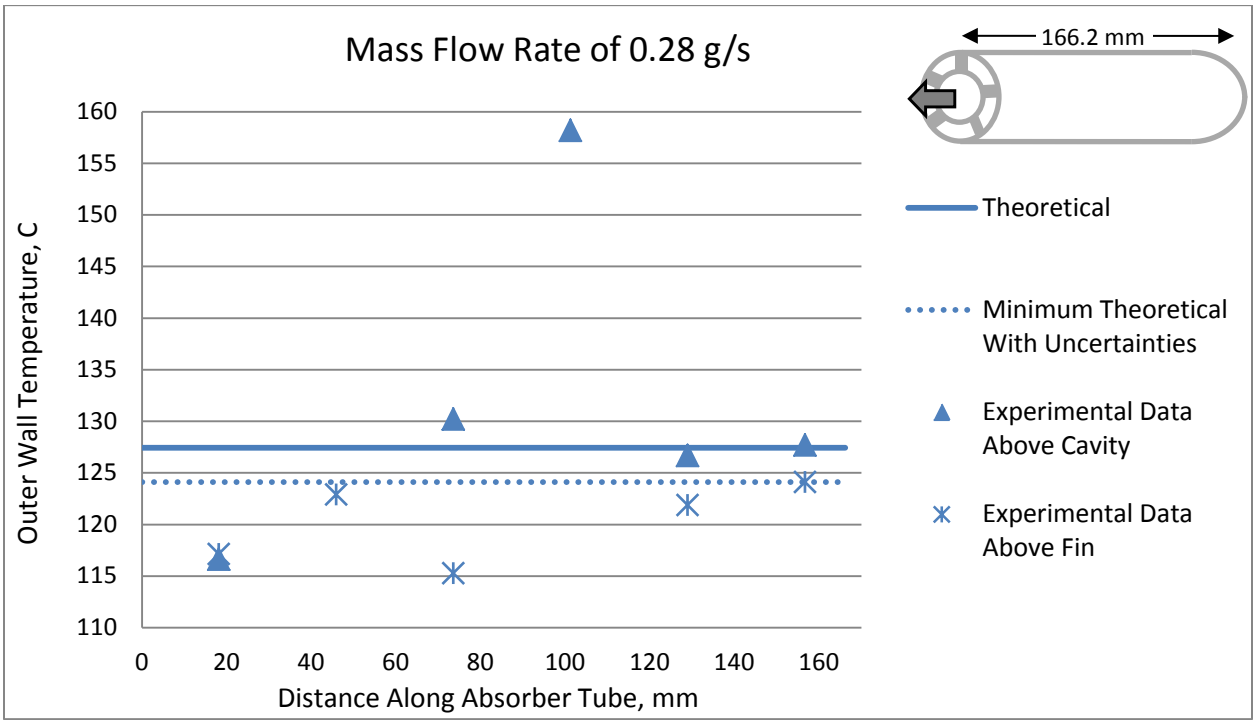

Figure 40: Experimental outer wall temperature compared to computational theoretical values. Water enters the outer chamber at 0.28 g/s at 65.5C and leaves the inner chamber at 100.8C. Strip fin alignment in outer chamber. Uncertainty in mass flow rate and inlet and outlet fluid temperatures creates uncertainty in computational model as shown by the dotted line. Uncertainty in the thermocouples attached to the outer wall is the height of the experimental data markers. The ambient temperature is 25.1C. The inlet pressure is 1 atm.

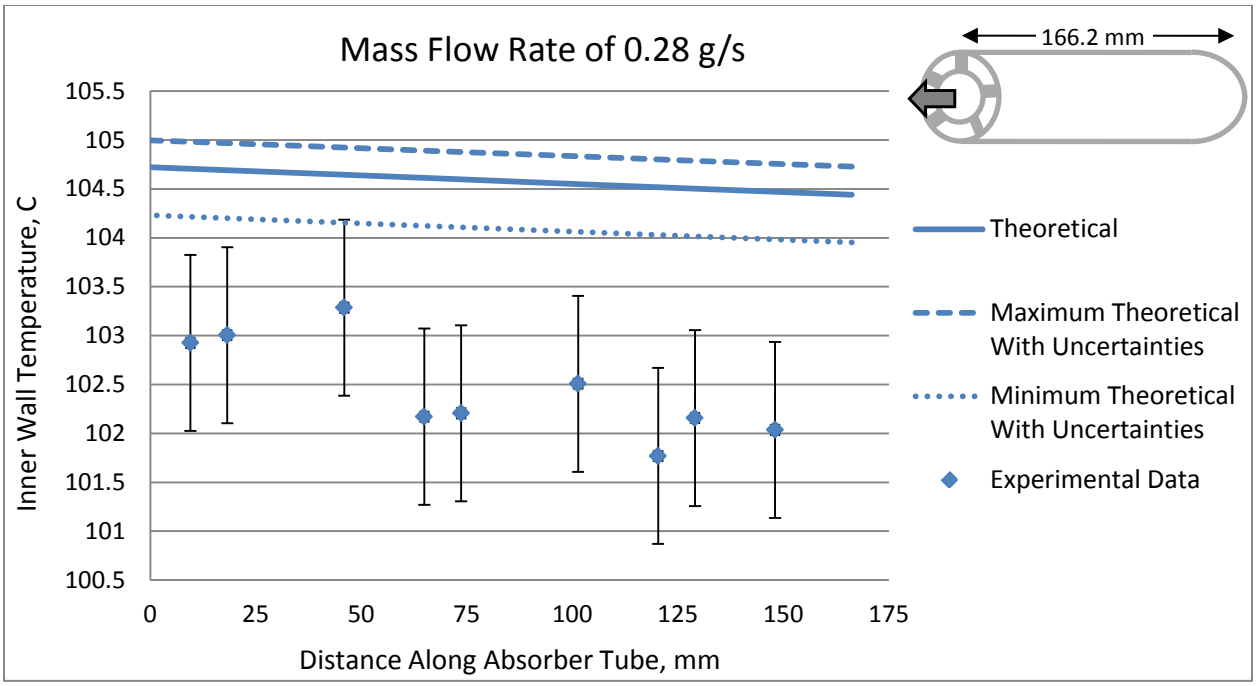

Figure 41: Experimental inner wall temperature compared to computational theoretical value. Water enters the outer chamber at 0.28 g/s at 65.5C and leaves the inner chamber at 100.8C. Strip fin alignment in outer chamber. Uncertainty in mass flow rate and inlet and outlet fluid temperatures creates uncertainty in computational model as shown by the dashed and dotted lines. Uncertainty in the thermocouples attached to the inner wall is shown by error bars. The ambient temperature is 25.1C. The inlet pressure is 1 atm.

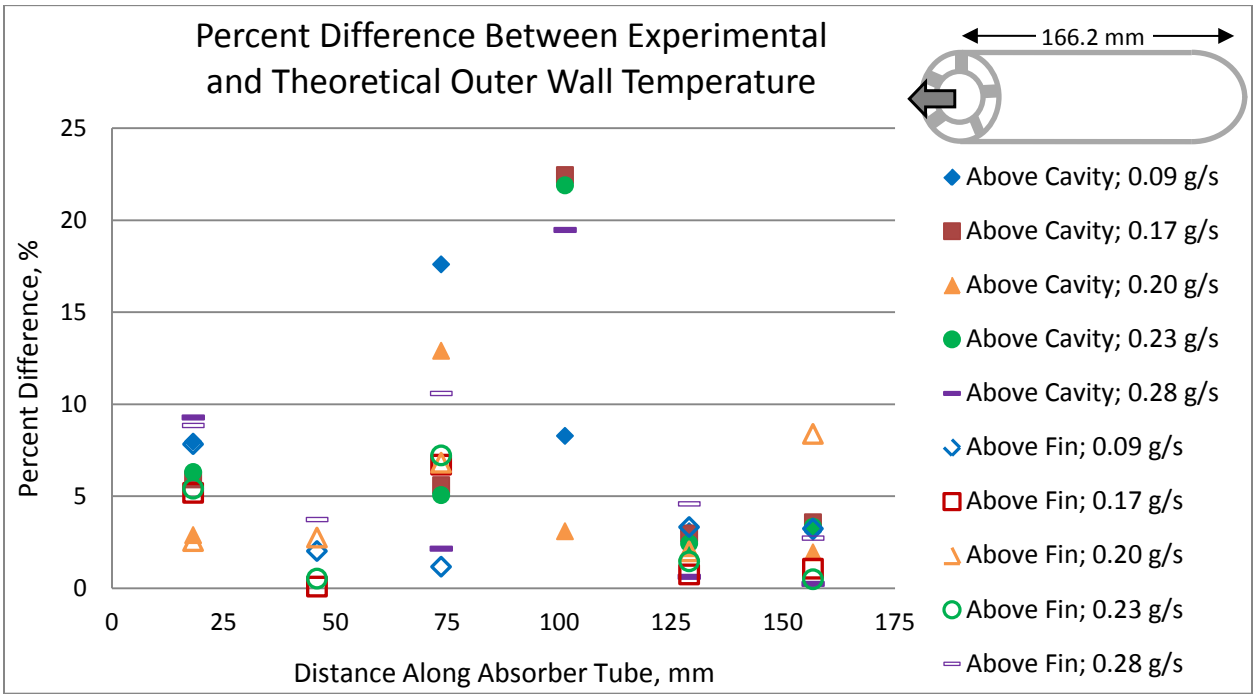

Figure 42: Percent difference between experimental and theoretical outer wall temperature along the absorber tube for all tested mass flow rates. The filled markers represent outer wall temperature data for a region above a cavity. The unfilled markers represent the outer wall temperature data for a region above a fin. Fluid enters the outer chamber first. Strip fin alignment in the outer chamber. Test conditions summarized in Table 5.

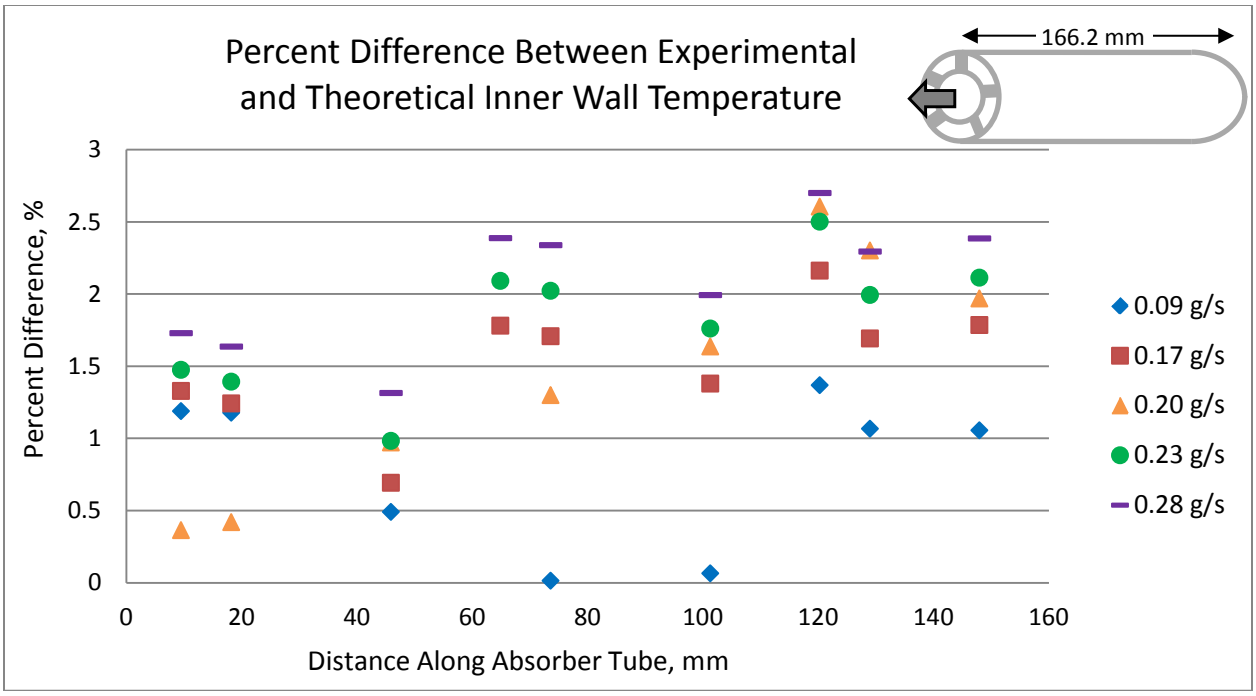

Figure 43: Percent difference between experimental and theoretical inner wall temperature along the absorber tube for all tested mass flow rates. Fluid enters the outer chamber first. Strip fin alignment in the outer chamber. Test conditions summarized in Table 5.

Overall there appears to be very good agreement between the computational model and the experimental data as seen in Figs. 42 – 43. For all mass flow rates studied, there is particularly strong agreement for the inner wall temperature with a percent difference of less than 3%. Conversely, the outer wall temperature shows good agreement between the computational and experimental data. 96% of all experimental data for the temperature of the outer wall agrees within 20% to the computational model. 90% of the experimental data agrees within 11.3%. It is important to realize that there are inherent limitations to the accuracy of the computational model. The computational model used relies heavily on the Stephan and Abdelsalam model for saturated boiling, which was found to agree with water data to a mean deviation of 11.3% (Stephan & Abdelsalam, 1980). Since saturated boiling dominates the outer chamber, the accuracy of the outer wall temperature is as would be expected using this model.

Variation with Fin Alignment

In order to test the benefit of using offset strip fins, the two experimental configurations (aligned fins and off-set strip fins) were compared at two mass flow rates (0.17 g/s and 0.23 g/s).

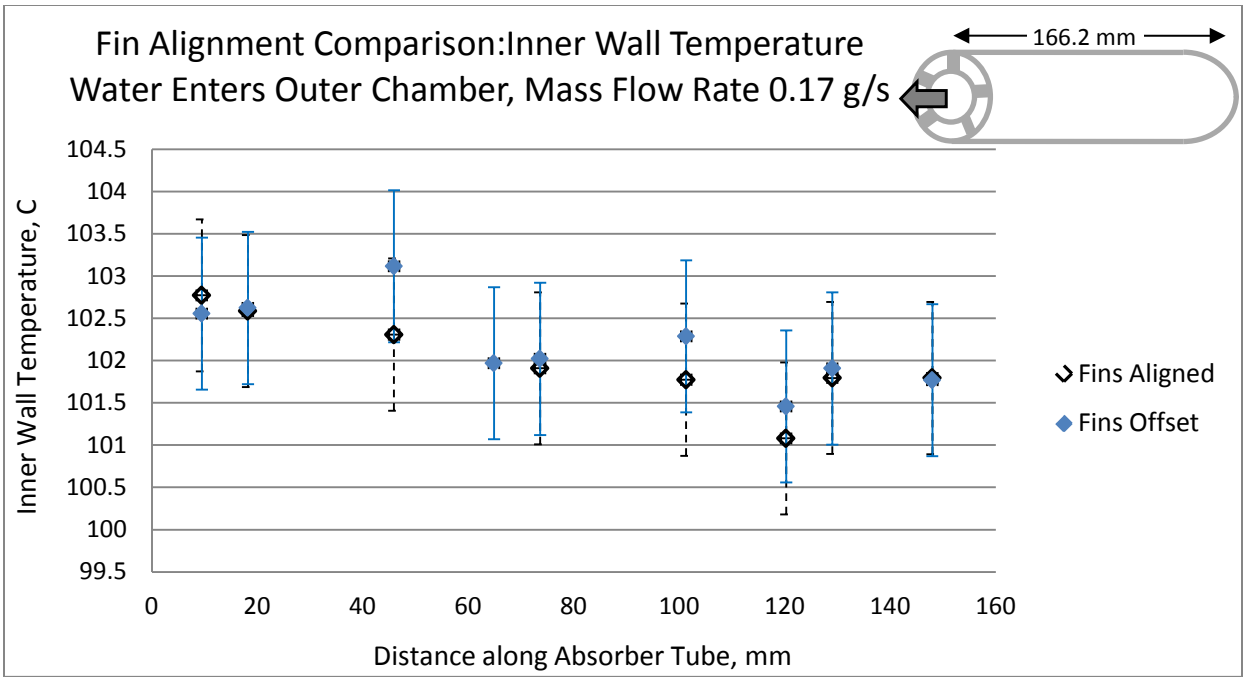

Figure 44: Experimental data of inner wall temperature for two outer chamber fin configurations: aligned and offset. Water enters the outer chamber at 0.17 g/s. For the aligned fin configuration, water enters the absorber tube at 79.9C and exits at 100.4C with an ambient temperature of 24.0C. For the strip fin configuration, water enters the absorber tube at 66.7C and exits at 100.6C with an ambient temperature of 25.6C. Uncertainty in the thermocouples attached to the inner wall is shown by solid blue error bars for offset fins and dashed black error bars for aligned fins. The inlet pressure is 1 atm.

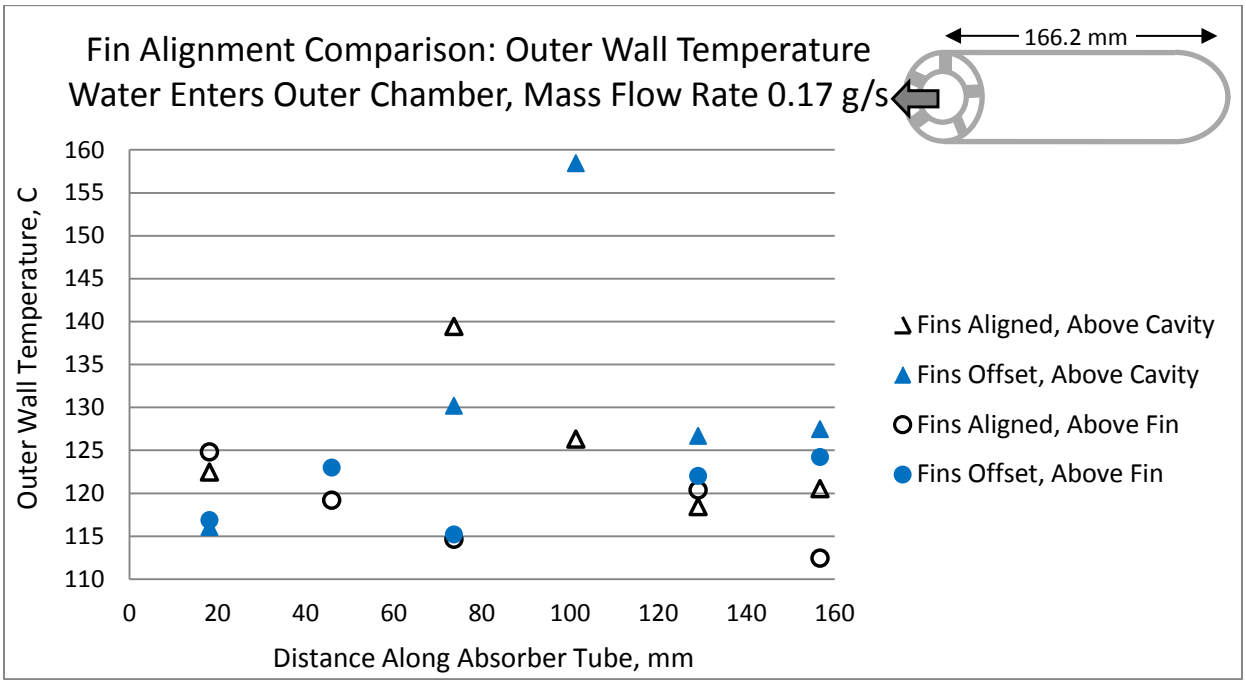

Figure 45: Experimental data of outer wall temperature for two outer chamber fin configurations: aligned and offset. Water enters the outer chamber at 0.17 g/s. For the aligned fin configuration, water enters the absorber tube at 79.9C and exits at 100.4C with an ambient temperature of 24.0C. For the strip fin configuration, water enters the absorber tube at 66.7C and exits at 100.6C with an ambient temperature of 25.6C. Uncertainty in the thermocouples attached to the outer wall is the height of the experimental data markers. The inlet pressure is 1 atm.

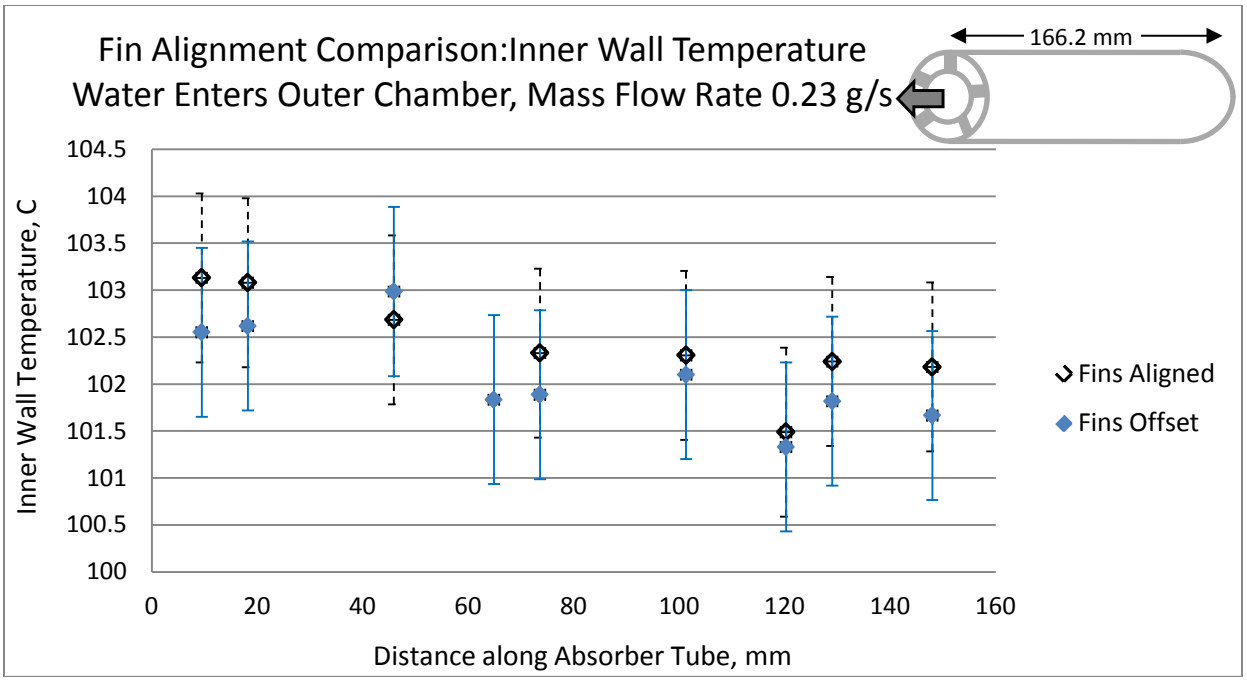

Figure 46: Experimental data of inner wall temperature for two outer chamber fin configurations: aligned and offset. Water enters the outer chamber at 0.23 g/s. For the aligned fin configuration, water enters the absorber tube at 77.9C and exits at 100.4C with an ambient temperature of 23.6C. For the strip fin configuration, water enters the absorber tube at 66.5C and exits at 100.7C with an ambient temperature of 23.6C. Uncertainty in the thermocouples attached to the inner wall is shown by solid blue error bars for offset fins and dashed black error bars for aligned fins. The inlet pressure is 1 atm.

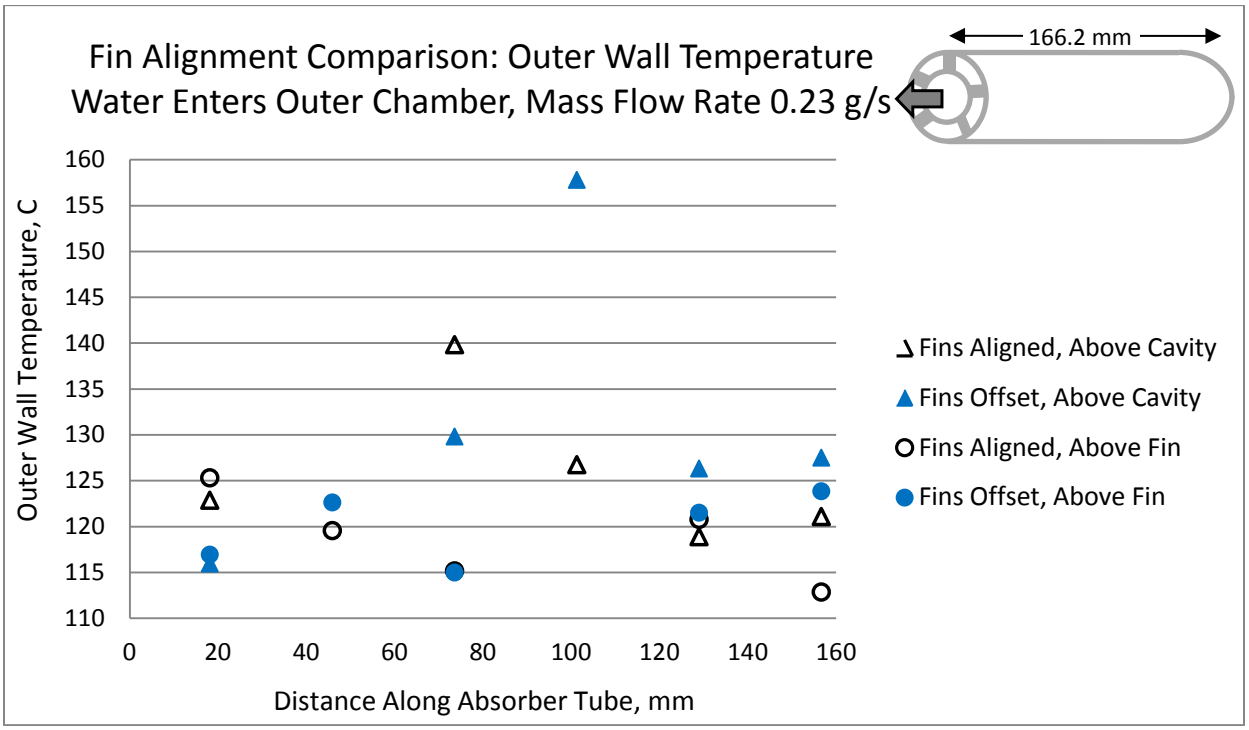

Figure 47: Experimental data of outer wall temperature for two outer chamber fin configurations: aligned and offset. Water enters the outer chamber at 0.23 g/s. For the aligned fin configuration, water enters the absorber tube at 77.9C and exits at 100.4C with an ambient temperature of 23.6C. For the strip fin configuration, water enters the absorber tube at 66.5C and exits at 100.7C with an ambient temperature of 23.6C. Uncertainty in the thermocouples attached to the outer wall is the height of the experimental data markers. The inlet pressure is 1 atm.

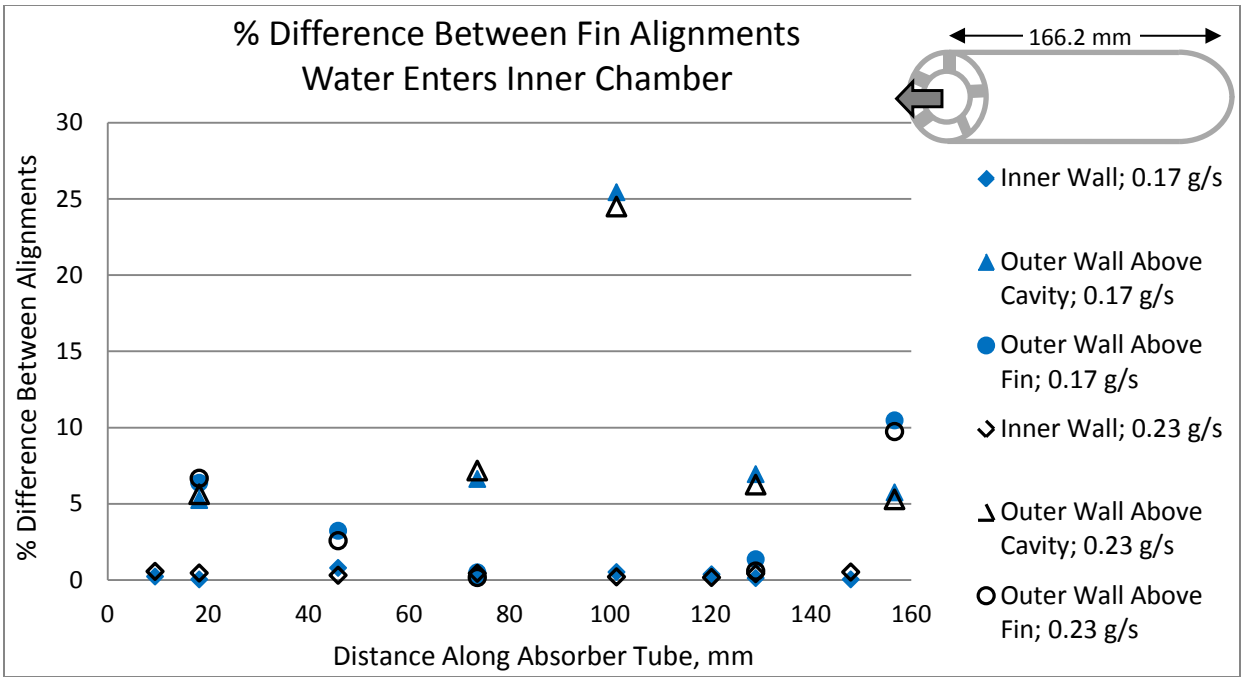

Figure 48: Percent difference between experimental data for two outer chamber fin configurations: aligned and offset. Inner and outer wall temperatures considered. Water enters the outer chamber at 0.17 g/s and 0.23 g/s. Fluid and ambient temperatures are as reported in Table 5.

There appears to be a greater difference in the experimental outer wall temperatures for the two fin configurations when water enters the outer chamber as opposed to the reverse flow. When water enters the outer chamber, 85% of the outer wall data shows less than a 10% difference between the two configurations. However, the difference in the obtained wall temperature data can be as great as 25%. This happens in a thermocouple located above a cavity roughly halfway along the absorber tube. It is possible that a bubble may get trapped when maneuvering through the offset fins. The presence of the localized bubble would result in an increased wall temperature adjacent to it. When the fins are aligned the bubble is less likely to get stuck. It is important to note that one configuration doesn't show a lower outer wall temperature at all data points along the absorber tube. When averaging the outer wall data, it was found that above a fin the average wall temperature differed less than 2^{o}C (120^{o}C vs. 118.5^{o}C). However, above a cavity the aligned fins had an average wall temperature 5^{o}C less than the offset fin configuration (126^{o}C vs. 131^{o}C). This suggests that there may be some advantage to having the fins aligned to reduce bubbles getting entrained and causing localized high temperature areas along the outer wall. On the other hand, Table 6 shows an advantage to having the fins offset. Despite slightly different operating conditions, Table 6 shows that the two fin configurations yield similar heat transfer into the fluid with the offset fin configuration having about a 2% improvement. Regardless of fin configuration, the inner wall temperatures show very strong agreement with a difference of less than 1%. It is unclear which fin configuration will yield the best performance. The offset fin alignment allowed more heat to transfer into the fluid but also resulted in localized high temperature areas on the outer wall. Further studies would be needed.

Table 6: Heat Transfer Performance for Aligned and Offset Fin Configurations

Mass Flow Rate	Fin Alignment	Inlet Fluid Temperature (C)	Exit Fluid Temperature (C)	Ambient Temperature (C)	Heat Transfer Through Tube (W)	Improvement with Offset Fin Alignment
0.17g/s	Aligned	79.9	100.4	24.0	398	--
0.17g/s	Offset	66.7	100.7	25.6	408	2.4%
0.23g/s	Aligned	77.9	100.4	23.6	541	--
0.23g/s	Offset	66.5	100.7	25.2	552	2.1%

Discussion of Absorber Tube Results

Predicted Fluid Behavior

Fluid Enters Inner Chamber

In the following figures, one will find the mean fluid temperature, quality and heat transfer coefficient as a function of the fluid path. The absorber tube length is 166.2 mm. The fluid enters the inner chamber travels the distance of the absorber tube and returns via the outer chamber. The path the fluid travels is twice the length of the absorber tube.

There are several interesting things to note about these figures. The mean temperature and quality of the fluid as a function of fluid path are very similar regardless of mass flow rate. An understanding for this can be found in Fig. 51 showing the local heat transfer coefficient. From Fig. 50 it is clear that the saturated boiling dominates the outer chamber. Therefore, in the outer chamber, the heat transfer coefficient is primarily calculated using Kandlikar's correlation (Kandlikar, 1991). An increase in mass flow rate for a fixed cross sectional area implies an increase to the mass flux, *G*. From Eqns. 24-25, it is clear that an increase in mass flux results in both an increase in liquid-only Reynolds number, Re_{le}, and a decrease in the boiling number, *Bo*. Both of these attribute to an increase in the heat transfer coefficient as seen in Eqns. 22-23. This is further supported by Table 7. For all mass flow rates considered, each has a very similar inlet and exit fluid temperature, resulting in similar enthalpy change through the absorber tube. Since the total heat transfer is equal to the mass flow rate multiplied by the enthalpy change through the system, as the mass flow rate increases and the enthalpy change remains the same, the total heat transfer must increase. The heat is transferred from the outer wall into the bulk fluid primarily by convection, which is a function of surface area, heat transfer coefficient, wall temperature and fluid temperature. The surface area is the same. Since saturated boiling dominates this region, the fluid temperature is 100^{o}C at most locations along the tube. From Table 7, we see that the wall temperature remains fairly consistent (within the uncertainty of the thermocouples) across all mass flow rates. The only way that the total heat transfer could increase is with an increased heat transfer coefficient.

Table 7: Fluid and Outer Wall Temperatures for Various Mass Flow Rates

Mass Flow Rate (g/s)	Inlet Fluid Temperature (C)	Exit Fluid Temperature (C)	Maximum Wall Temperature (C)	Average Wall Temperature (C)
0.09	72.9	100.5	219.6	139.8
0.17	71.0	100.4	223.2	139.7
0.22	72.8	100.5	221.3	140.3
0.25	73.8	100.5	221.7	140.6

Also to note, there appears to be significantly less heat transfer into the inner chamber than the outer chamber. At the turn, the quality is roughly 10%. The energy needed to take a fluid at atmospheric pressure from an inlet temperature of 72°C to a 10% quality, as seen in the inner chamber, is roughly 343 kJ/kg. The energy to further heat that fluid to 100.5°C is roughly 2031 kJ/kg in the outer chamber. Hence, about 15% of the heat that enters the absorber tube is utilized by the inner chamber.

Furthermore, it was difficult to superheat the water. After the water in the outer chamber had become a saturated vapor, it continued to receive additional energy from the surface of the outer wall. If the superheated water was to increase in temperature, there would be a temperature gradient between the fluids in the inner and outer chamber. Heat would then transfer from the superheated vapor in the outer chamber to the subcooled and boiling water in the inner chamber. Some sort of insulation along the outer surface of the inner chamber wall and the sides of the outer chamber fins would be needed to limit this heat transfer. The inner chamber would receive heat from the outer wall surface via the fins. However, it should be noted that strategically placing this insulation would increase manufacturing costs.

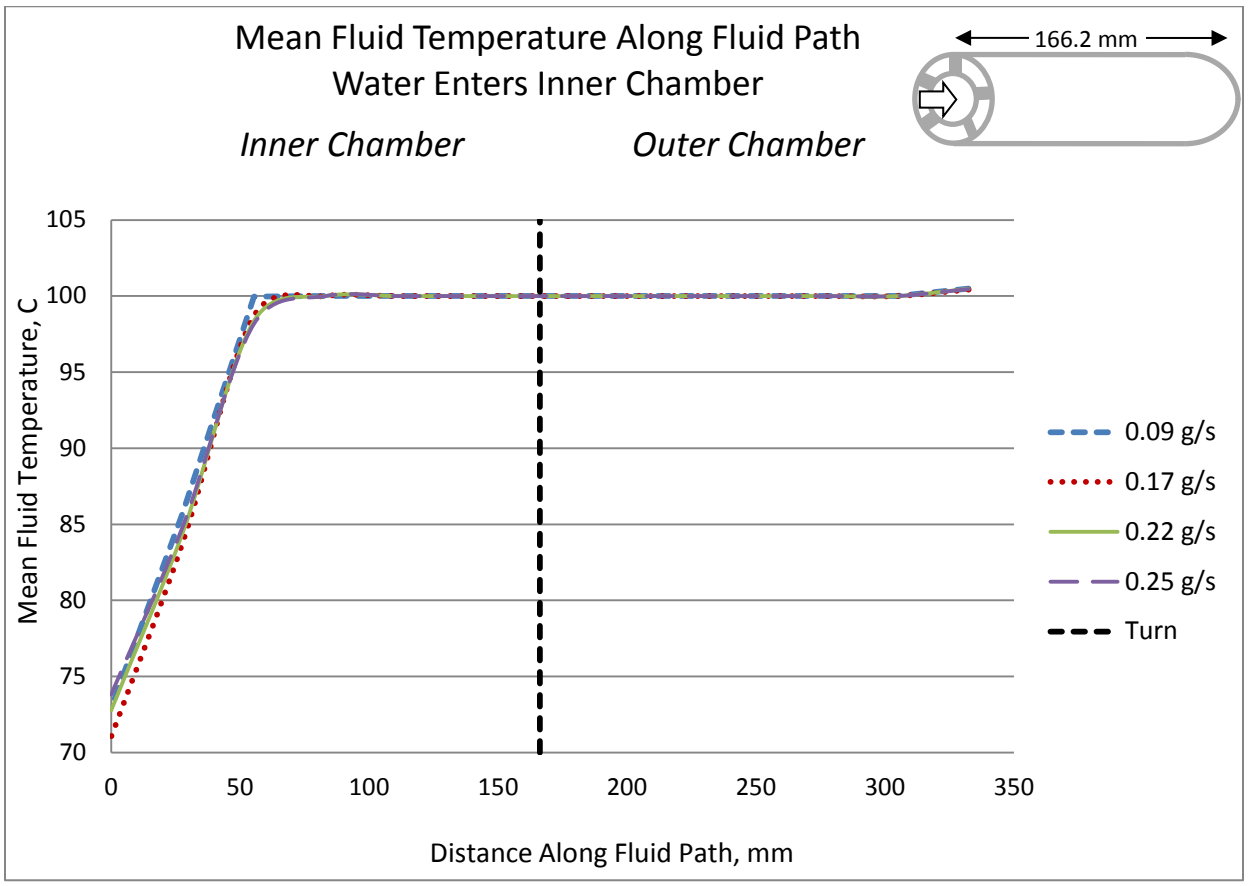

Figure 49: Computational results for the mean fluid temperature along the fluid path. Water enters the inner chamber at various experimentally tested mass flow rates. Test conditions summarized in Table 3.

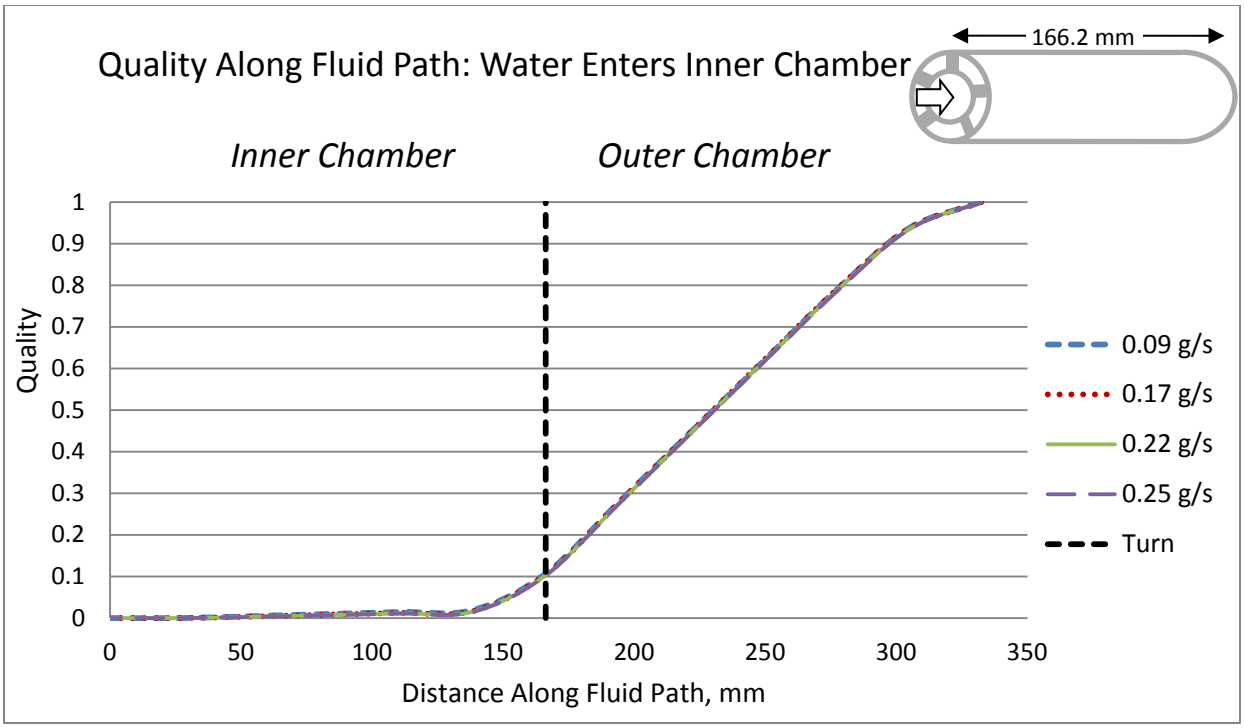

Figure 50: Computational results for quality along the fluid path. Water enters the inner chamber at various experimentally tested mass flow rates. Test conditions summarized in Table 3.

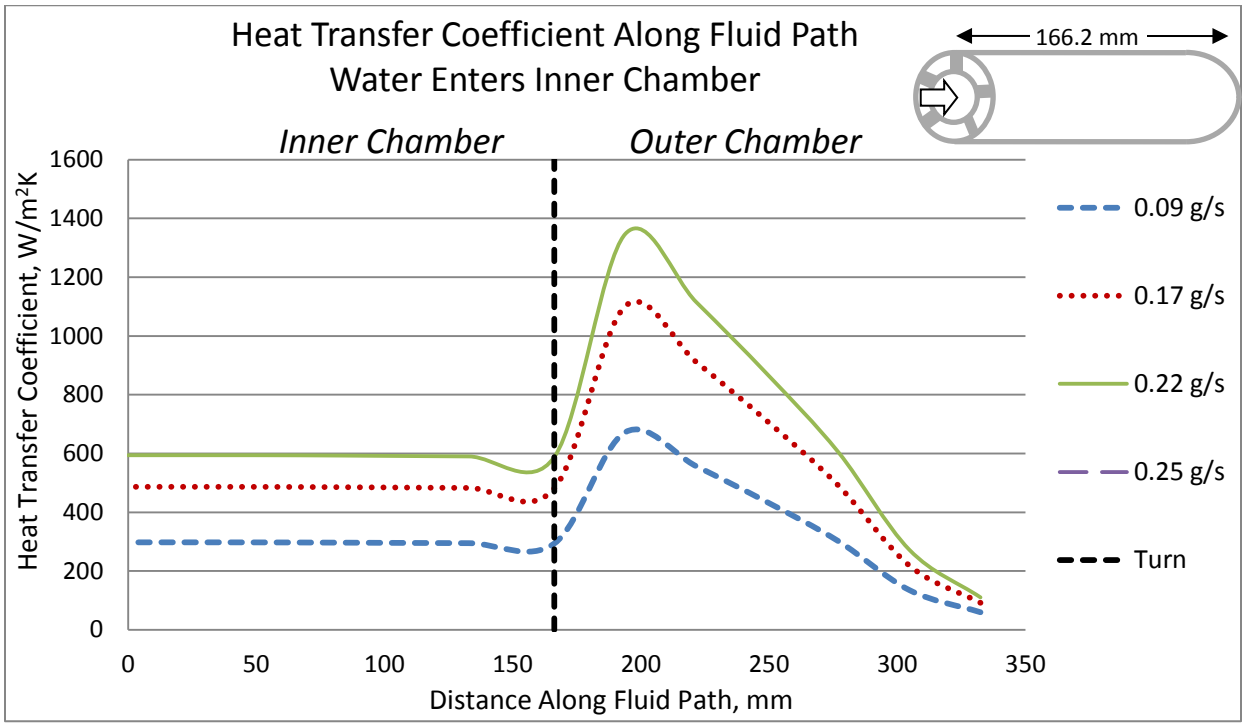

Figure 51: Computational results for heat transfer coefficient into the fluid along the fluid path. Water enters the inner chamber at various experimentally tested mass flow rates. Test conditions summarized in Table 3.

Having calculated the quality along the fluid path, the various heating regimes can more easily be seen. More than half of the inner chamber is dominated by single phase, subcooled heating. Only the last 20% of the outer chamber has single phase, superheating of vapor. To determine

the appropriate two-phase saturated boiling regime, the flow pattern map presented as Fig. 1 in "Flow pattern map for gas-liquid flow in horizontal pipes" was used (Mandhane, Gregory, & Aziz, 1974). Several two-phase regimes are mapped on the log-log plot of the superficial velocities of the fluid and the gas portions of the flow. Since all of the tested mass flow rates are very small (less than 0.3 g/s), both superficial velocities are also quite small resulting in stratified flow. It has been found that two-phase flow regimes and transitions in channels with offset strip fins are similar to those in round tubes (Carey & Mandrusiak, 1986). Hence the same two-phase mapping could be using in both the inner and outer chambers. Fig. 52 shows a more detailed version of Fig. 2 with the various heating regimes indicated.

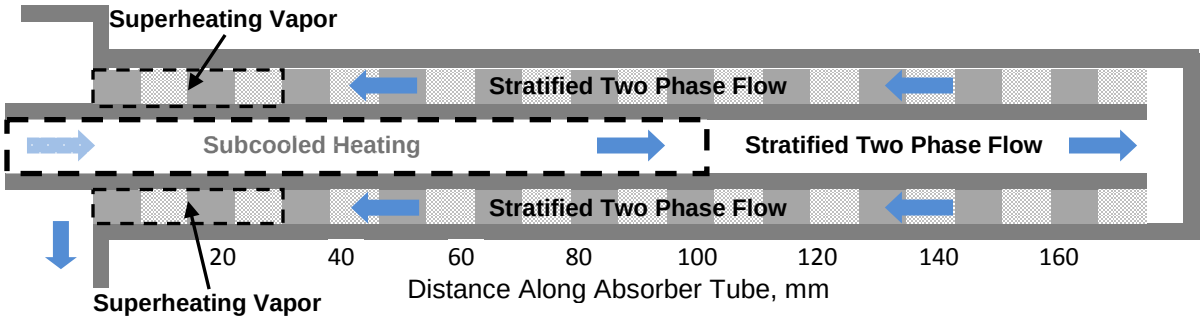

Figure 52: Heating regimes depicted in longitudinal cross section of dual-chamber solar absorber tube for water entering the inner chamber under tested conditions summarized in Table 3.

Fluid Enters Outer Chamber

In the following figures, one will find the mean fluid temperature, quality and heat transfer coefficient as a function of the fluid path for the design configuration of water entering the outer chamber.

There are several interesting things to note. First, the two-phase model used in the outer chamber in the reverse flow was unable to accurately predict wall temperatures. In order to provide improved accuracy, the Stephan-Abdelsalam correlation was used (Stephan & Abdelsalam, 1980). This correlation is only valid for pool boiling, which depends entirely on nucleate boiling. The Kandlikar model (Kandlikar, 1991) that was previously used relies on both the nucleate boiling and convective boiling components. To validate the use of the Stephan-Abdelsalam correlation (Stephan & Abdelsalam, 1980), the nucleate boiling component must be found to dominate making the convective boiling component negligible. To do this, the Chen correlation (Chen, 1966) was utilized. Chen proposed evaluating the heat transfer coefficient as the sum of the microscopic (nucleate boiling) component and the macroscopic (convective boiling) component:

$$h = h_{NBD} + h_{CBD} \tag{96}$$

The nucleate boiling component could be found using the Forster-Zuber correlation (Forster & Zuber, 1955):

$$h_{NBD} = 0.00122\left[\frac{k_l^{0.79} c_{pl}^{0.45} \rho_l^{0.49}}{\sigma^{0.5} \mu_l^{0.29} h_{lv}^{0.24} \rho_v^{0.24}}\right][T_w - T_{sat}(P_l)]^{0.24}[P_{sat}(T_w) - P_l]^{0.75} S \quad (97)$$

Where S is the suppression factor. The suppression factor corrects the nucleate boiling prediction of the heat transfer coefficient to account for convective boiling effects. The suppression factor is a value between zero and one, where zero represents complete convective boiling and one represents complete nucleate boiling. The suppression factor can be calculated using empirical relationships proposed by Collier (Collier, 1981):

$$S = \left[1 + (2.56 \times 10^{-6}) Re_{tp}^{1.17}\right]^{-1} \quad (98)$$

Where the two-phase Reynolds number, Re_{tp}, is defined as:

$$Re_{tp} = Re_l [F(X_{tt})]^{1.25} \quad (99)$$

The liquid only Reynold's number, Re_l, and the Martinelli parameter, X_{tt}, were defined in Eqns. 3 and 9. These depend on the mass flux, quality and saturation properties.

For $X_{tt}^{-1} \leq 0.1$

$$F(X_{tt}) = 1 \quad (100)$$

For $X_{tt}^{-1} > 0.1$

$$F(X_{tt}) = 2.35\left(0.213 + \frac{1}{X_{tt}}\right)^{0.736} \quad (101)$$

For each mass flow rate tested, the suppression factor was calculated along the length of the outer chamber using quality information presented in Fig. 54. It was found that suppression factor varies between 0.94 and 1. The high suppression factor indicates that the heat transfer coefficient is dominated by the nucleate boiling component. It is reasonable to neglect the convective boiling component and model heating in the outer chamber as pool boiling. Hence, the Stephan-Abdelsalam correlation (Stephan & Abdelsalam, 1980) is appropriate to use.

The Stephan-Abdelsalam correlation (Stephan & Abdelsalam, 1980) provides a single heat transfer coefficient for two-phase flow in the outer chamber. Eqn. 64. shows the equation used to obtain the heat transfer coefficient from the Stephan-Abdelsalam correlation. Recall that the computational model iterates on a fixed outer wall temperature. Hence, along the entire absorber tube, the outer wall temperature is assumed constant. Therefore, all the terms on the right-hand side of Eqn. 64 are constant. This results in the heat transfer coefficient being constant regardless of the changes in quality in the outer chamber. This can be seen in Fig. 55 as the horizontal lines that dominate the outer chamber region.

The inner chamber is dominated by a high quality (over 0.9) saturated mixture and superheated vapor. Since this behaves largely as a single phase laminar flow, the heat transfer coefficient is very low. The result of this is that very little heat is transferred to the inner chamber. In the outer chamber, water is taken from an average inlet temperature of 73.8°C to a quality of 0.9. This requires 2140.8 kJ/kg. In the inner chamber, water is taken from a quality of 0.9 to

superheated steam at an average exit temperature of 100.5°C. This requires 226.7 kJ/kg, which is only 9.6% of the total heat transferred into the absorber tube. This is even less than the percentage of heat transferred to the inner chamber for flow in the reverse direction. Additional or thicker fins could help more heat to get transferred to the inner chamber. Alternatively, tripping the flow into turbulence perhaps by increased surface roughness could increase the heat transfer coefficient in the inner chamber. However, this would have the adverse effect of also increasing the pressure losses. It is important to realize that the outer wall temperature was only about 125°C. A temperature gradient is needed between the fluid in the inner chamber and the outer wall; thus, limiting how much superheat can occur in the inner chamber.

Table 8: Fluid and Outer Wall Temperatures for Various Mass Flow Rates

Mass Flow Rate (g/s)	Inlet Fluid Temperature (C)	Exit Fluid Temperature (C)	Predicted Theoretical Wall Temperature (C)	Average Experimental Wall Temperature (C)	Difference in Wall Temperature
0.09	85.7	100.2	116.4	122.8	5.2%
0.17	66.7	100.6	122.9	126.0	2.5%
0.20	84.8	100.2	122.0	122.1	0.1%
0.23	66.5	100.7	123.3	125.7	1.9%
0.28	65.5	100.8	127.4	126.1	1.0%

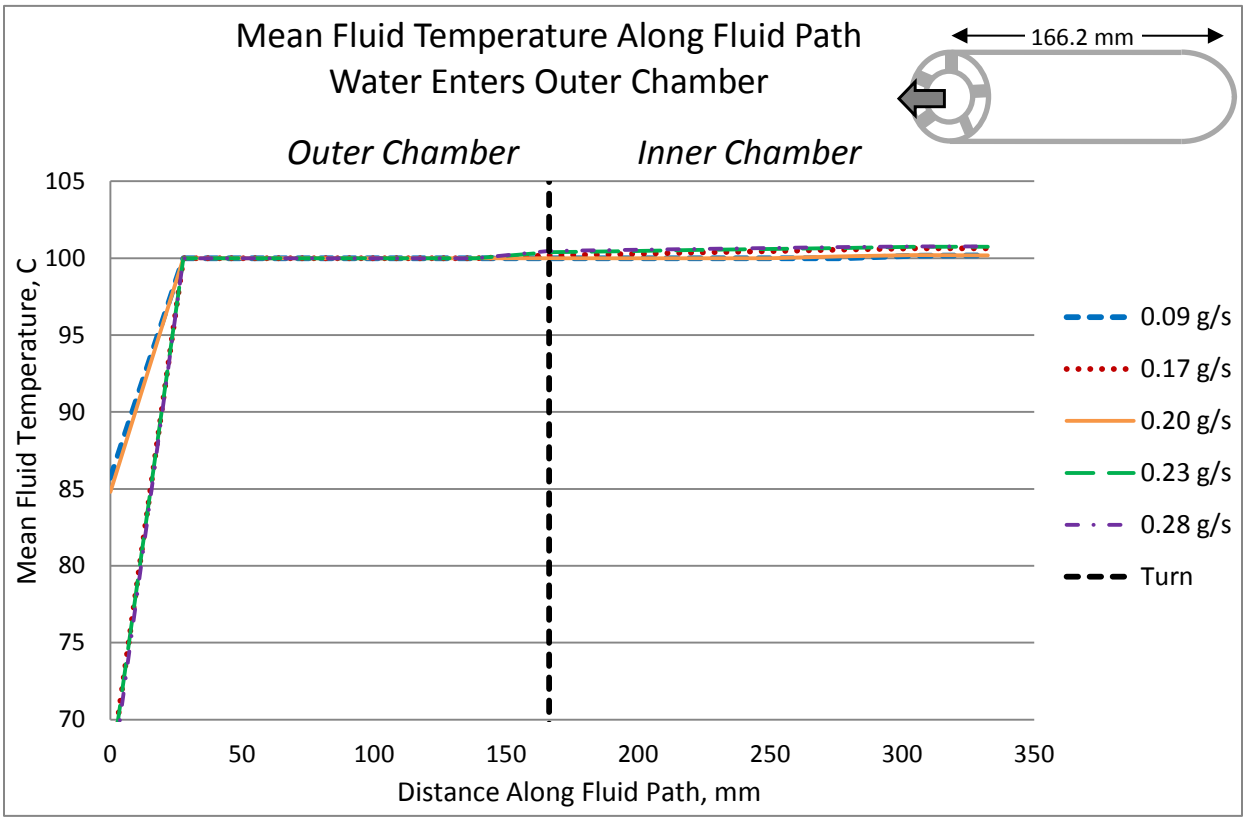

Figure 53: Computational results for the mean fluid temperature along the fluid path. Water enters the outer chamber at various experimentally tested mass flow rates. Test conditions summarized in Table 5.

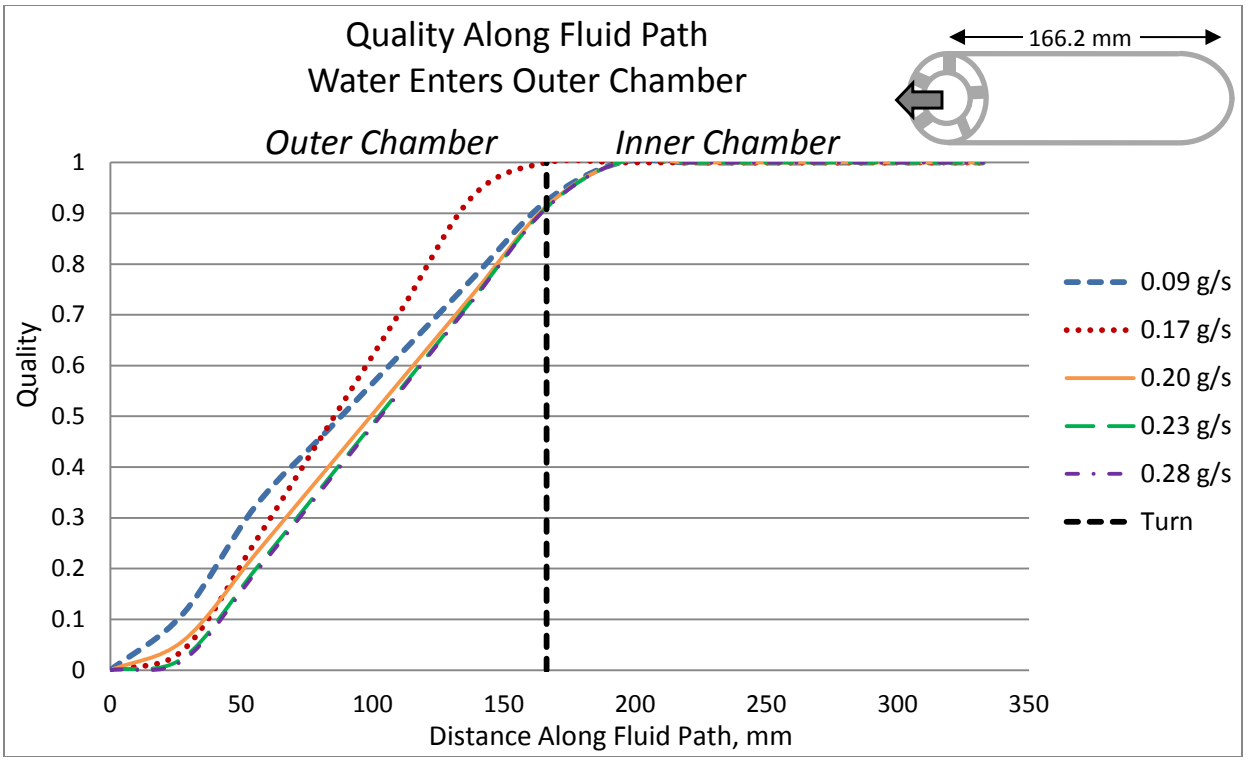

Figure 54: Computational results for quality along the fluid path. Water enters the outer chamber at various experimentally tested mass flow rates. Test conditions summarized in Table 5.

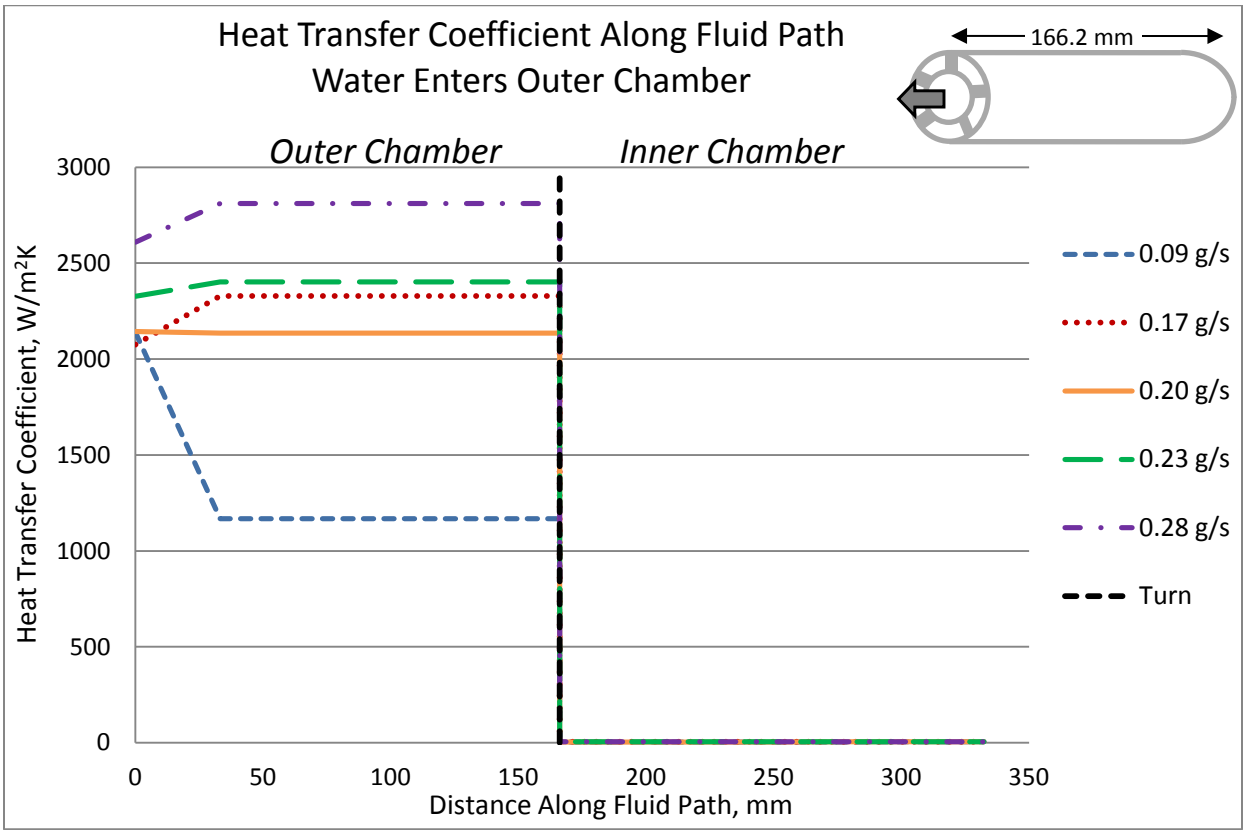

Figure 55: Computational results for heat transfer coefficient into the fluid along the fluid path. Water enters the outer chamber at various experimentally tested mass flow rates. Test conditions summarized in Table 5.

Having calculated the quality along the fluid path, the various heating regimes can once again be mapped. Roughly the first 20% of the inner chamber is single phase, subcooled heating. The majority of the outer chamber is single phase, superheating of vapor. To determine the appropriate two-phase saturated boiling regime, the same flow pattern map was used as in the analysis of flow in the reverse direction (Mandhane, Gregory, & Aziz, 1974). Since all of the tested mass flow rates are very small (less than 0.3 g/s), all of the two-phase saturated boiled occurs as stratified flow. Fig. 56 shows a more detailed version of Fig. 2 with the various heating regimes indicated.

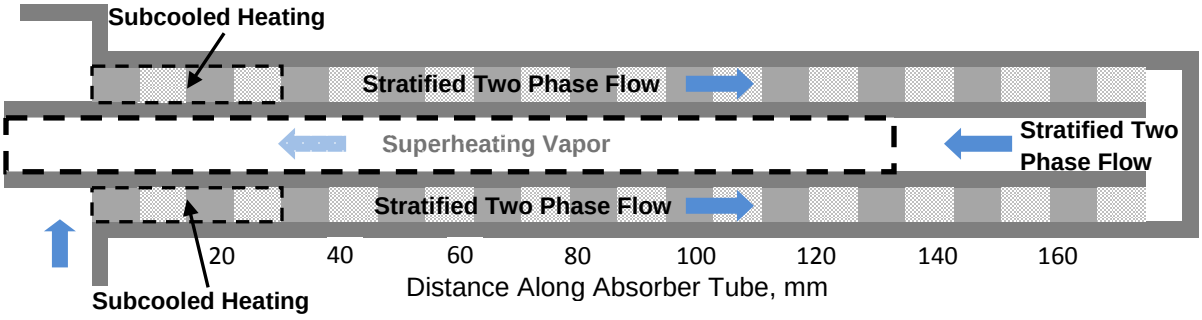

Figure 56: Heating regimes depicted in longitudinal cross section of dual-chamber solar absorber tube for water entering the outer chamber under tested conditions summarized in Table 5.

Comparison to Single Chamber Performance

Decrease Thermal Losses

To compare the performance of the dual chamber design to the conventional single chamber design several considerations were made. First, the single and dual chamber designs have the same inlet and exit fluid temperatures and mass flow rates to ensure the same heat input to the system. Next, the inner radius of the dual chamber is the radius of the single chamber design. This ensures that the length of the fluid path is the same. Hence, the absorber tube length of the dual chamber design is half the length of the single chamber design. From Figs. 57-65 it is clear that the outer wall temperature for the single chamber is extremely high near superheated water vapor. Superheated vapor has poor thermal conductivity and the heat transfer coefficient for single phase flow is very low relative to two-phase flow. It is very difficult for energy from the wall to transfer into the gas. Unlike the dual chamber design, there are no fins to act as a heat sink to send the heat into the inner chamber. A high wall temperature results in greater losses to the surroundings. It should be noted that the outer wall temperature in the single chamber design may be over-estimated in the computational model as the model does not account for axial conduction.

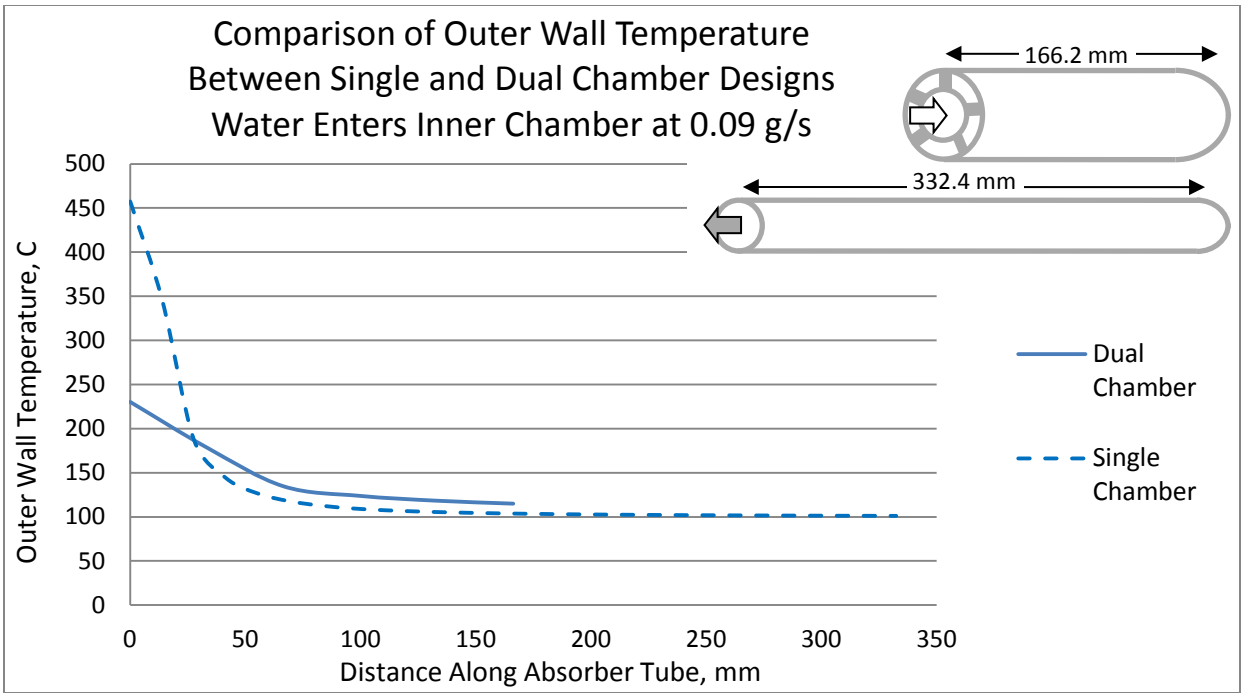

Figure 57: Comparison of single chamber and dual chamber computational outer wall temperatures for a mass flow rate of 0.09 g/s. Fluid enters the inner chamber and exits the outer chamber the dual chamber design. The single and dual chamber designs have the same inlet fluid temperature, exit fluid temperature, and mass flow rate as presented in Table 3 to ensure the same heat input to both systems. The inner radius of the dual chamber is the radius of the single chamber design. The length of both fluid paths is the same so the absorber tube length of the dual chamber design is half the length of the single chamber design.

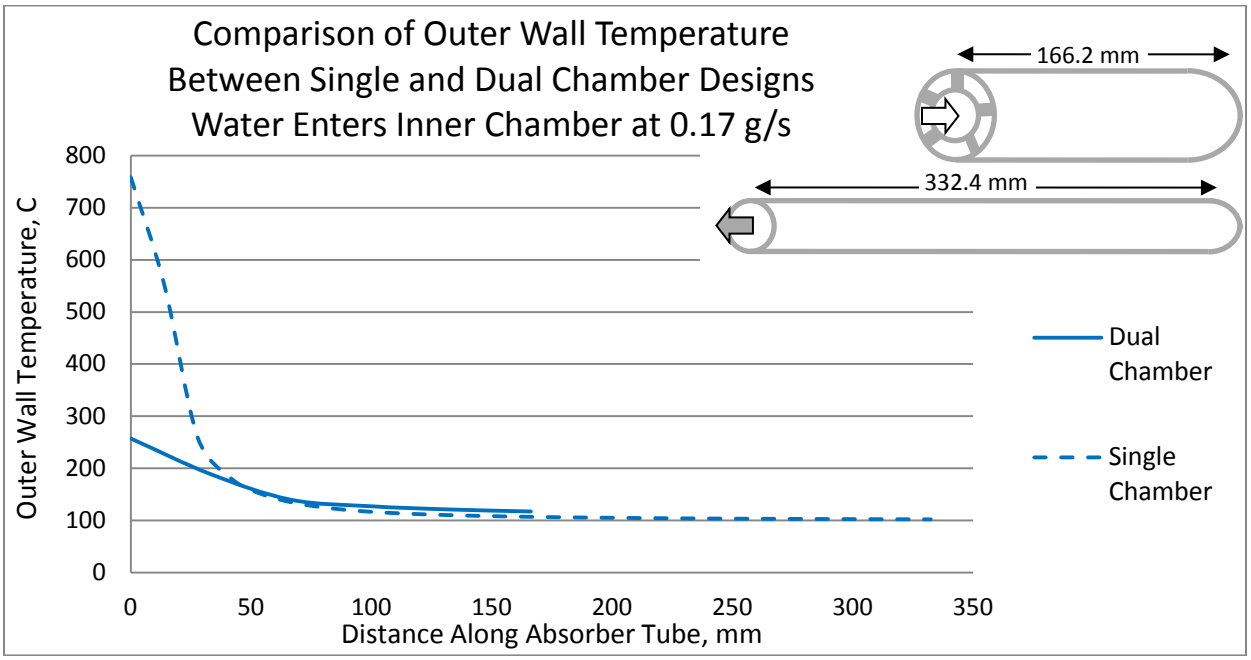

Figure 58: Comparison of single chamber and dual chamber computational outer wall temperatures for a mass flow rate of 0.17 g/s. Fluid enters the inner chamber and exits the outer chamber the dual chamber design. The single and dual chamber designs have the same inlet fluid temperature, exit fluid temperature, and mass flow rate as presented in Table 3 to ensure the same heat input to both systems. The inner radius of the dual chamber is the radius of the single chamber design. The length of both fluid paths is the same so the absorber tube length of the dual chamber design is half the length of the single chamber design.

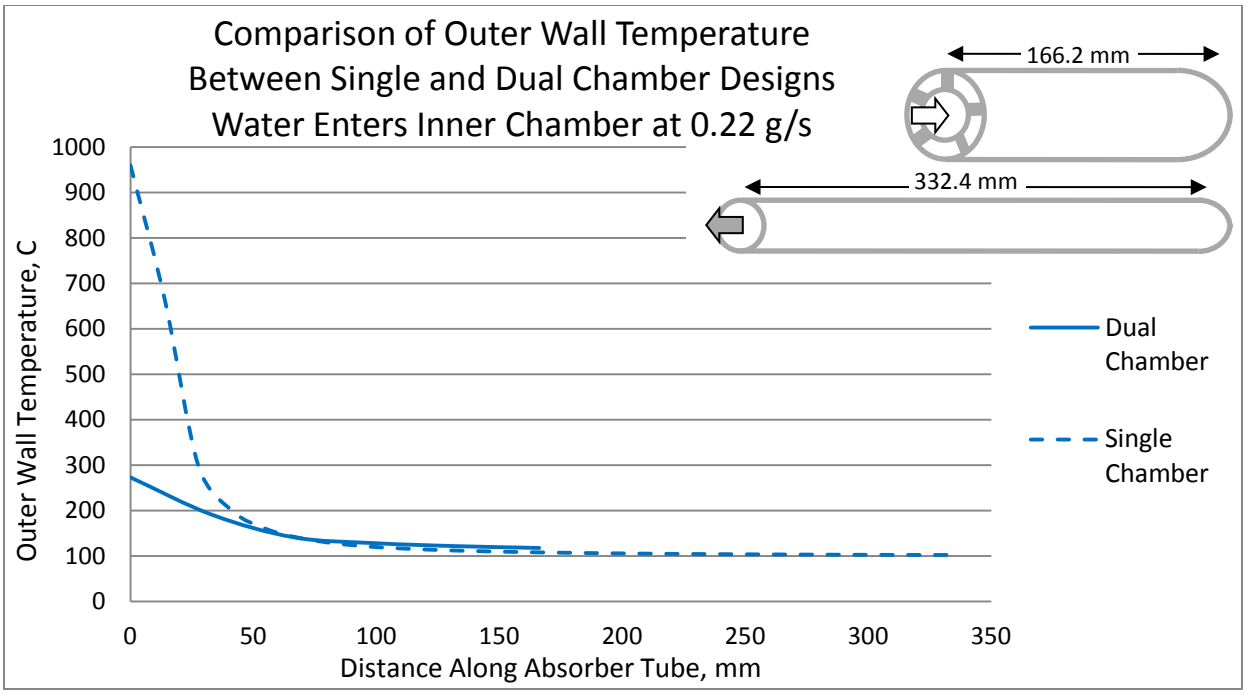

Figure 59:Comparison of single chamber and dual chamber computational outer wall temperatures for a mass flow rate of 0.22 g/s. Fluid enters the inner chamber and exits the outer chamber the dual chamber design. The single and dual chamber designs have the same inlet fluid temperature, exit fluid temperature, and mass flow rate as presented in Table 3 to ensure the same heat input to both systems. The inner radius of the dual chamber is the radius of the single chamber design. The length of both fluid paths is the same so the absorber tube length of the dual chamber design is half the length of the single chamber design.

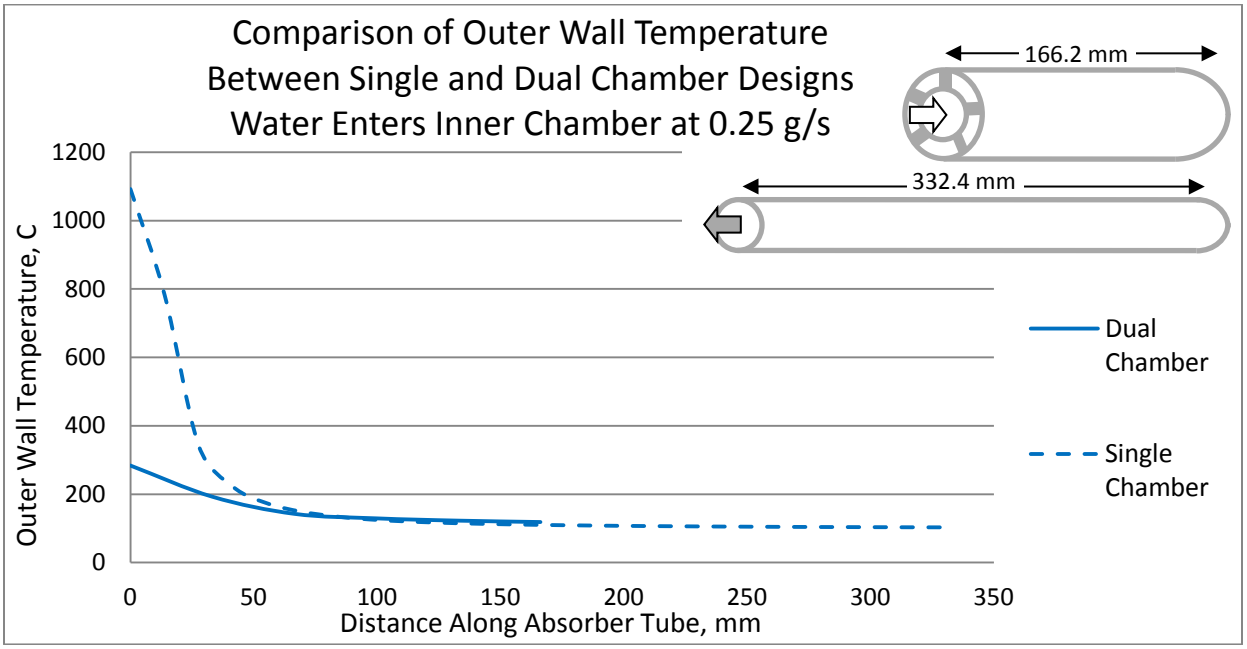

Figure 60: Comparison of single chamber and dual chamber computational outer wall temperatures for a mass flow rate of 0.25 g/s. Fluid enters the inner chamber and exits the outer chamber the dual chamber design. The single and dual chamber designs have the same inlet fluid temperature, exit fluid temperature, and mass flow rate as presented in Table 3 to ensure the same heat input to both systems. The inner radius of the dual chamber is the radius of the single chamber design. The length of both fluid paths is the same so the absorber tube length of the dual chamber design is half the length of the single chamber design.

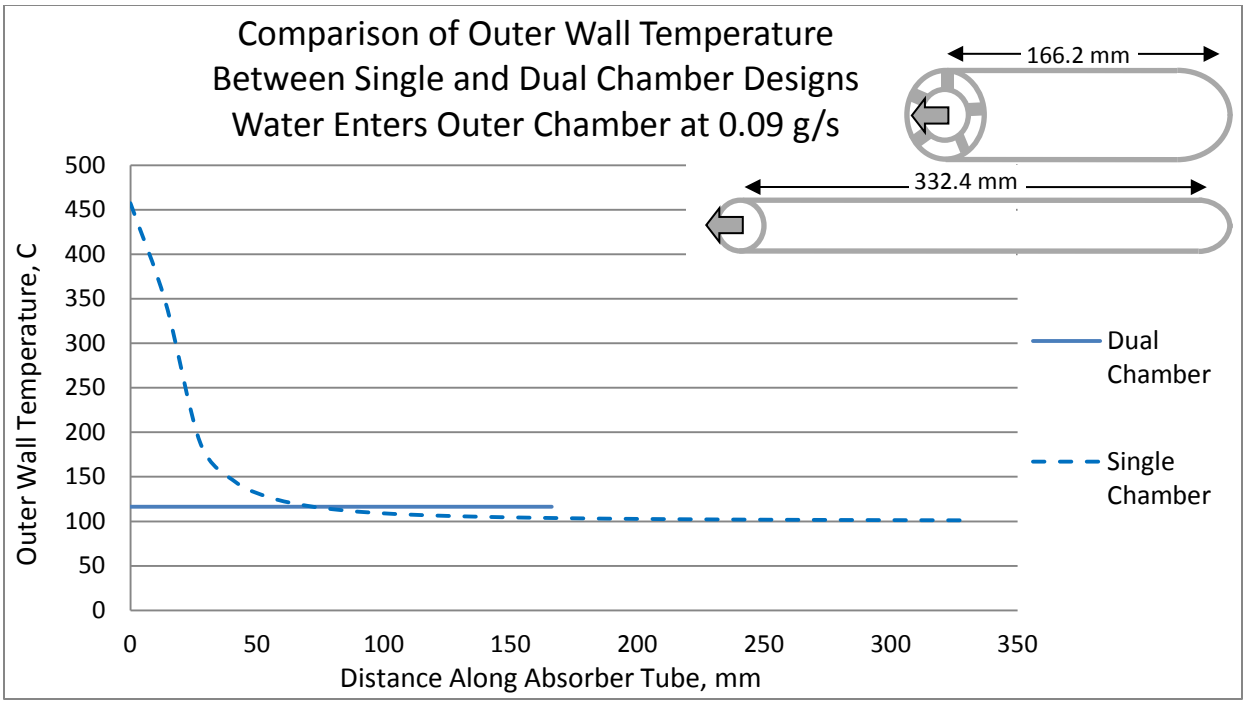

Figure 61: Comparison of single chamber and dual chamber computational outer wall temperatures for a mass flow rate of 0.09 g/s. Fluid enters the outer chamber and exits the inner chamber in the dual chamber design. The single and dual chamber designs have the same inlet fluid temperature, exit fluid temperature, and mass flow rate as presented in Table 5 to ensure the same heat input to both systems. The inner radius of the dual chamber is the radius of the single chamber design. The length of both fluid paths is the same so the absorber tube length of the dual chamber design is half the length of the single chamber design.

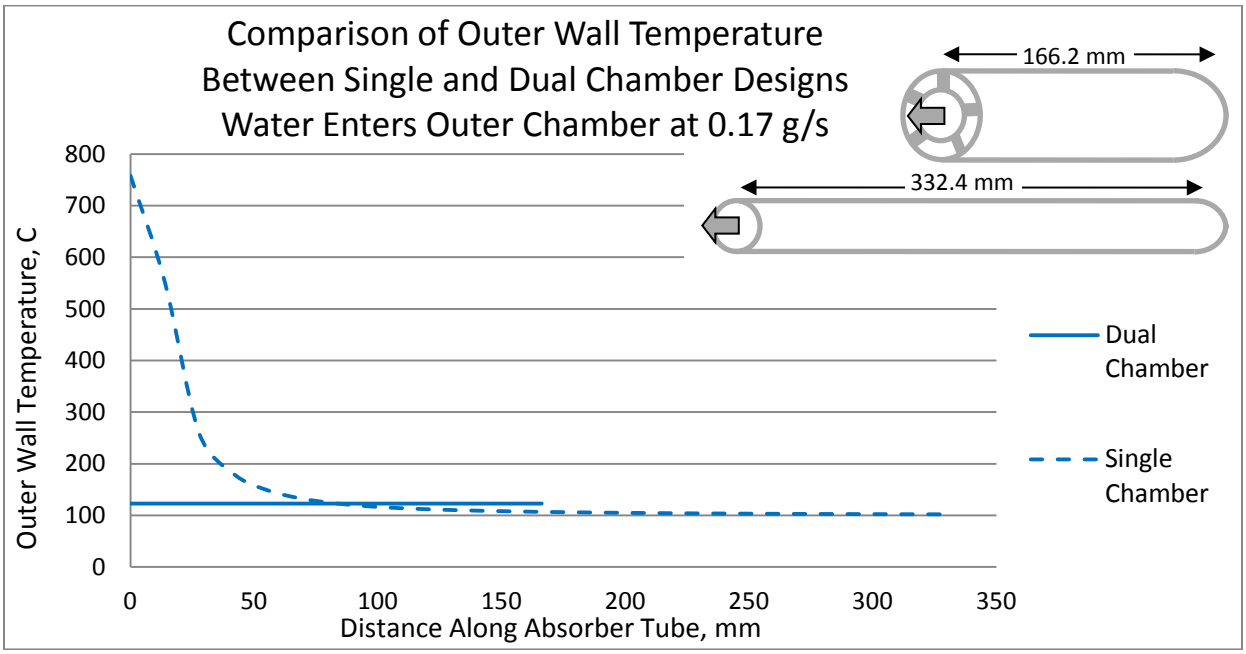

Figure 62: Comparison of single chamber and dual chamber computational outer wall temperatures for a mass flow rate of 0.17 g/s. Fluid enters the outer chamber and exits the inner chamber in the dual chamber design. The single and dual chamber designs have the same inlet fluid temperature, exit fluid temperature, and mass flow rate as presented in Table 5 to ensure the same heat input to both systems. The inner radius of the dual chamber is the radius of the single chamber design. The length of both fluid paths is the same so the absorber tube length of the dual chamber design is half the length of the single chamber design.

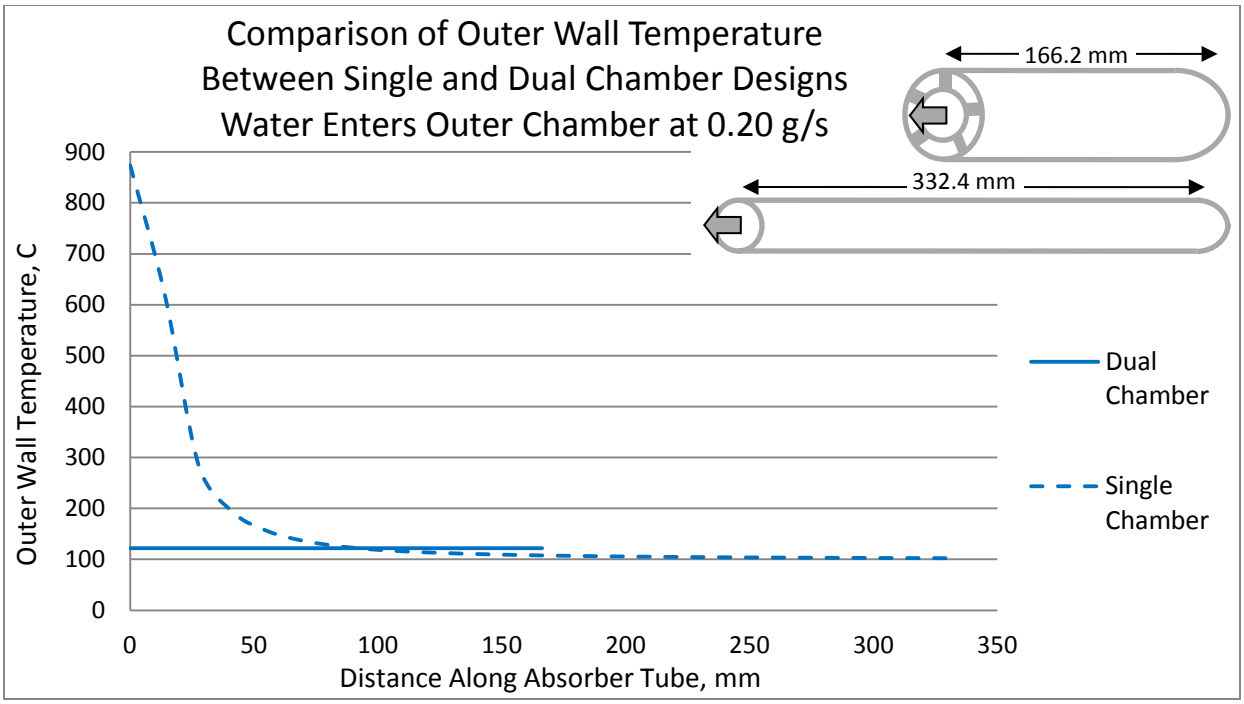

Figure 63: Comparison of single chamber and dual chamber computational outer wall temperatures for a mass flow rate of 0.20 g/s. Fluid enters the outer chamber and exits the inner chamber in the dual chamber design. The single and dual chamber designs have the same inlet fluid temperature, exit fluid temperature, and mass flow rate as presented in Table 5 to ensure the same heat input to both systems. The inner radius of the dual chamber is the radius of the single chamber design. The length of both fluid paths is the same so the absorber tube length of the dual chamber design is half the length of the single chamber design.

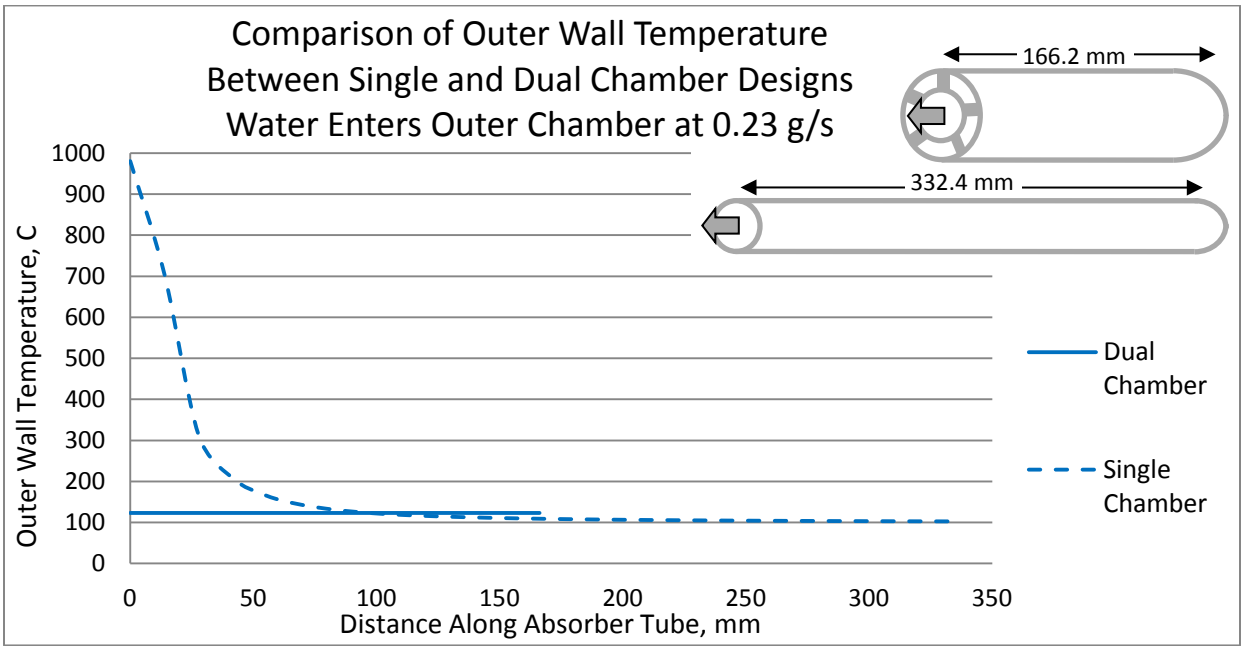

Figure 64: Comparison of single chamber and dual chamber computational outer wall temperatures for a mass flow rate of 0.23 g/s. Fluid enters the outer chamber and exits the inner chamber in the dual chamber design. The single and dual chamber designs have the same inlet fluid temperature, exit fluid temperature, and mass flow rate as presented in Table 5 to ensure the same heat input to both systems. The inner radius of the dual chamber is the radius of the single chamber design. The length of both fluid paths is the same so the absorber tube length of the dual chamber design is half the length of the single chamber design.

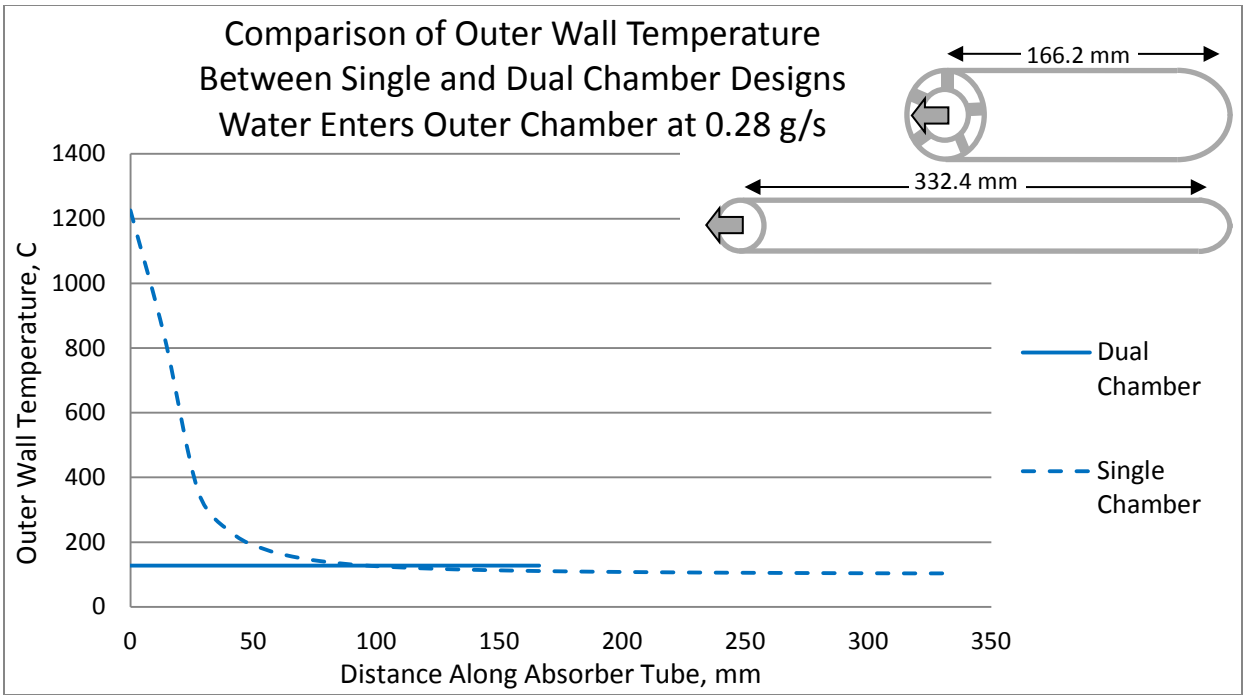

Figure 65: Comparison of single chamber and dual chamber computational outer wall temperatures for a mass flow rate of 0.28 g/s. Fluid enters the outer chamber and exits the inner chamber in the dual chamber design. The single and dual chamber designs have the same inlet fluid temperature, exit fluid temperature, and mass flow rate as presented in Table 5 to ensure the same heat input to both systems. The inner radius of the dual chamber is the radius of the single chamber design. The length of both fluid paths is the same so the absorber tube length of the dual chamber design is half the length of the single chamber design.

In order to better conceptualize the magnitude of improvement, please refer to Figs. 66-67. If a heat transfer coefficient to the surroundings is estimated as 5 W/m^2K (a typical value used for natural convection), Fig. 66 shows the amount of energy lost from the outer tube wall to the environment for each configuration. For any ambient heat transfer coefficient, Fig. 67 shows the percent reduction in heat loss when a single chamber design is replaced by either dual chamber design. The heat loss to the environment can be reduced by 10-60%. The best performance is found when water enters the outer chamber at the highest mass flow rate. This impressive improvement encourages further development of the dual chamber design.

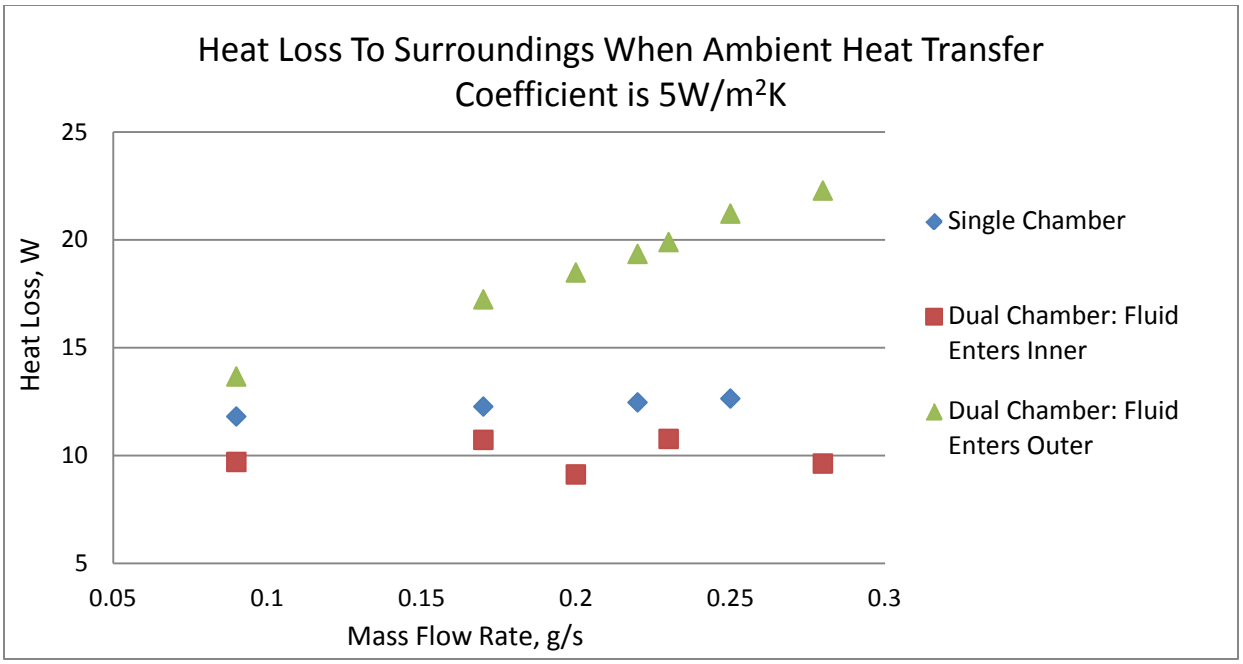

Figure 66: Heat loss comparison for multiple mass flow rates and design configurations (single chamber, dual chamber with fluid entering inner and outer chambers). For each mass flow rate considered, the single and dual chamber designs have the same inlet and exit fluid temperatures and mass flow rate to ensure the same heat input to the system. The inner radius of the dual chamber is the radius of the single chamber design. The length of both fluid paths is the same so the absorber tube length of the dual chamber design is half the length of the single chamber design. The heat loss is computed as sum of each isothermal segment where $Q_{loss} = hA(T_w - T_{amb})$. The wall temperature is the theoretical wall temperature. The ambient temperature is assumed to be 25C. The heat transfer coefficient is arbitrarily assigned 5 W/m^2K.

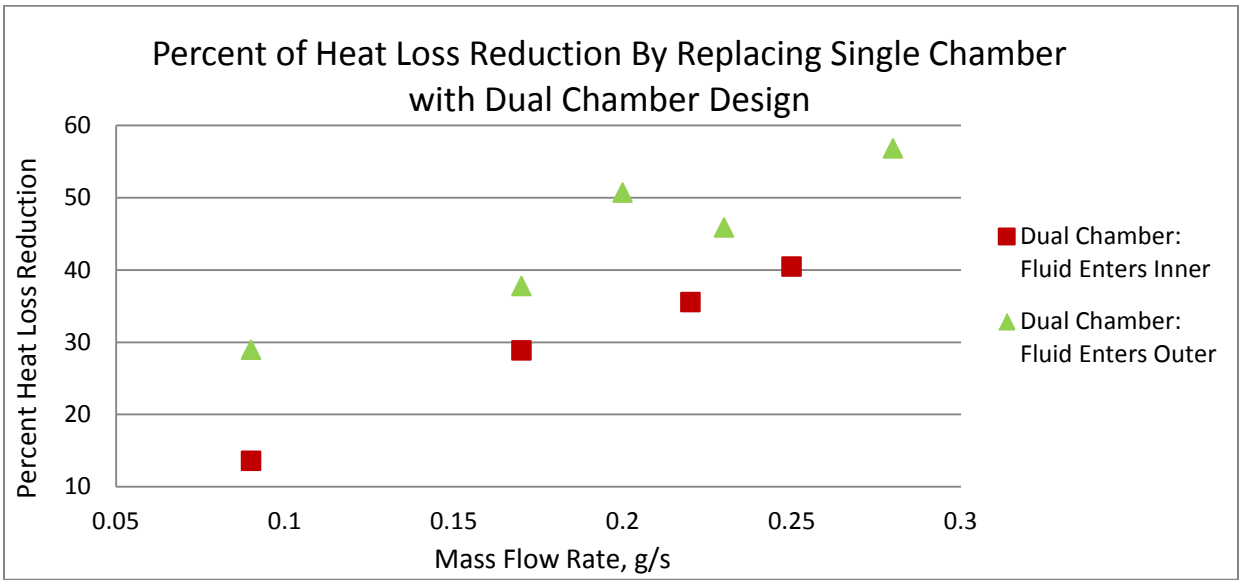

Figure 67: Percent reduction in heat loss for multiple mass flow rates when the single chamber design is replaced with the dual chamber design. Both configurations for fluid entering the inner and outer chamber are presented. For each mass flow rate considered, the single and dual chamber designs have the same inlet and exit fluid temperatures and mass flow rate to ensure the same heat input to the system. The inner radius of the dual chamber is the radius of the single chamber design. The length of both fluid paths is the same so the absorber tube length of the dual chamber design is half the length of the single chamber design. The heat loss is computed as sum of each isothermal segment where $Q_{loss} = hA(T_w - T_{amb})$. The wall temperature is the theoretical wall temperature. The ambient temperature is assumed to be 25C. The percent of heat loss reduction is calculated as $(Q_{loss,single} - Q_{loss,dual})/Q_{loss,single}*100\%$. The heat transfer coefficient is arbitrarily and drops out of the analysis.

Increase Pressure Losses

Tables 9 – 12 show the theoretical pressure losses for the dual chamber design with water entering either the inner or outer chamber and the corresponding single chamber design. Each theoretical analysis was done based on the experimentally tested conditions. As can be seen in the tables, the pressure losses in all configurations is quite small, less than 2 Pa. Because of this, the pressure drop was undetectable using the experimental equipment.

An increase in mass flow rate, regardless of design configuration, results in an increase of pressure losses. This behavior is as would be expected based on fundamental fluid dynamics. From the Darcy-Weisbach equation, it is clear that the pressure loss in pipes is proportional to the inverse of the velocity squared. Hence, as the mass flow rate increases so does the velocity causing a greater pressure loss. The pressure loss seems to be greatest in the dual chamber design with the water entering the inner chamber. In this configuration, the outer chamber is dominated by high quality saturated mixture and superheated gas. The low density vapor is traveling at a high velocity through an area with a very small hydraulic diameter causing greater losses to friction.

The difference in pressure losses between the single and dual-chamber designs is greatest at low mass flow rates. At a mass flow rate of 0.09 g/s the dual chamber design with fluid entering the inner chamber experiences over five times the pressure losses of a single chamber under similar conditions. For the mass flow rates tested, the dual-chamber design experiences 166% - 513% the pressure loss of the single chamber design. Although relative to the single chamber design the pressure drop of the dual chamber designs are much greater, it is important to note that the magnitude of the pressure losses are quite small (less than 2 Pa). For most practical applications the benefit of the heat loss reduction in the dual-chamber design will likely outweigh the increased pressure losses.

Table 9: Pressure Losses For Dual Chamber With Fluid Entering Outer Chamber Under Experimentally Tested Conditions

Mass Flow Rate (g/s)	Friction in inner chamber (Pa)	Friction in outer chamber (Pa)	Form Drag From Fins (Pa)	Bend (Pa)	Total (Pa)
0.09	0.0342	0.2837	0.0001	0.0007	0.3187
0.17	0.0708	0.7636	0.0008	0.0018	0.8370
0.20	0.0851	0.8276	0.0005	0.0022	0.9154
0.23	0.1020	0.9134	0.0007	0.0030	1.0191
0.28	0.1369	1.1585	0.0011	0.0053	1.3018

Table 10: Pressure Loss Comparison Between Single Chamber and Dual Chamber Design With Fluid Entering Outer Chamber

Mass Flow Rate (g/s)	Single Chamber Design (Pa)	Dual Chamber Design (Pa)	Percent Difference
0.09	0.0797 Pa	0.3187	300%
0.17	0.2047	0.8370	309%
0.20	0.2372	0.9154	286%
0.23	0.3326	1.0191	206%
0.28	0.4896	1.3018	166%

Table 11: Pressure Losses For Dual Chamber With Fluid Entering Inner Chamber Under Experimentally Tested Conditions

Mass Flow Rate (g/s)	Friction in inner chamber (Pa)	Friction in outer chamber (Pa)	Form Drag From Fins (Pa)	Bend (Pa)	Total (Pa)
0.09	0.0028	0.4817	0.0003	0.0001	0.4849
0.17	0.0058	0.9189	0.0009	0.0003	0.9259
0.22	0.0080	1.2051	0.0015	0.0006	1.2152
0.25	0.0098	1.4329	0.0020	0.0009	1.4456

Table 12: Pressure Loss Comparison Between Single Chamber and Dual Chamber Design with Fluid Entering Inner Chamber

Mass Flow Rate (g/s)	Single Chamber Design (Pa)	Dual Chamber Design (Pa)	Percent Difference
0.09	0.0791	0.4849	513%
0.17	0.2050	0.9259	352%
0.22	0.3119	1.2152	290%
0.25	0.4089	1.4456	254%

III. Radial Inflow Turbine Analysis

Motivation

Recent studies suggest that small scale (5-10kW) distributed solar Rankine combined heat and power could be a viable renewable energy strategy for displacing fossil fuel use in residential buildings, small commercial buildings, or developing rural communities. One of the primary obstacles of scaling down solar Rankine technology to this level is finding an appropriate expander design. This chapter considers the radial-inflow turbine for such an application. Although well-tested methodologies exist for design analysis of radial inflow turbines, existing analysis tools are generally focused on machines using a combustion gases in a Brayton cycle. Use of Rankine cycle working fluids under conditions optimal for small scale Rankine solar systems result in turbine operating conditions that can be dramatically different from those in combustion-based Brayton cycle power systems. This investigation explored how analysis tools developed by NASA and others for conventional Brayton cycle power systems can be adapted to analyze and design radial inflow expanders for small scale Rankine solar combined heat and power systems. Using a 1D model derived from analysis methodologies used by NASA for conventional aerospace gas turbine power applications, the effect of reduced power output on performance is explored. Since the model contains several non-dimensional variables, a variety of geometries are surveyed, and performance sensitivity to various geometric parameters is observed. The interplay between radial inflow turbine performance and cycle efficiency for the system is examined in detail. Several fluids are compared to access how critical temperature and the shape of the saturation dome affect thermodynamic performance of the cycle and efficiency of the turbine. Conclusions regarding optimal fluids and geometric parameters for the radial-inflow turbine are discussed.

Literary Review

As outlined in the 2005 Dept. of Energy publication “Basic Research Needs for Solar Energy Utilization,” (Lewis & Crabtree, 2005) moderate temperature distributed solar thermal is an

area where there is potential for significant innovation to reduce the cost of solar energy. The commercial efficiencies of solar thermal systems are at 20-35%. This offers a significant advantage over photovoltaics which currently have efficiencies between 10-20% (Mills, 2004). The case for small-scale solar Rankine systems is strongest when considering the use of rejected heat in a combined heat and power configuration. In this case, solar efficiencies in excess of 60% (combined heat and power) are possible with concentrating solar collector efficiencies of 80% at moderate temperatures (150-450°C) (Kalogirou, 2004) (Kaushika, 1993). Thermal demands worldwide, including space heating and cooling, are a large fraction of total energy demands for customers using less than 10 kW peak power. Energy in the form of heat can also be stored in a more cost effective manner than electricity can be stored. Solar thermal technology can be manufactured using abundant and easily processed engineering materials such as steel, glass and rubber. For these reasons, solar thermal combined heat and power has potential to be exceptionally low-cost and environmentally benign.

One of the leading challenges in solar thermal technology is designing an appropriate expander. The radial inflow turbine deserves further consideration for distributed applications owing to its potential high efficiency and reasonable pressure ratios achievable at small scales (Jones A. , 1996). A number of investigators have developed fluid mechanical models of the radial inflow turbine for air-breathing systems. Glassman (Glassman, 1976) developed a one dimensional geometry-parameterized computer-based analysis for designing radial inflow turbines for NASA. Whitfield (Whitfield, 1990) developed a non- dimensional design procedure for radial inflow turbines based on best industry practices, and Spence (Spence & Artt, 1997) tested a representative design with various stators. A computational fluid dynamics model (CFD) was proposed and tested by Hoffren (Hoffren, Talonpoika, Larjola, & Siikonen, 2002) to demonstrate to desirability of using high molecular weight organic fluids with supersonic inlet conditions in the hundreds of kilowatts size scale. However, the analysis of the radial inflow turbine in small-scale (<10kW) Rankine cycles for non-air-breathing systems has been limited. Aoun (Aoun, 2009) discusses the potential of using various organic fluids in small-scale combined heat and power production. However, he does not take into account that altering the working fluid would affect the turbine efficiency. He only compares thermal efficiency of a Rankine cycle based on an isentropic turbine.

In this chapter, a comprehensive analysis and design optimization for radial inflow turbines with peak power outputs of between 5 and 10kW using a variety of organic fluids is discussed. This offers improvement over the current radial inflow turbine analyses limited to air-breathing systems. An idealized combined heat and power Rankine cycle is developed using the design methodology of Glassman (Glassman, 1976). A sensitivity analysis is performed using an iterative design procedure to find the parameters which most affect overall cycle thermal efficiency. As a one dimensional analysis, the Glassman model is simpler than CFD yet is a widely used design approach utilized by a number of turbine manufacturers, such as United Technologies. Then, this information is used to assess the impact on turbine and cycle efficiency of altering the working fluids for use in a small scale (<10 kW) radial inflow turbine for a solar thermal combined heat and power system.

Nomenclature

$cd_{2,t}$	Clearance to rotor exit tip diameter
c_p	Specific heat at constant pressure
i	Enthalpy
Δi_{id}	Ideal specific enthalpy difference
Δi_{shft}	Specific enthalpy difference of shaft
j	Sector number
N	Rotative speed
r_0r_{1a}	Ratio of stator inlet radius to rotor inlet radius
r_1r_{1a}	Ratio of stator exit radius to rotor inlet radius
$r_{2,h}r_{2,t}$	Ratio of rotor exit hub radius to rotor exit tip radius
$r_{2,t}r_{1a}$	Ratio of rotor exit tip to rotor inlet radius
$rV_{1a,ave}$	Ratio of rotor inlet angular momentum to average change in angular momentum
t_rh_{2m}	Ratio of rotor mean section trailing edge thickness to rotor exit passage height
n_s	Number of stator vanes
n_r	Number of rotor blades
P	Shaft power at turbine outlet
P_0'	Total pressure at stator inlet
P_2	Absolute pressure at rotor exit
P_{high}	High-side pressure
P_{low}	Low-side pressure
t_sh_1	Ratio of stator trailing edge thickness to stator height
T_0'	Temperature at stator inlet
v	Specific volume
w	Mass flow rate
α_0	Flow Angle at Inlet to Stator
α_1	Flow Angle at Exit to Stator
γ	Specific Heat Ratio
η_{th}	Thermal Cycle Efficiency
$\eta_{turbine}$	Turbine Efficiency

Cycle Definition

Fig. 68 shows a process diagram for a Rankine cycle. For a combined heat and power system, it is necessary that the rejected temperature from the Rankine cycle is high enough to be able to create usable heat. Typical household hot water is kept between 40^0C and 50^0C. A heat exchanger would be used between state points 4 and 1 so that the fluid in the closed Rankine cycle loop could condense while heating domestic hot water. To ensure a driving temperature difference of at least 15^0C, the temperature in the condenser was fixed at 65^0C. In other words, the minimum temperature of the Rankine cycle was fixed at 65^0C. Additionally, there is a constraint to the high-side temperature of the Rankine cycle. A temperature of 250^0C was

chosen as a fluid temperature that is reasonably achievable by low-cost tracking solar collectors (RawSolar, 2009). The operating temperature of the solar collector defines the peak temperature of the Rankine cycle. The following is a summary of the system constraints and idealizations of the Rankine cycle:

1. The minimum temperature is fixed at 65^0C.
2. The maximum temperature is fixed at 250^0C.
3. The inlet to the pump, point 1, is saturated liquid.
4. The pump is isentropic.
5. The turbine efficiency is based on modeling described later in this paper.
6. There is no pressure drop in the evaporator, condenser or pipes.
7. Just to the left of the saturation dome, the fluid is assumed to be incompressible.

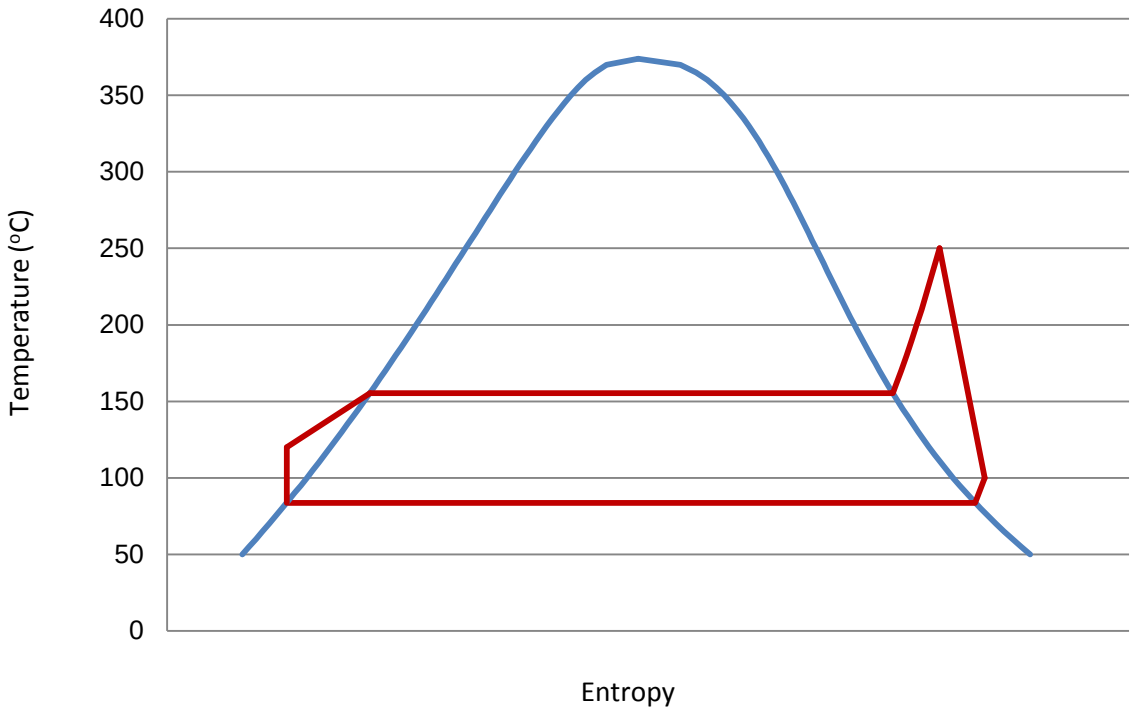

Figure 68: Process diagram of Rankine cycle based on stated assumptions.

Turbine Modeling

The basis of the turbine modeling came from "Computer Program for Design Analysis of Radial-Inflow Turbines" by Arthur Glassman (Glassman, 1976). It was sponsored through NASA and is currently available through NASA's technical library. For those interested in the details of this model, please refer to the original paper. To better visualize these parameters under consideration, refer to Fig. 69-70. These diagrams are reproductions from "Computer Program for Design Analysis of Radial-Inflow Turbines" by Arthur Glassman (Glassman, 1976).

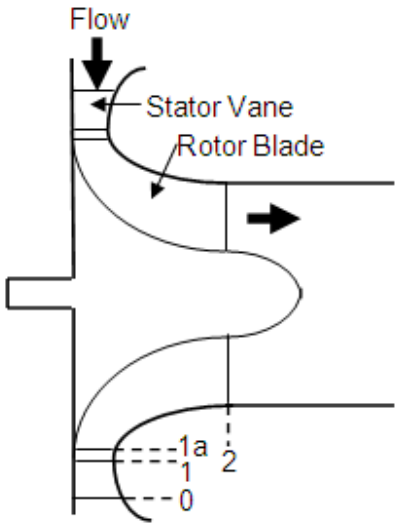

Figure 69: Schematic cross-section of radial inflow turbine

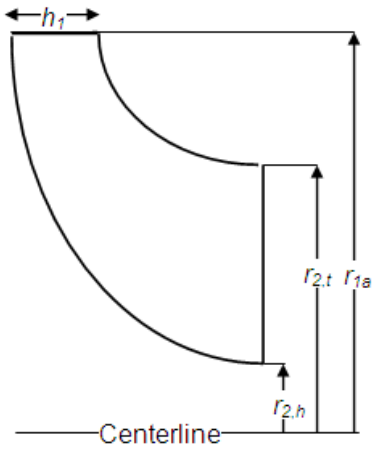

Figure 70: Rotor geometry model

Glassman's model assumes mean-line flow through the stator and equal span-fraction sectors through the rotor. The input design variables include power output, mass flow rate, inlet temperature and pressure, rotational speed, stator exit angle, rotor-exit-tip to rotor-inlet radius ratio, rotor-exit-hub to tip radius ratio, and the magnitude and radial distribution of rotor-exit tangential velocity. Glassman's model accounts for losses due stator and rotor boundary layers, tip clearance, disk friction and exit velocity. The model computes the total and static turbine efficiencies, and diameters, temperatures, pressures, velocities and flow angles at the stator inlet, stator exit, rotor inlet, and rotor exit. Glassman's model is converted into a Fortran program, which is available in his original paper.

Glassman's model uses ideal gas assumptions and has been widely used in air and combustion processes. In this paper, Glassman's model is being applied to super-heated vapor that, in some situations, approaches the saturation dome. As one approaches the saturation dome, the ideal gas laws become less valid. In order to account for this, some modifications have been made to the code. First, for convenience, the code was translated from Fortran into MATLab. Next, the gas constant is adjusted based on the molecular weight of the fluid under consideration. Lastly, the specific heat and viscosity of the vapor change from the turbine inlet to the turbine outlet. To account for this, we run Glassman's model at the specific heat and viscosity of the mean temperature and mean pressure. Originally, Glassman's model evaluated the specific heat and viscosity at the conditions of the inlet to the turbine. The error associated with assuming a fixed value for the specific heat and viscosity, as opposed to evaluating the properties as a function of temperature and pressure throughout the turbine, is insignificant. To verify this, water is evaluated twice using the case study conditions of Table 13. The first time, the turbine performance is evaluated at the specific heat and viscosity of the inlet to the turbine. This results in a turbine efficiency of 89.2%. The second time, the turbine performance is evaluated at the specific heat and viscosity of the outlet of the turbine. Here, the turbine efficiency is 89.4%. Changing the temperature and pressure that the specific heat and viscosity were evaluated corresponds to only a percent error of 0.22%. This error is cut in half by evaluating the specific heat and viscosity at the mean temperature and pressure with

the resulting turbine efficiency 89.3% for this case study. A flow chart is provided in Fig. 71 to show structure of the original Glassman model.

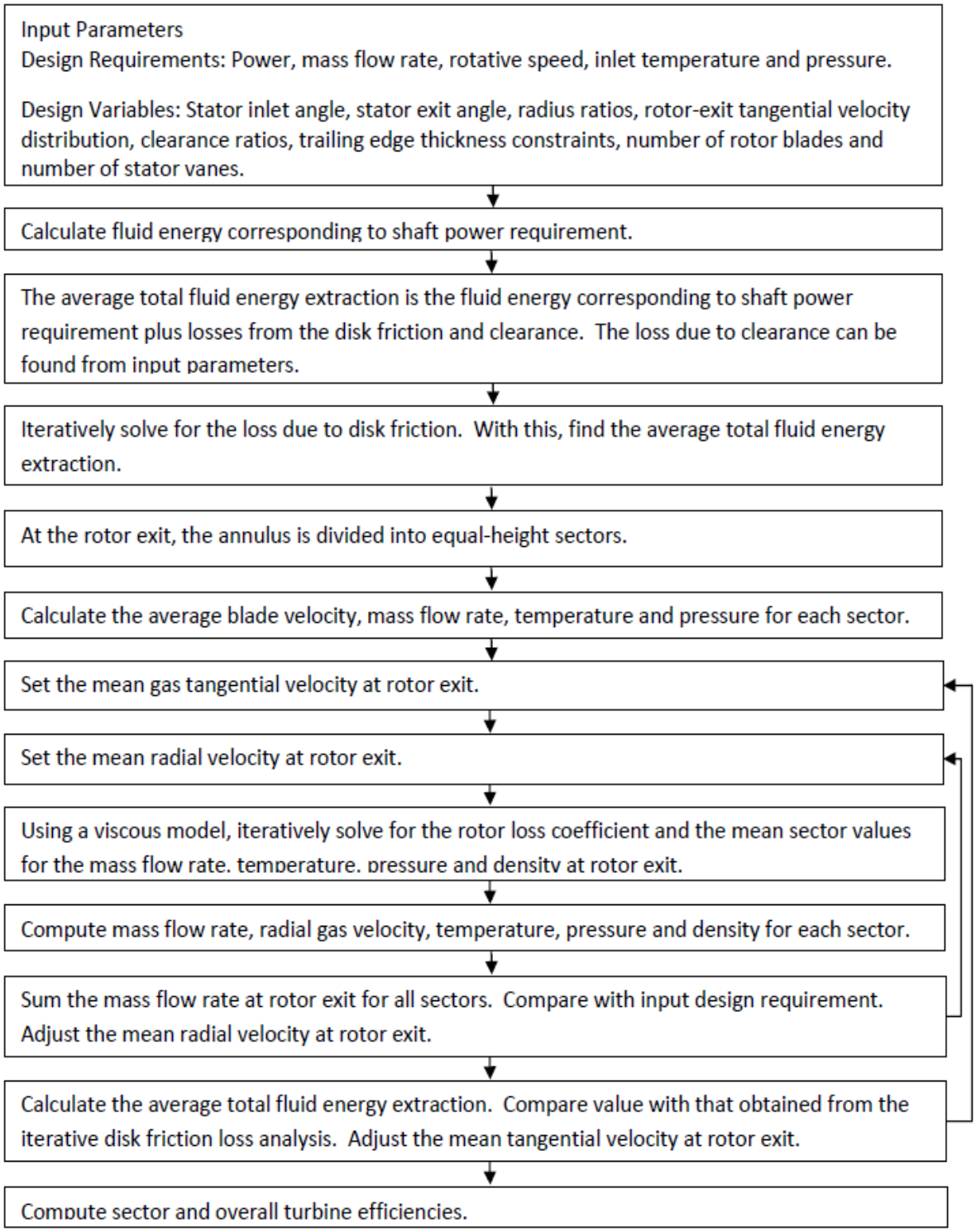

Figure 71: Flow chart of Glassman's model.

Determination of Turbine Efficiency

A lengthy explanation of how to compute the turbine efficiency is available in "Computer Program for Design Analysis of Radial-Inflow Turbines" by Arthur Glassman (Glassman, 1976). For the reader's convenience, the basic equation is provided below.

$$\eta_{turbine} = \frac{\Delta i_{shft}}{\sum_j \frac{w_j}{w} \Delta h_{id,j}} \tag{102}$$

Where

$$\Delta i_{shft} = \frac{c_p P}{w} \tag{103}$$

$$\Delta i_{id,j} = c_p T_o' \left[1 - \left(\frac{P_{2,j}}{P_o'} \right)^{(\gamma-1)/\gamma} \right] \tag{104}$$

Determination of Cycle Efficiency

Based on the cycle definition and the turbine model, the following approach was used to calculate the cycle efficiency.

1. Since the minimum cycle temperature is fixed, one can compute the low-side pressure as the saturation pressure at 65^0C.
2. Guess the high-side pressure, specific heats, and viscosity.
    a. Run the modified Glassman's program using the maximum cycle temperature (250^0C) and the guessed high-side pressure as turbine inlet conditions.
    b. The modified Glassman program outputs the temperature and pressure at the turbine exit. Use this and part a to compute the average temperature and pressure across the turbine. Determine the specific heats and viscosity at this averaged temperature and pressure.
    c. Modify the specific heats and viscosity and iterate from part a until the guessed specific heats and viscosity correspond to those at the average temperature and pressure of the turbine.
3. Compare the pressure at the turbine exit found in part 2 with the low-side pressure computed in part 1.
    a. If the two pressures differ by more than 0.2%, adjust the high-side pressure guess and repeat part 2.
    b. If not, then the high-side pressure, turbine outlet temperature and turbine efficiency have been found using the modified Glassman model.
4. Calculate enthalpies at each state point.
    a. At state point 1, the enthalpy, i_1, is the enthalpy of saturated liquid at 65^oC. Also find the specific volume of saturated liquid at 65^oC, v_1.
    b. Based on the incompressible liquid assumption noted as 7 in the cycle definition, the enthalpy of state point 2 can be computed by constant volume work:

$$i_2 = i_1 + v_1 (P_{high} - P_{low}) \tag{105}$$

c. At state point 3, the temperature is 250°C and the pressure is the high-side pressure. This is enough information to find the enthalpy of the superheated vapor, i_3.

5. At state point 4, the pressure was found in part 1 and the temperature of the turbine outlet in part 3. This is enough information to find the enthalpy of the superheated vapor, i_4.
6. Calculate the thermal efficiency of the cycle.

$$\eta_{th} = 1 - \frac{i_4 - i_1}{i_3 - i_2} \tag{106}$$

EES, software containing the thermodynamic properties of many fluids, was used to compute the thermodynamic efficiency of the Rankine cycle. A few fluids under investigation, such as benzene, were not available in the EES software. These thermodynamic properties were taken from the National Institute of Standards and Technology.

Sensitivity to Input Parameters

The modified Glassman model has seventeen input parameters. Trying to optimize all seventeen while comparing various fluids would be quite cumbersome. The most practical approach is to perform a sensitivity analysis to determine which input parameters have the greatest effect on thermal performance and then optimize only these parameters. Water was chosen as the working fluid in this analysis.

Table 13 shows all seventeen input parameters and their corresponding case study values. Although the total pressure at stator inlet, P_0', is an input parameter to the Glassman model, it is iteratively found based on the pressure at the rotor outlet being fixed at the saturation pressure at 65°C. This iterative approach is discussed in "Determination of Cycle Efficiency." Also, the total absolute temperature at the stator inlet, T_o', is fixed as a design constraint at 250°C. This is based on the operating temperature of Raw Solar's concentrating dishes. Hence, regardless of the sensitivity the model has to these two input parameters, P_0' and T_o', they will not be altered for optimizing thermal performance.

Table 13: Case Study Values for Input Parameters of the Modified Glassman Model for Radial Inflow Turbines

Input Parameter	Case study Value
P_0'	Iteratively Determined
T_0'	250°C
w	No Case study Value
$cd_{2,t}$	0.00312
$r_1 r_{1a}$	1.111
$rV_{1a,ave}$	0.963
$t_r h_{2,m}$	0.1557
$t_s h_1$	0.1007
α_0	45°
α_1	78°
n_r	9
n_s	15
N	45000 rpm
P	10 kW
$r_0 r_{1a}$	1.292
$r_{2,h} r_{2,t}$	0.5
$r_{2,t} r_{1a}$	0.5

Mass Flow Rate

Holding constant all the input parameters listed in Table 13 at their case study values, the mass flow rate was varied. As can be seen in Figs. 72-74, the mass flow rate significantly alters thermal performance. As the mass flow rate is decreased, there is an increase in both turbine efficiency and pressure drop. Both of these factors contribute to the improved thermal efficiency with a decrease in mass flow rate as seen in Fig. 74. The figures show only a limited range of mass flow rates. This is because outside this range the fluid approached sonic conditions and the modified Glassman model is limited to sub-sonic regimes. However, within this limited range of convergence, the thermal efficiency changed by 34% varying from a thermal efficiency of 3.23% to 4.32%.

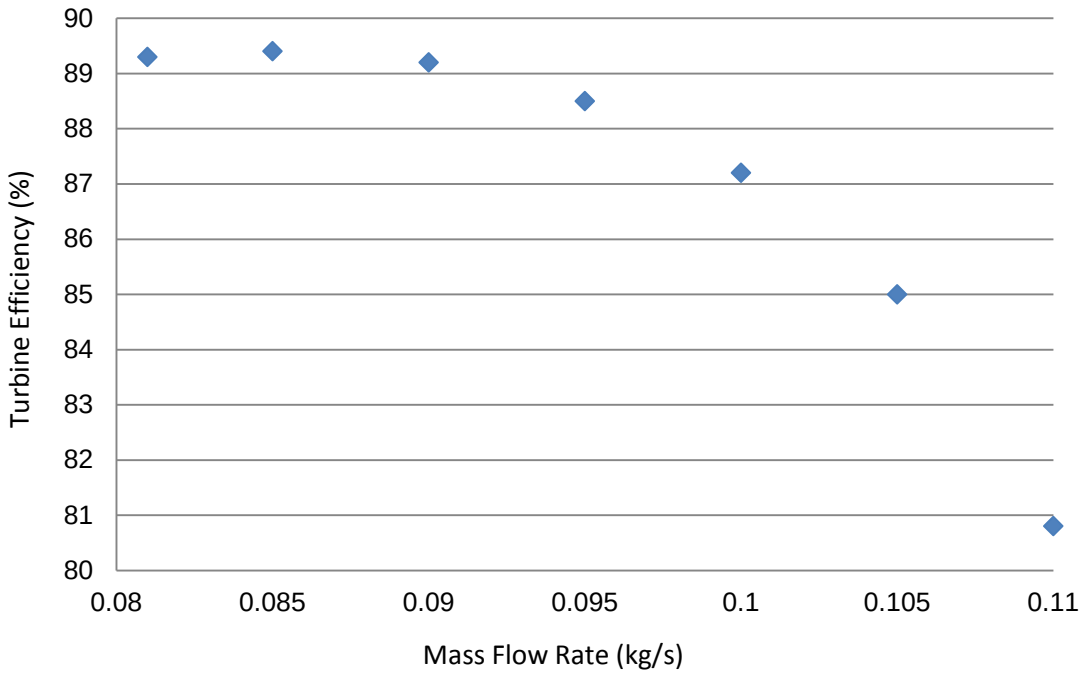

Figure 72: Effect of mass flow rate on turbine efficiency. All other parameters held at case study values. Water is the operating fluid.

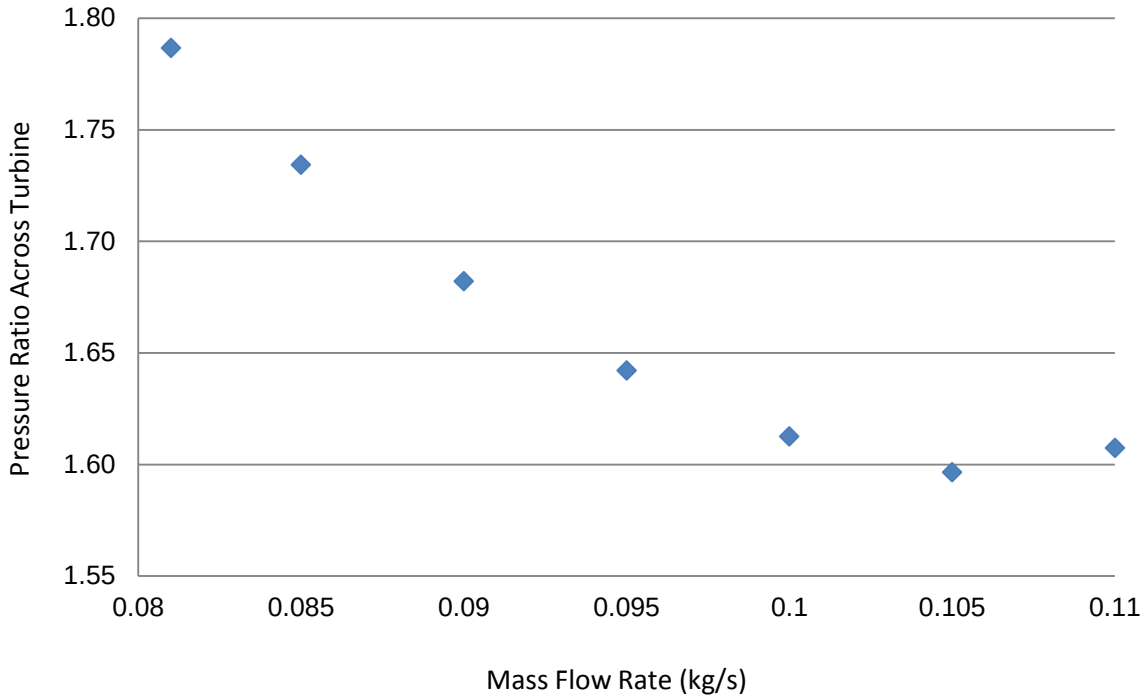

Figure 73: Effect of mass flow rate on pressure drop across the turbine. All other parameters held at case study values. Water is the operating fluid.

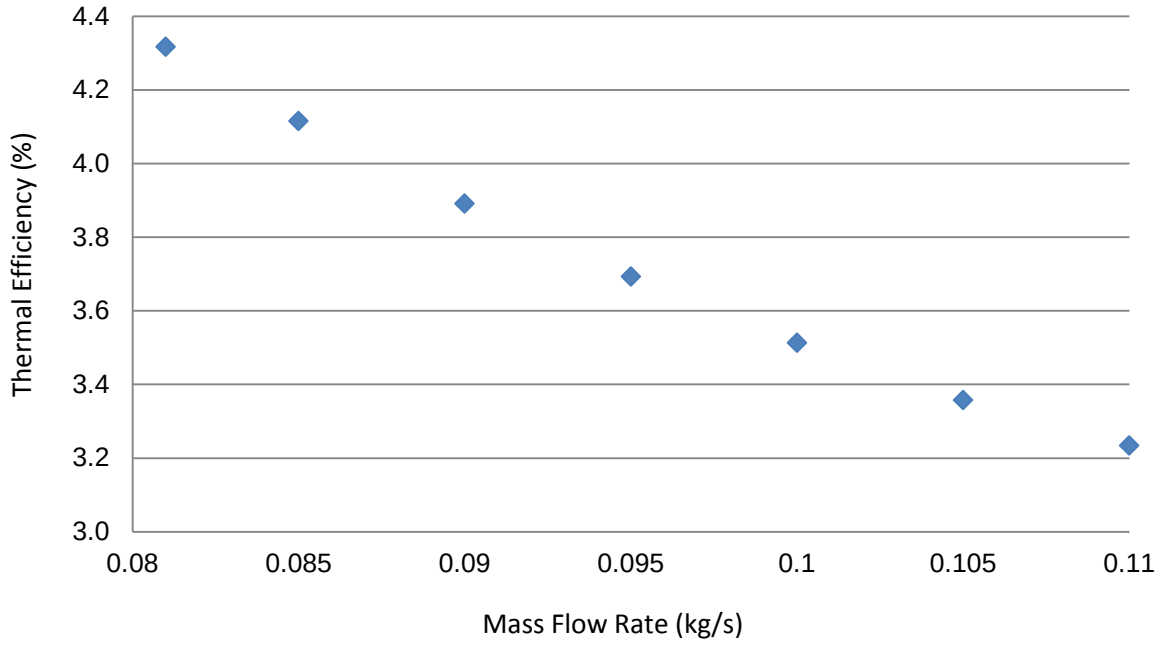

Figure 74: Effect of mass flow rate on thermal efficiency. All other parameters held at case study values. Water is the operating fluid.

Appropriately Fixed Input Parameters

The next five input parameters in Table 13, $cd_{2,t}$, r_1r_{1a}, $rV_{1a,ave}$, $t_rh_{2,m}$ and t_sh_1, are appropriately fixed input parameters. $cd_{2,t}$, r_1r_{1a} both represent clearances. The case study values chosen are appropriate for industrial use. Thermal performance could be increased by decreasing either of these. However, this would make it more difficult to manufacture and the rotor would need to be designed for very little vibration. The next parameter, $rV_{1a,ave}$, is widely used to estimate the change in angular momentum through the turbine. The last two parameters, $t_rh_{2,m}$ and t_sh_1, both incorporate trailing edge thicknesses. Similar to the arguments regarding clearances, there are manufacturing limitations to how thin a trailing edge can be made.

Sensitivity Analysis of Remaining Input Parameters

Due to the high sensitivity of thermal efficiency to mass flow rate and the limited range of convergence, the remaining input parameters are studied coupled with mass flow rate. Each of the remaining input parameters is varied while keeping all other input parameters constant at the case study values. The mass flow rate is then minimized for each variation of the input parameter under consideration to provide the largest thermal efficiency for each variation. Each parameter is varied by at least 50% as convergence allows. Figs. 88 – 96 in the appendix show the sensitivity analysis of the remaining nine input parameters in Table 13. Water remained the operating fluid.

A summary of the figures in the appendix are provided in Table 14 below for your convenience. When all case study values in Table 13 are used and the mass flow rate is minimized, the thermal efficiency is found to be 4.317%. When the input parameter under consideration is varied, the variations create different thermal efficiencies. The middle column of Table 14 shows the difference in thermal efficiency between the parameter change that leads to the

greatest change in thermal efficiency and the case study thermal efficiency of 4.317%. The leftmost column in Table 14 shows the percent change in the thermal efficiency, which is the middle column divided by the case study thermal efficiency. The figures in the appendix plot this percent change in thermal efficiency. A larger percentage implies that it has more influence that input parameter has on the thermal performance. These input parameters are coupled with mass flow rate alone. This analysis doesn't take into account other possible couplings. However, this preliminary analysis does show three parameters that seem to more significantly alter the thermal performance than the others. N, $r_{2,h}r_{2,t}$ and $r_{2,t}r_{1a}$ all altered the thermal efficiency by over 20% when coupled with mass flow rate. The other six parameters altered the thermal efficiency by less than 10%. Since this is significantly less than the other three, these six parameters will be fixed at their case study values. Increasing the rotative speed, N, yields improved thermal performance. However, increasing the rotative speed can represent a safety hazard that would require a more extensive design. Because of this, the rotative speed is also fixed at its case study value. Ultimately, the result of the sensitivity analysis is that $r_{2,h}r_{2,t}$ and $r_{2,t}r_{1a}$ coupled with mass flow rate most greatly affect thermal performance. To optimize a turbine design these will be varied and all other fixed at their case study values.

Table 14: Effect on Thermal Performance when Input Parameters Varied by at Least 50%

Input Parameter	Greatest Difference in Thermal Efficiency from Case study Value	Percent Change in Thermal Efficiency
α_0	0.002	0.05%
α_1	0.375	8.69%
n_r	0.360	8.34%
n_s	0.003	0.07%
N	1.151	26.7%
P	0.376	8.71%
$r_0 r_{1a}$	0.002	0.05%
$r_{2,h}\, r_{2,t}$	0.992	23.0%
$r_{2,t} r_{1a}$	0.932	21.6%

Fluid Selection

Preliminary Analysis

An optimized analysis of many fluids done by varying the mass flow rate, $r_{2,h}r_{2,t}$ and $r_{2,t}r_{1a}$ would be very time consuming. Therefore, to begin, nine fluids were selected for preliminary analysis. These initial fluids were selected because they provide information across a spectrum of critical temperatures. They also vary in the type of fluid. Five of the fluids are wet: water, ammonia, methanol, R12 and R143a. Four of the fluids are dry: Toluene, R11, R123 and RC318. A wet fluid is one in which the vapor curve of the saturation dome on the temperature-entropy plot has a negative slope. In contrast, a dry fluid has a positive slope at some points along the vapor curve. To begin, all input parameters are fixed at the case study values designated in Table 13. Only the mass flow rate is varied. Figs. 75-81 show the thermal efficiency obtained for each fluid plotted against various fluid properties. This is done to identify any trends between these fluid properties and thermal performance in the system under investigation.

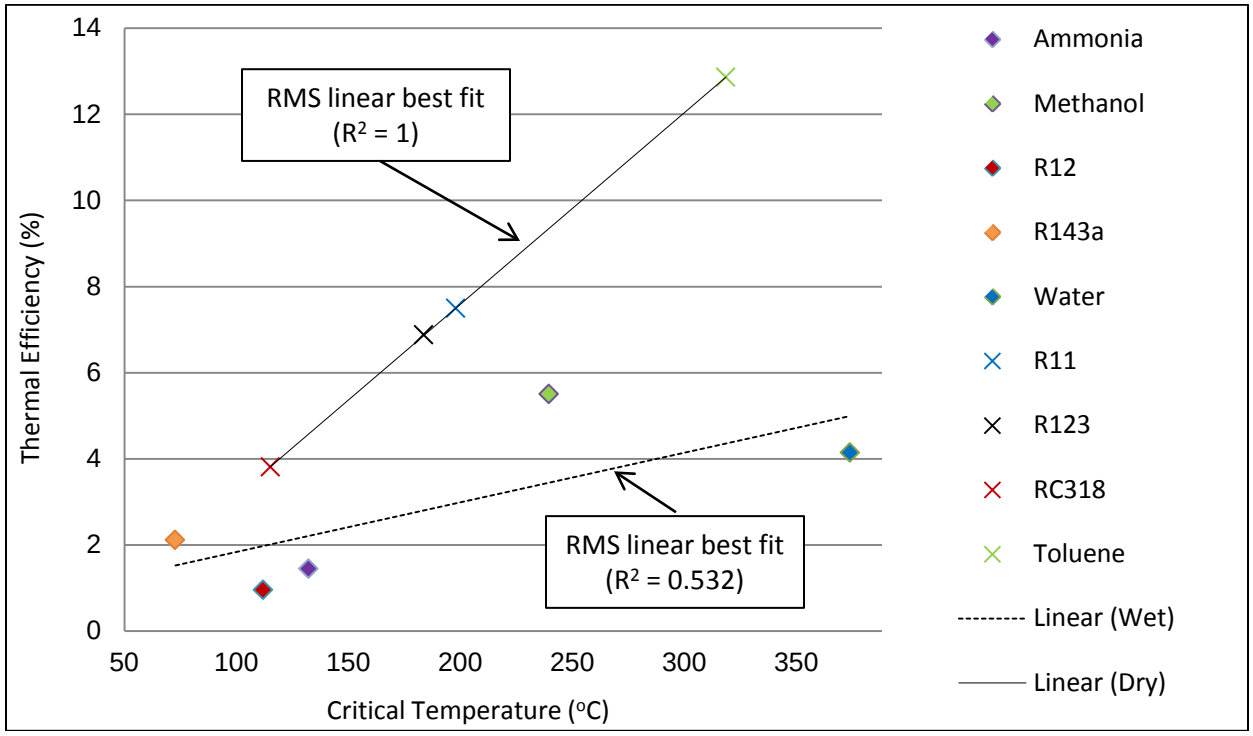

Figure 75: Thermal efficiency of preliminary fluids plotted against critical temperature. Wet fluids are designated by diamonds and dry fluids by x's.

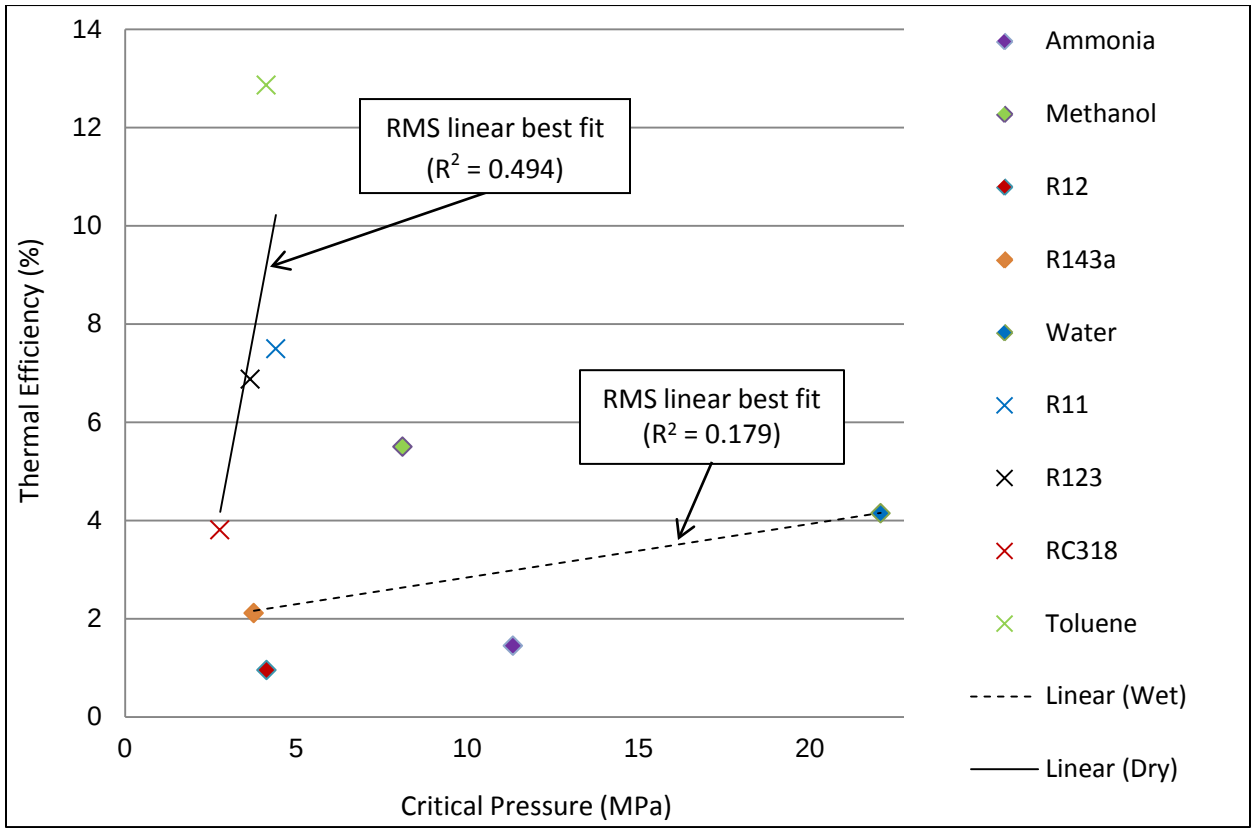

Figure 76: Thermal efficiency of preliminary fluids plotted against critical pressure. Wet fluids are designated by diamonds and dry fluids by x's.

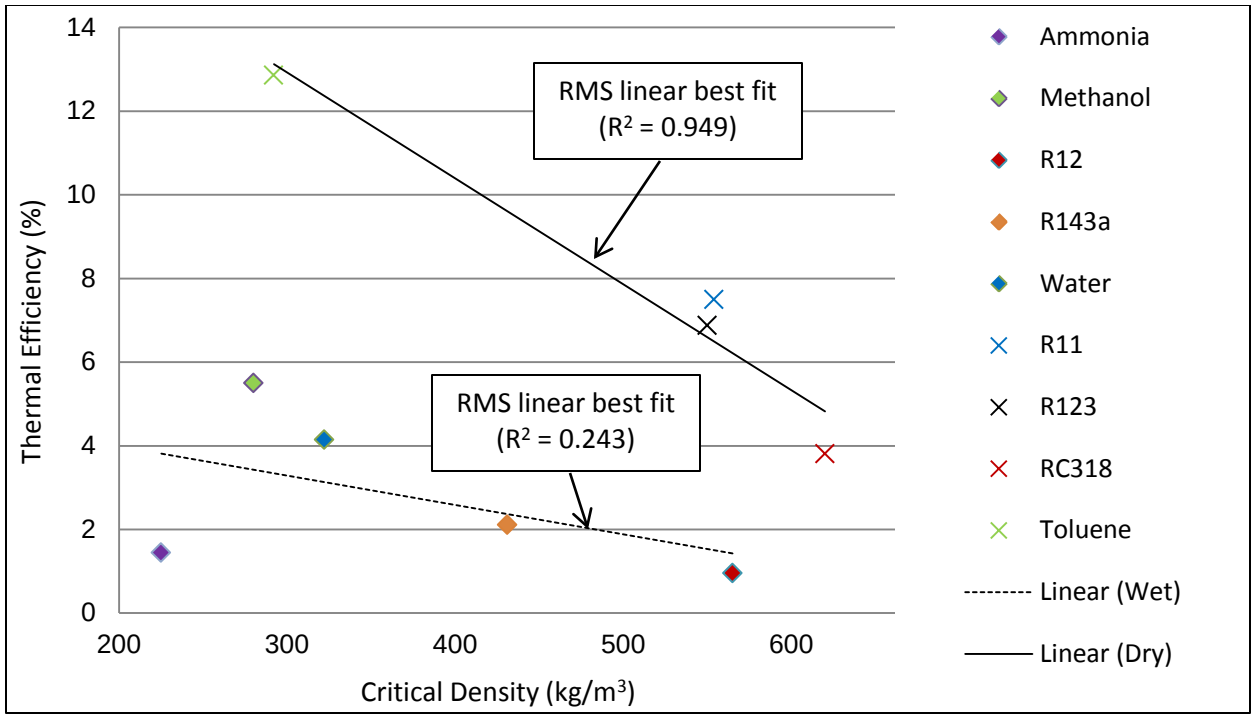

Figure 77: Thermal efficiency of preliminary fluids plotted against critical density. Wet fluids are designated by diamonds and dry fluids by x's.

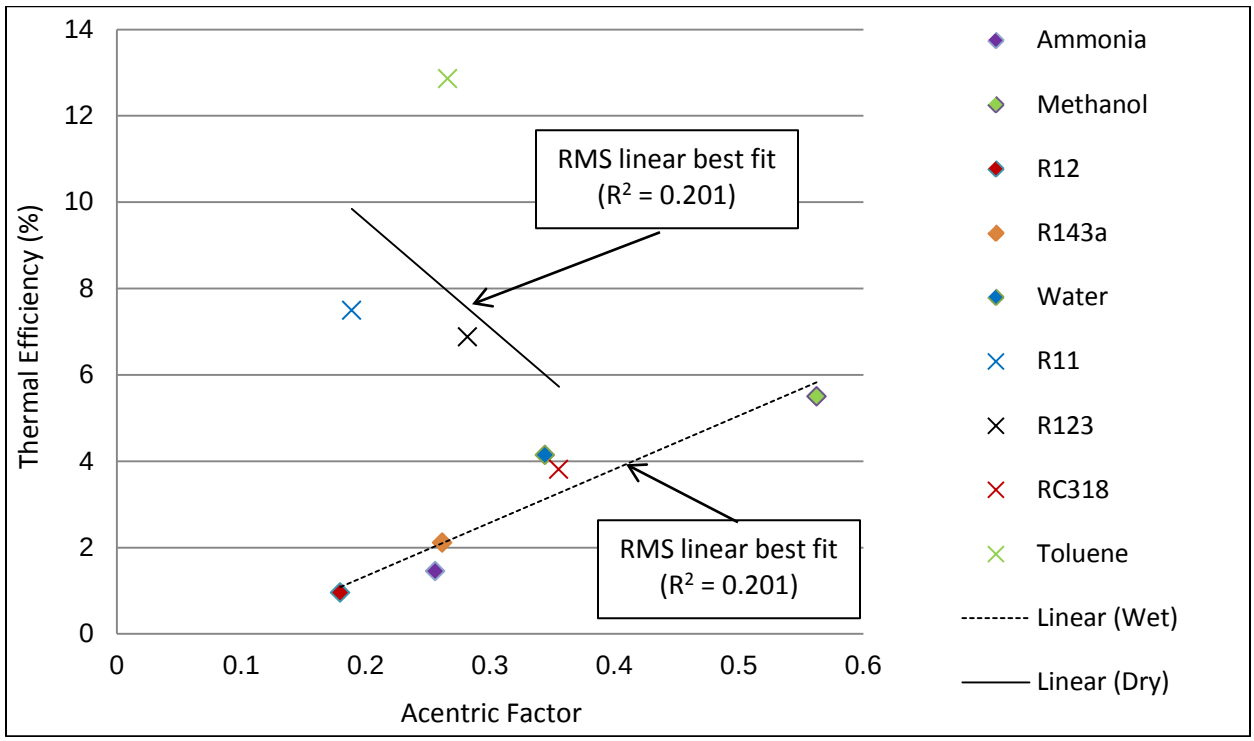

Figure 78: Thermal efficiency of preliminary fluids plotted against acentric factor. Wet fluids are designated by diamonds and dry fluids by x's.

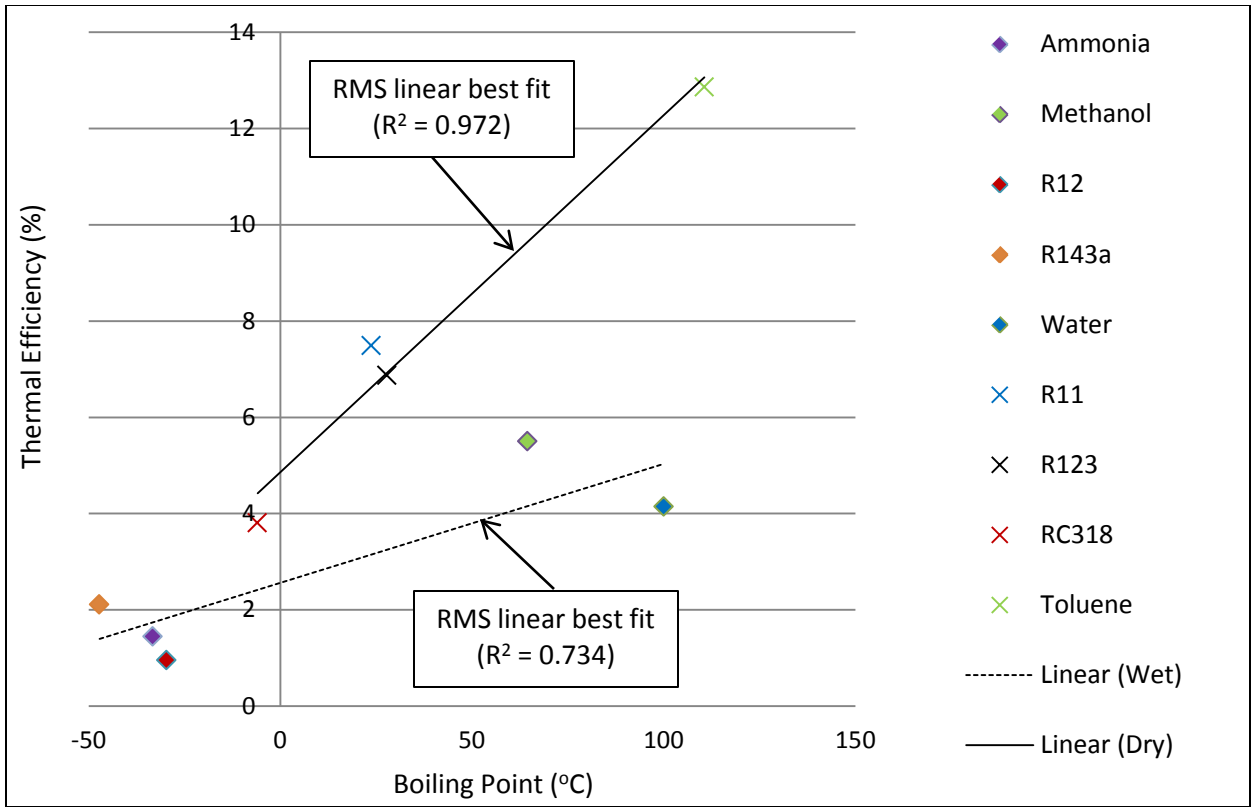

Figure 79: Thermal efficiency of preliminary fluids plotted against normal boiling point. Wet fluids are designated by diamonds and dry fluids by x's.

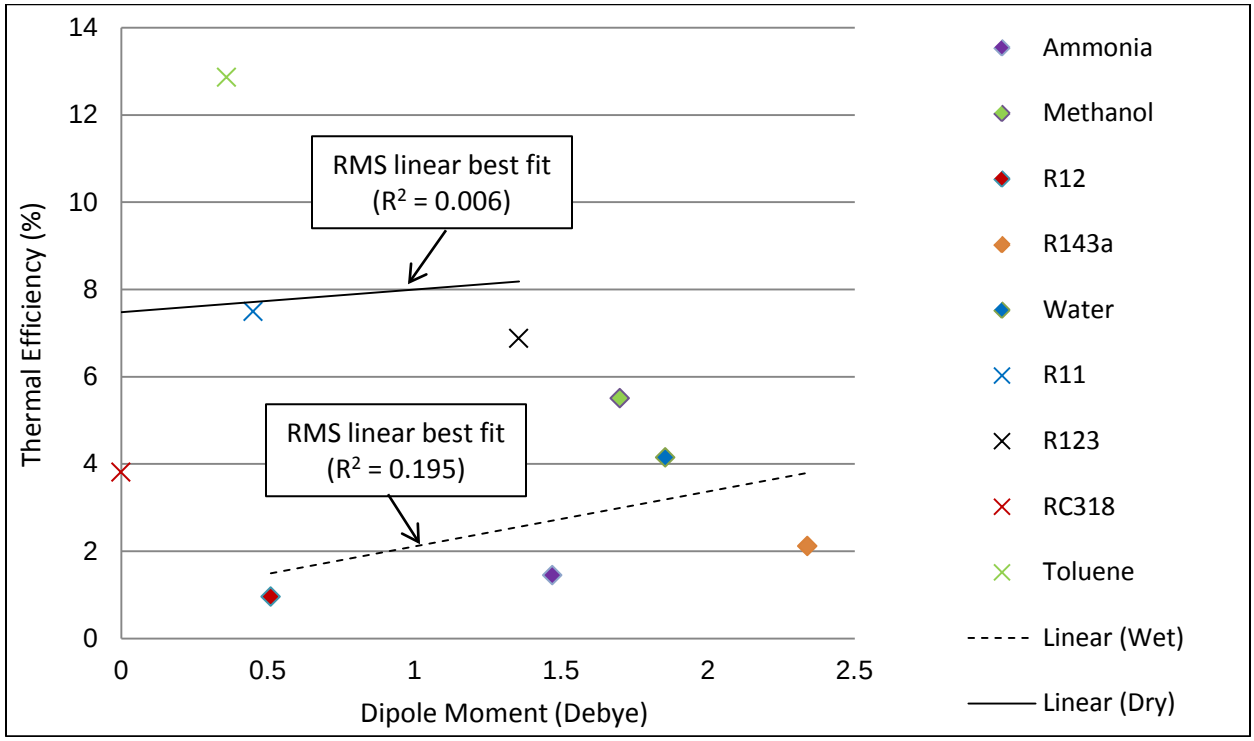

Figure 80: Thermal efficiency of preliminary fluids plotted against dipole moment. Wet fluids are designated by diamonds and dry fluids by x's.

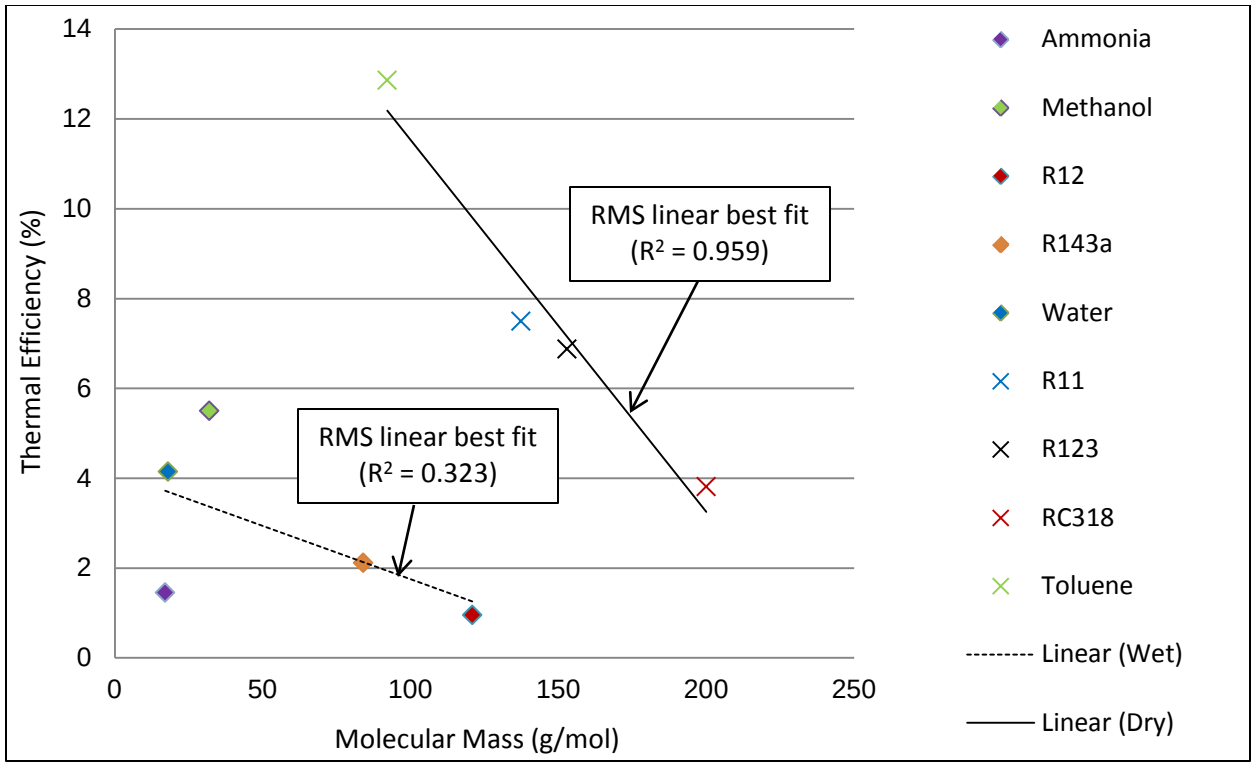

Figure 81: Thermal efficiency of preliminary fluids plotted against molecular mass. Wet fluids are designated by diamonds and dry fluids by x's.

A linear regression for both wet and dry fluids can be seen in each of these figures. Along with the regression, the coefficient of determination, R^2, is displayed. The coefficient of determination represents the percent of data that is closest to the line of best fit. For example, if R^2 is 0.9 then 90% of the total variation in the property along the y-axis can be explained by the linear relationship. A coefficient of determination of 0.9 or higher represents strong correlation. Using this as a standard, there is strong linear correlation for thermal efficiency of dry fluids against the following fluid properties: critical temperature, critical density, normal boiling point, and molecular mass. The strongest correlation exists for critical temperature. These fluid properties are not necessarily independent. Fluids with high critical temperature and low molecular mass often have low critical density and high normal boiling point. Dry fluids typically had better thermal efficiency then wet fluids. Wet fluids didn't show as strong correlations as dry fluids. Potential fluids to be examined in the optimal thermal performance analysis are dry fluids with high critical temperature and low molecular mass.

Extended Analysis of Top Performing Preliminary Fluids

During the preliminary analysis, all input parameters to the modified Glassman model for the radial-inflow turbine are fixed at the case study values in Table 13. Only mass flow rate is varied. In the sensitivity analysis, it was determined that mass flow rate, $r_{2,h}r_{2,t}$ and $r_{2,t}r_{1a}$ all significantly affect the thermal performance. Before the conclusions of the preliminary analysis are studied, the effect of including variations of $r_{2,h}r_{2,t}$ and $r_{2,t}r_{1a}$ must be investigated. Of the nine preliminary fluids, it was decided to further study water, toluene and methanol. Water is the most abundant and widely used fluid. Toluene is the best performing dry fluid and methanol is the best performing wet fluid. The thermal efficiencies of these three fluids with

varying $r_{2,h}r_{2,t}$ and $r_{2,t}r_{1a}$ coupled with mass flow rate can be seen in Figs. 82-84. An interesting feature of these figures is the values of $r_{2,h}r_{2,t}$ and $r_{2,t}r_{1a}$ that optimize the thermal efficiency for each of the fluids. Notice that the two wet fluids, water and methanol, optimize performance with low values of $r_{2,t}r_{1a}$ but high values of $r_{2,h}r_{2,t}$. Toluene, the dry fluid, optimizes its thermal performance with low values of both $r_{2,h}r_{2,t}$ and $r_{2,t}r_{1a}$.

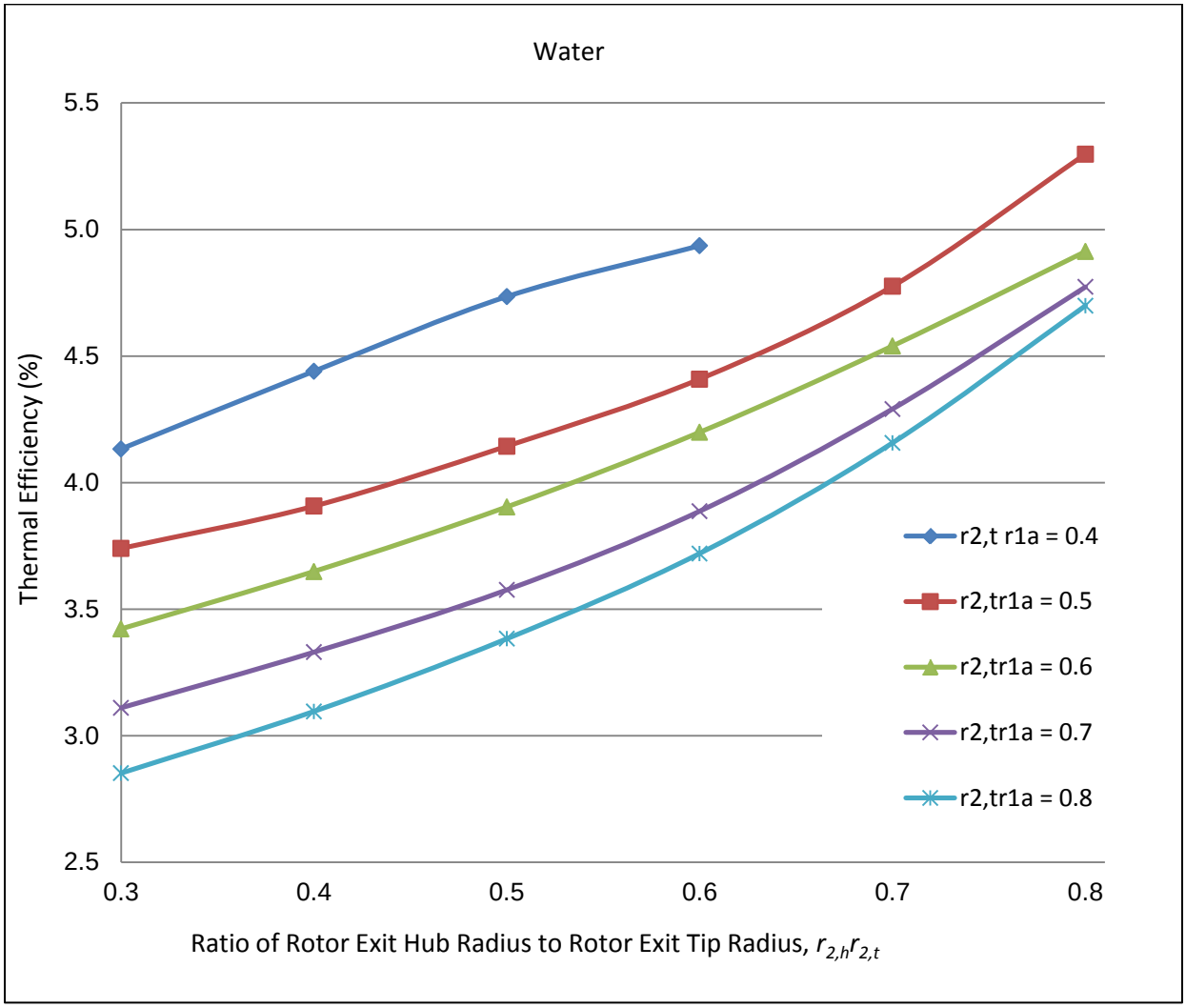

Figure 82: Thermal efficiency of water for various values of the ratio of rotor exit hub radius to rotor exit tip radius and the ratio of rotor exit tip radius to rotor inlet radius coupled with mass flow rate. All other input parameters are the case study values listed in Table 13.

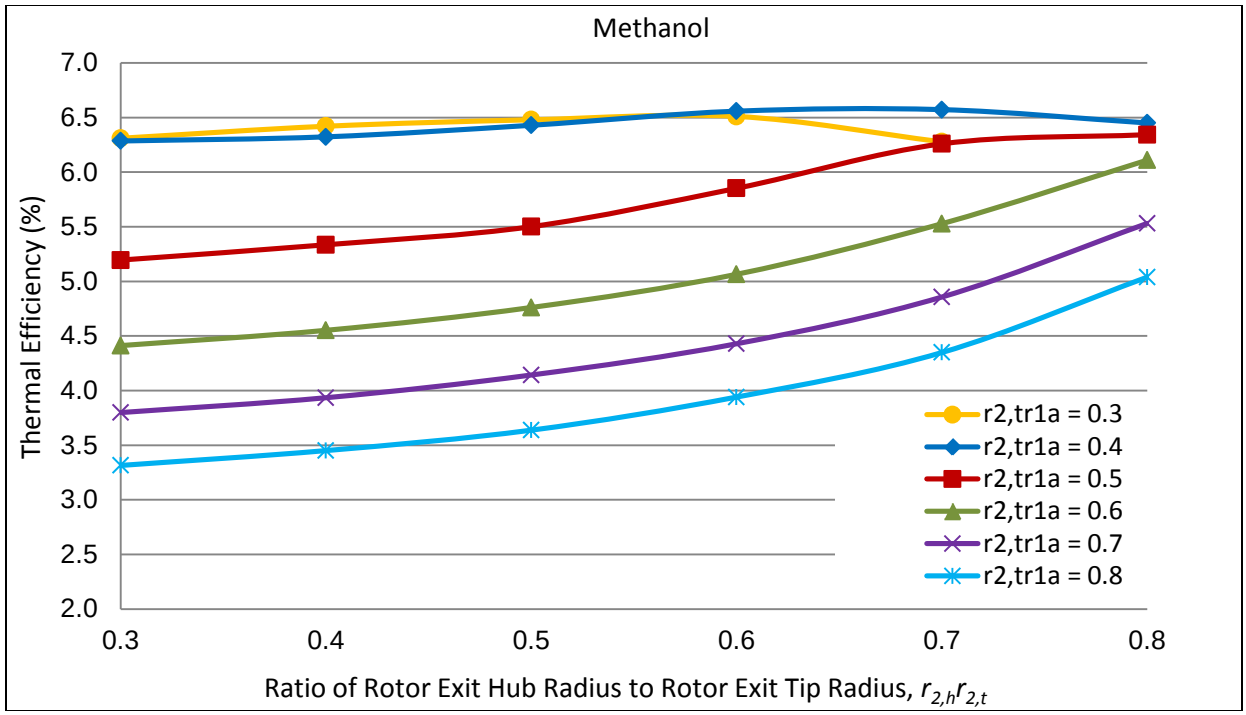

Figure 83: Thermal efficiency of methanol for various values of the ratio of rotor exit hub radius to rotor exit tip radius and the ratio of rotor exit tip radius to rotor inlet radius coupled with mass flow rate. All other input parameters are the case study values listed in Table 13.

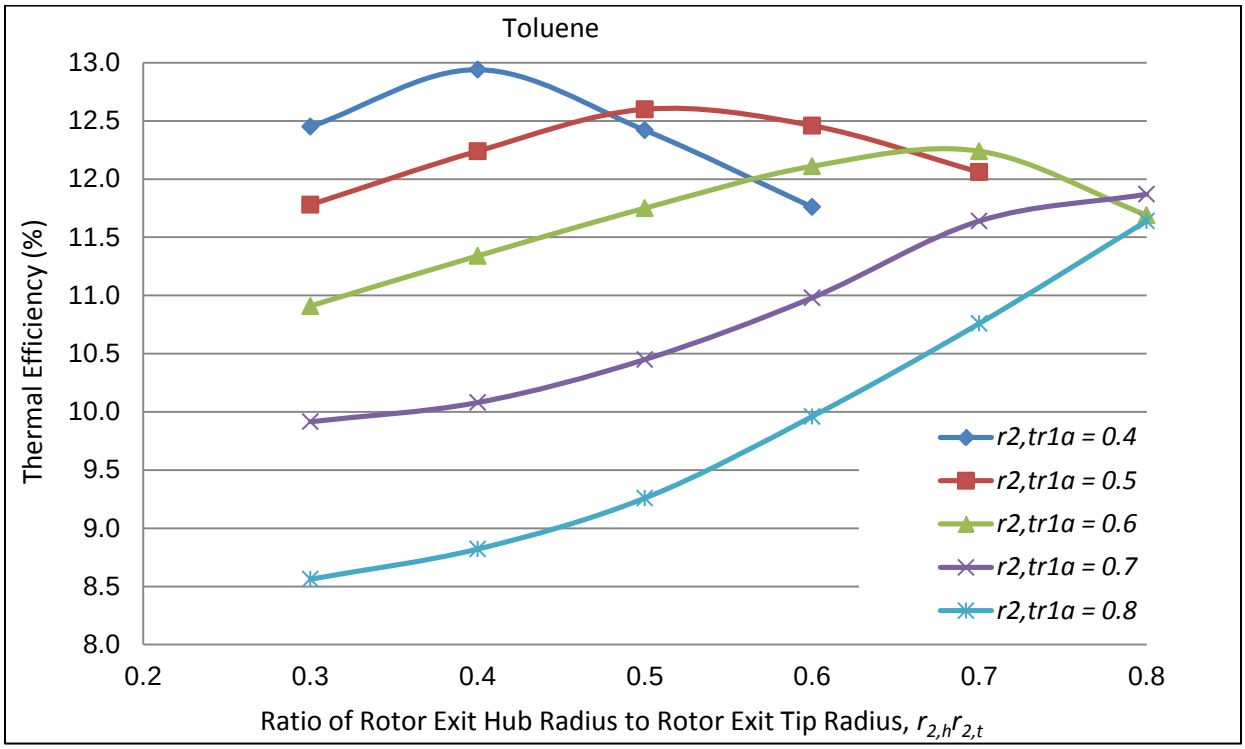

Figure 84: Thermal efficiency of toluene for various values of the ratio of rotor exit hub radius to rotor exit tip radius and the ratio of rotor exit tip radius to rotor inlet radius coupled with mass flow rate. All other input parameters are the case study values listed in Table 13.

Table 15 shows the affect of incorporating various values of $r_{2,h}r_{2,t}$ and $r_{2,t}r_{1a}$ had on the thermal performance. As predicted by the sensitivity analysis, these two input parameters could significantly alter the thermal efficiency. As seen in Table 15, changing these parameters improved the thermal efficiency of water by roughly 30%. Although the percent of change shown in the leftmost column can be quite large, the difference between the thermal efficiency optimizing $r_{2,h}r_{2,t}$ and $r_{2,t}r_{1a}$ and the thermal efficiency for case study values is at most about 1%. The difference in thermal efficiency between optimized toluene and optimized methanol is over 6%. Even after including the effects of $r_{2,h}r_{2,t}$ and $r_{2,t}r_{1a}$, high critical temperature and low molecular mass dry fluids still trump the wet fluids performance by nearly a factor of two.

Table 15: Comparison of Thermal Performance with Case Study Input Parameters with Thermal Performance Optimizing $r_{2,h}r_{2,t}$ and $r_{2,t}r_{1a}$

Fluid	Case study Thermal Efficiency	Optimized Thermal Efficiency	Difference	Percent Change in Thermal Efficiency
Water	4.14%	5.30%	1.16%	28%
Methanol	5.50%	6.57%	1.07%	19%
Toluene	12.6%	12.9%	0.3%	2.4%

Optimal Thermal Performance Fluid Analysis

The preliminary analysis suggests that dry fluids with high critical temperature and low molecular mass perform best. The next step is to search for fluids that have such properties. Fig. 85 shows many dry fluids plotted according to their critical temperature and molecular mass. Toluene has a high critical temperature and low molecular mass relative to most dry fluids. Of the fluids analyzed, decane is the only fluid with noticeably higher critical temperature. When the modified Glassman model was used, a pressure ratio so great was achieved as to cause the Mach number to exceed one. This would create a shock wave. Unfortunately, the current analysis is not sophisticated enough to handle shock waves dynamics so the results are not included in this paper. Of the fluids that have a lower molecular mass than toluene, benzene has the highest critical temperature. Benzene was studied because it has a lower molecular mass than toluene but also a lower critical temperature. Fig. 86 shows the thermal performance of benzene, which is very similar to toluene. Both have a peak thermal efficiency of about 13%.

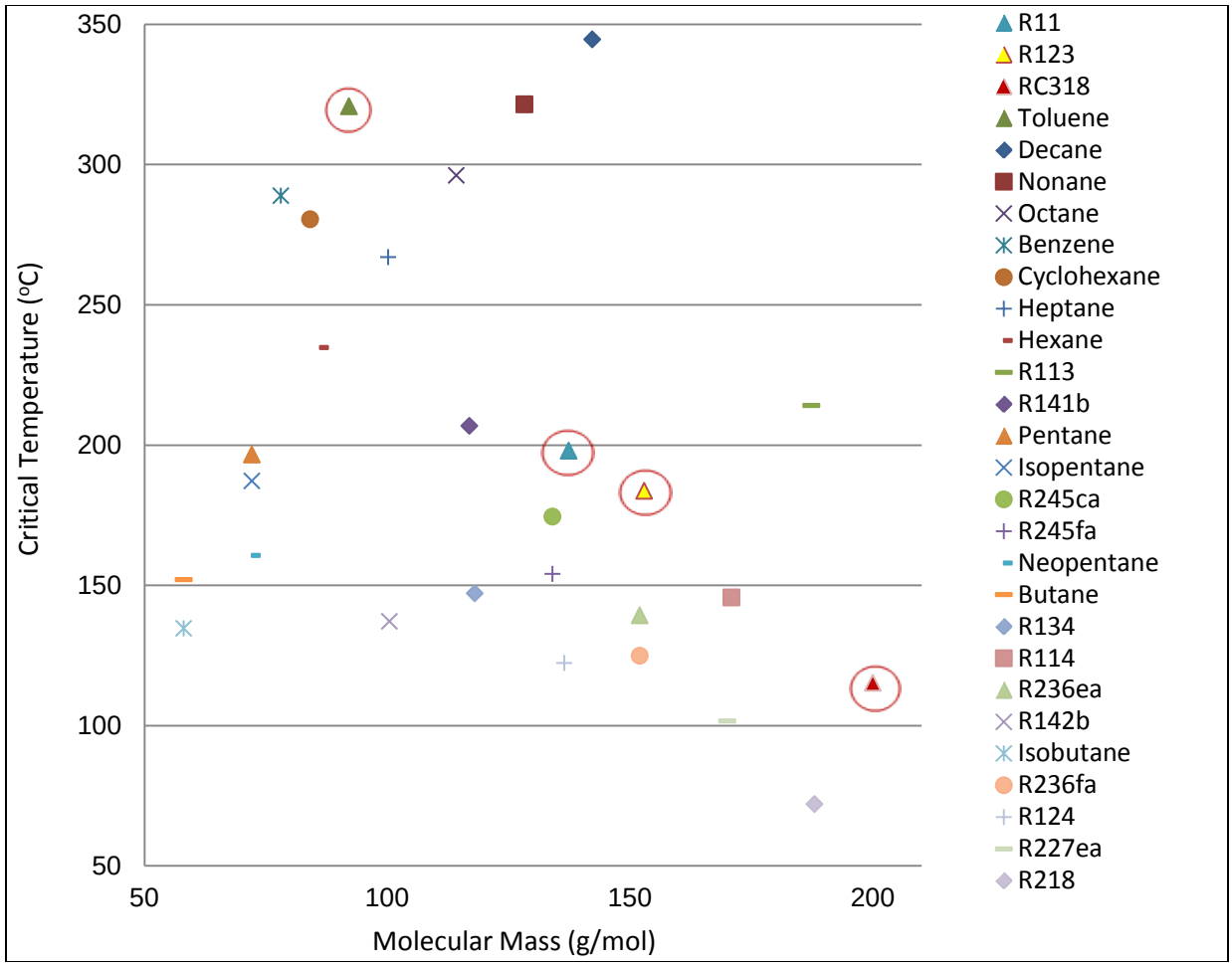

Figure 85: Dry fluids plotted according to critical temperature and molecular mass. The triangular symbols surrounded by the red circles represent fluids that have already been studied in the preliminary analysis. The desired fluids for optimal performance are those with high critical temperature and low molecular mass corresponding to those in the upper lefthand portion of the figure.

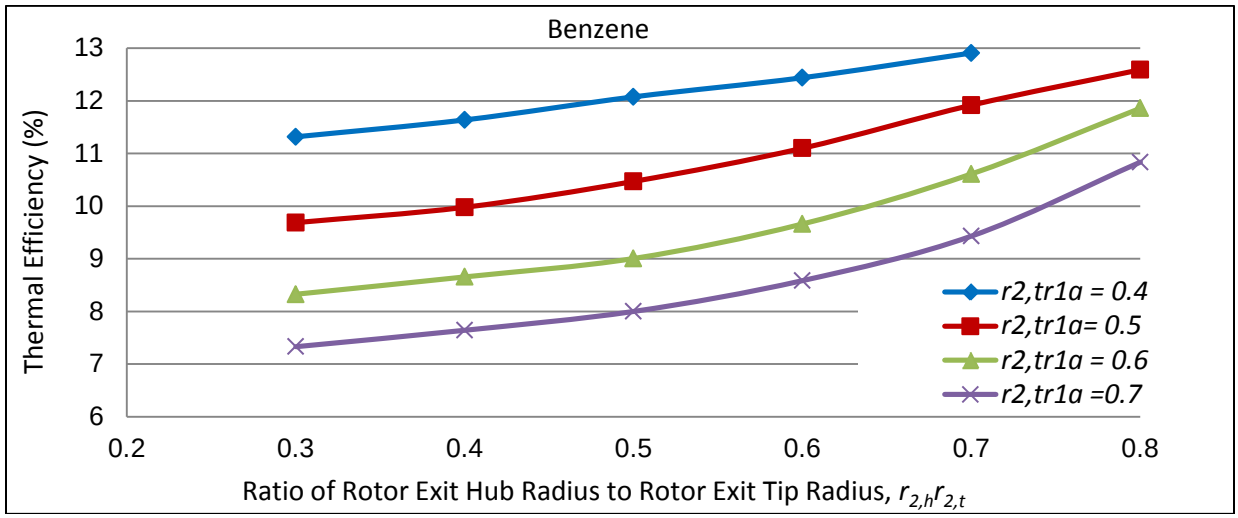

Figure 86: Thermal efficiency of benzene for various values of the ratio of rotor exit hub radius to rotor exit tip radius and the ratio of rotor exit tip radius to rotor inlet radius coupled with mass flow rate. All other input parameters are the case study values listed in Table 13.

Power Output

There may be a perceived discrepancy between thermal efficiencies of commercially available radial-inflow turbines and those addressed in this chapter. Please note that most commercially available radial-inflow turbines operate at higher power outputs. This analysis was done for a small scale (residential, small commercial, developing world applications). These have power outputs in the range of 5-10kW. Limiting the power output in turn limits the pressure drop. Fig. 87 is similar to Fig. 93 in the appendix. However, Fig. 87 includes all nine of the fluids used in the preliminary analysis. As you can see, for all fluids there is a noticeable increase in thermal efficiency with an increase of power output. Therefore, for commercially available radial-inflow turbines operating at higher power outputs, it would be expected that the thermal efficiency would be higher than those listed in this chapter.

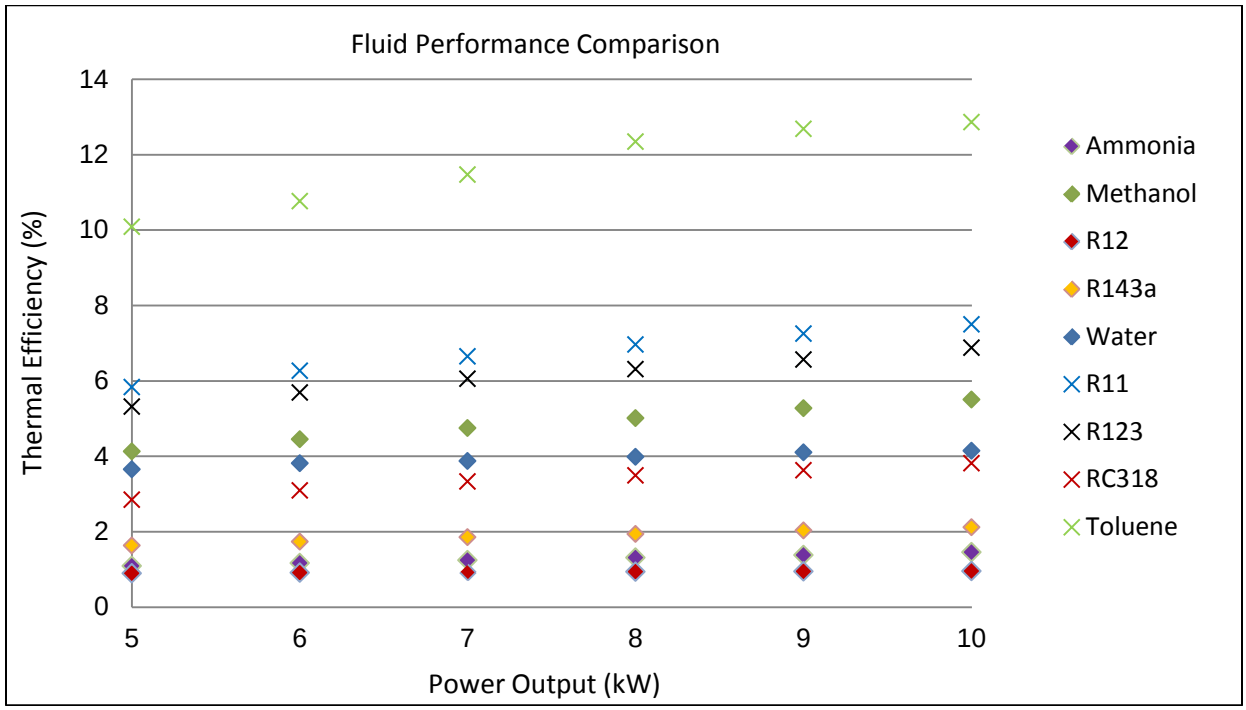

Figure 87: Effect of the power output coupled with mass flow rate on thermal efficiency for several fluids. All input parameters held at case study values.

Discussion of Radial Inflow Turbine Results

A modified version of the Glassman model was used to predict the performance of the radial-inflow turbine. A sensitivity analysis showed that of the seventeen input parameters of the modified Glassman model, the mass flow rate, $r_{2,h}r_{2,t}$ and $r_{2,t}r_{1a}$ had the greatest influence on the thermal efficiency of the system. Decreasing the mass flow rate both increased the turbine efficiency and increased the pressure drop across the turbine both of which enhanced the thermal efficiency. The effect that $r_{2,h}r_{2,t}$ and $r_{2,t}r_{1a}$ had on the thermal efficiency did not conform to as simple a trend as that of the mass flow rate. Instead, the optimized value of $r_{2,h}r_{2,t}$ and $r_{2,t}r_{1a}$ seem to depend on the type of fluid. The two wet fluids, water and methanol, had an optimal performance with low values of $r_{2,t}r_{1a}$ but high values of $r_{2,h}r_{2,t}$. Toluene, the dry fluid, had an optimal thermal performance with low values of both $r_{2,h}r_{2,t}$ and $r_{2,t}r_{1a}$.

The modified version of the Glassman model with varying mass flow rate, $r_{2,h}r_{2,t}$ and $r_{2,t}r_{1a}$ was used to determine which fluids would achieve the greatest thermal efficiency. All three variables were varied so that the optimal configuration for each fluid could be compared. Of the fluids studied it appears that dry fluids with low molecular mass and high critical temperature yielded the greatest thermal efficiency. Such fluids include toluene and benzene that produced a thermal efficiency of roughly 13%. These fluids as well as other dry fluids with low molecular mass and high critical temperature have low viscosity. The low viscosity allows these fluids to have less frictional losses in the turbine leading to better thermal efficiencies. Unfortunately, these fluids also share the characteristic of being highly toxic. Because of their toxic nature, Aoun (Aoun, 2009) initially excluded these fluids from consideration in small turbines. Water is much safer, abundant and environmentally friendly. However, it can only provide less than half the thermal efficiency, at only 5.3%. Investigations are still being done to find non-toxic fluids with low molecular mass and high critical temperature. If none are found, it is possible that a different type of turbine may be more appropriate for this application.

IV. Conclusions

As outlined in the Dept. of Energy publication "Basic Research Needs for Solar Energy Utilization," (Lewis & Crabtree, 2005) moderate temperature distributed solar thermal is an area where there is potential for significant innovation to reduce the cost of solar energy. Two areas for innovation were explored: reduced thermal losses in a novel dual-chamber absorber tube and parametric study for optimal efficiency of small-scale radial inflow turbines.

The commercially used solar absorber tube design for a parabolic trough solar collector is a simple tube. As the peak temperature in solar thermal systems increases to allow for increase cycle thermal efficiency, the simple tube suffers from higher wall temperatures and increased thermal losses to the surroundings. A novel finned dual-chamber absorber tube design was presented as a possible solution. Fins attached to the outer wall could serve as a heat sink to send heat into the inner chamber. Computation modeling using the Kandlikar's correlation (Kandlikar, 1991) for two phase saturated boiling when fluid entered the outer chamber and the Stephan and Abdelsalam correlation (Stephan & Abdelsalam, 1980) for fluid entering the inner chamber was validated by a reduced-scale experiment. 82.5% of the experimental data for fluid entering the outer chamber agrees within 16% of the computational model, which is the expected accuracy of the Kandlikar correlation (Kandlikar, 1991). 90% of the experimental data for fluid entering the inner chamber agrees within 11.3%, which is the expected accuracy of the Stephan and Abdelsalam correlation (Stephan & Abdelsalam, 1980). From these models, it has been demonstrated that the heat loss to the environment from the outer wall of the absorber tube could be reduced by 10-60%. The best performance was found when water enters the outer chamber at the highest mass flow rate. This impressive improvement encourages further development of the dual chamber design.

A modified Glassman model was used to complete a parametric study of small-scale radial inflow turbines. Of the seventeen input parameters of the modified Glassman model, the mass flow rate, $r_{2,h}r_{2,t}$ and $r_{2,t}r_{1a}$ had the greatest influence on the thermal efficiency of the system. Decreasing the mass flow rate both increased the turbine efficiency and increased the pressure

drop across the turbine both of which enhanced the thermal efficiency. The optimized value of $r_{2,h}r_{2,t}$ and $r_{2,t}r_{1a}$ seem to depend on the type of fluid. Wet fluids had an optimal performance with low values of $r_{2,t}r_{1a}$ but high values of $r_{2,h}r_{2,t}$. Dry fluids had an optimal thermal performance with low values of both $r_{2,h}r_{2,t}$ and $r_{2,t}r_{1a}$. Of the fluids studied it appears that dry fluids with low molecular mass and high critical temperature yielded the greatest thermal efficiency. Such fluids typically have low viscosity, allowing there to be less frictional losses in the turbine leading to better thermal efficiencies. Unfortunately, these fluids also share the characteristic of being highly toxic. Water is much safer, abundant and environmentally friendly. However, it can only provide less than half the thermal efficiency. Investigations are still being done to find non-toxic fluids with low molecular mass and high critical temperature. If none are found, it is possible that a different type of turbine may be more appropriate for this application.

V. Suggestions for Further Research

This research has served as a proof of concept to demonstrate the potential for the dual-chamber solar absorber tube. Since the preliminary results suggest significant decrease in thermal losses, it is recommended to further investigate this design.

The preliminary results showed that only 10 – 15% of the total heat was transferred to the inner chamber. It would be advantageous to investigate ways to transfer more heat into the inner chamber. There are many possible ways that this could be achieved. There could be additional or thicker fins connecting the outer wall to the inner chamber wall. Alternatively, tripping the flow in the inner chamber into turbulence, perhaps by increased surface roughness, could increase the heat transfer coefficient in the inner chamber. However, this would have the adverse effect of also increasing the pressure losses. When fluid enters the outer chamber, some sort of insulation along the outer surface of the inner chamber wall and the sides of the outer chamber fins could limit heat transfer from the inner chamber to the outer chamber fluid. The inner chamber would receive heat from the outer wall surface via the fins only. The inlet/outlet port had the benefit of creating more radially uniform flow. However, it also behaved as a counter-flow heat exchanger transferring heat between the inner and outer chamber. Insulation could be placed between the chambers in this segment or the axial length could be reduced. It should be noted that strategically placing insulation would increase manufacturing costs.

The style and placement of the fins should be further explored. Fins could be varied in thickness, length, number of fins, and type of fins. There is concern that the strip fin configuration may cause entrainment resulting in localized high wall temperatures. Fluid flow around various fin configurations could best be observed with experiments utilizing a translucent outer wall or a more advanced computational fluid model.

A single chamber extension of the inner chamber beyond the dual-chamber design could be explored. It is important to realize that the outer wall temperature was only about 125 C. A temperature gradient is needed between the fluid in the inner chamber and the outer wall; thus, limiting how much superheat can occur in the inner chamber. For high temperature applications, it may be advantageous to couple the dual-chamber and single chamber designs.

More advanced fluid model using programs such as ANSYS FLUENT would allow for better characterization of the flow and optimization of the design parameters.

Finally, in terms of the radial-inflow turbine, further research would need to be done to find non-toxic fluids with low molecular mass and high critical temperature. If none are found, other turbines should be investigated for this application.

VI. References

Aoun, B. (2009). *Micro combined heat and power operating on renewable energy for residential building.* PhD Thesis, Sciences des Métiers de l'Ingénieur.

Bejan, A. (1995). *Convective Heat Transfer, 2nd Edition.* New York: Wiley & Sons, Inc.

Carey, V. (2007). *Liquid-Vapor Phase-Change Phenomena 2nd Edition.* New York, NY: Hemisphere Publishing Corporation.

Carey, V., & Mandrusiak, G. (1986). Annular film-flow boiling of liquids in a partially heated vertical channel with offset strip fins. *Int. J. of Heat and Mass Transfer , 29*, 927-939.

Chen, J. (1966). Correlation for boiling heat transfer to saturated fluids in convective flow. *Ind. Eng. Chem. Proc. Design and Dev. , 5* (3), 322-339.

Collier, J. (1981). Forced convective boiling. In A. Bergles, J. G. Collier, J. Delhaye, & G. F. Hewitt, *Two-Phase Flow and Heat Transfer in the Power and Process Industries.* New York, NY: Hemisphere Publishing.

Fernandez-Garcia, A., Zarza, E., Valenzuela, L., & Perez, M. (2010). Parabolic-Trough Solar Collectors and Their Applications. *Renewable and Sustainable Energy Reviews , 14*, 1695-1721.

Forster, H., & Zuber, N. (1955). Dynamics of vapor bubbles and boiling heat transfer. *AIChE Journal , 1*, 531-535.

García-Valladares, O., & Velázquez, N. (2009). Numerical simulation of parabolic trough solar collector: Improvement using counter flow concentric circular heat exchangers. *International Journal of Heat and Mass Transfer , 52*, 597–609.

Geary, D. (1975). Return bend pressure drop in refrigeration systems. *ASHRAE Transactions , 81* (1), 250-265.

Glassman, A. J. (1976). *Computer Program for Design Analysis of Radial-Inflow Turbines.* Lewis Research Center, NASA.

Gnielinski, V. (1975). New equation for heat and mass transfer in the turbulent flow in pipes and channels. *Forschung im Ingenieurwesen , 41* (1), 8-16.

Hoffren, J., Talonpoika, T., Larjola, J., & Siikonen, T. (2002). Numerical simulation of real-gas flow in a supersonic turbine nozzle ring. *Journal of Engineering for Gas Turbines and Power , 124*, 395–403.

Idelchik, I. (1994). *Handbook of Hydraulic Resistance, 3rd Edition.* Ann Arbor: CRC Press, Inc.

Jaques, N. (2010). Direct Steam Generation: Full Steam Ahead for Grid Parity. *CSP Today* .

Jones, A. (1996). Design and Test of a Small, High Pressure Ratio Radial Turbine. *Journal of Turbomachinery , 118*, 362–370.

Jones, G., & Bouamane, L. (2012). *'Power from Sunshine': A Business History of Solar Energy.* Boston, MA: Harvard Business School Working Paper, No. 12–105.

Joshi, H., & Webb, R. (1987). Heat Transfer and Friction in the Offset Strip Fin Heat Exchanger. *Int. J. Heat Mass Transfer , 30*, 69-84.

Kalogirou, S. (2004). Solar Thermal Collectors and Applications. *Progress in Energy and Combustion Science , 30*, 231-295.

Kandlikar, S. (1991). Development of a flow boiling map for subcooled and saturated flow boiling of different fluids in circular tubes. *J. Heat Transfer , 113*, 190-200.

Kaushika, N. (1993). Viability Aspects of Paraboloidal Dish Solar Collector Systems. *Renewable Energy , 3*, 787 – 793.

Kays, W., Crawford, M., & Weigand, B. (2005). *Convective Heat and Mass Transfer, 4th Edition.* Boston, MA: McGraw Hill.

Kim, J., Simon, T., & Viskanta, R. (1993). Journal of Heat Transfer Policy on Reporting Uncertainties in Experimental Measurements and Results. *Journal of Heat Transfer , 115* (1), 5-6.

Lewis, N., & Crabtree, G. (2005). *Research Needs for Solar Energy Utilization: Report of the Basic Energy Sciences Workshop on Solar Utilization.* US Department of Energy Office of Basic Energy Sciences.

Lockhart, R. W., & Martinelli, R. C. (1949). Proposed correlation of data for isothermal two-phase, two-component flow in pipes. *Chemical Engineering Progress , 45* (1), 39-48.

Lundberg, R., McCuen, P., & Reynolds, W. (1963). Heat Transfer in Annular Passages: Hydrodynamically Developed Flow with Arbitrarily Prescribed Wall Temperatures or Heat Fluxes. *Int. J. Heat Mass Transfer, 6*, 495-529.

Mandhane, J., Gregory, G., & Aziz, K. (1974). Flow pattern map for gas-liquid flow in horizontal pipes. *Int. J. Multiphase Flow , 1*, 537-553.

Manglik, R. M., & Bergles, A. E. (1995). Heat Transfer and Pressure Drop Correlations for the Rectangular Offset Strip Fin Compact Heat Exchanger. *Experimental Thermal and Fluid Science , 10* (2), 171-180.

Marseille, T., Carey, V., & Estergreen, S. (1988). Full-Core Test Method for Experimental Determination of Convective Boiling Heat Transfer Coefficients in Tubes of Crossflow Compact Evaporators. *Experimental Thermal and Fluid Science , 1* (4), 395–404.

Martinelli, R. C., & Nelson, D. B. (1948). Prediction of pressure drop during forced-circulation boiling of water. *Trans. ASME , 70*, 695-702.

Mastai, Y., Polarz, S., & Antonietti, M. (2002). Silica-Carbon Nanocomposites–A New Concept for the Design of Solar Absorbers. *Advanced Functional Materials , 12* (3), 197-202.

Mills, D. (2004). Advances in Solar Thermal Electricity Technology. *Solar Energy , 76*, 19 – 31.

Morgan, S. (2007). *From Windmills to Hydrogen Fuel Cells: Discovering Alternative Energy.* London: Heinemann.

Munoz, J., & Abanades, A. (2011). Analysis of Internal Helically Finned Tubes for Parabolic Trough Design by CFD Tools. *Applied Energy , 88* (11), 4139–4149.

NIST. (1992). National Institute of Standards and Technology Thermophysical Properties of Pure Substances, Version 3.0. Gaithersburg, MD.

Osborn, D., & Collier, D. (1996). Utility Grid-Connected Distributed Power Systems. *National Solar Energy Conference.* Asheville, NC: American Solar Energy Society.

Pihl, E., Kushnir, D., Sanden, B., & Johnsson, F. (2012). Material constraints for concentrating solar thermal power. *Energy , 44* (1), 944–954.

Price, T. (2009). Direct Steam Generation: Steamlining Parabolic Trough Plants. *CSP Today* .

Raj, R., Srinivas, T., Natarajan, M., Kumar, K., Chengappa, A., & Deoras, A. (2013). Experimental and numerical analysis using CFD technique of the performance of the absorber tube of a solar parabolic trough collector with and without insertion. *International Conference on Energy Efficient Technologies for Sustainability (ICEETS).* Kanyakumari, Tamilnadu, India.

RawSolar. (2009). Retrieved from http://www.raw-solar.com/

Shuman, F. (1914). Feasibility of Utilizing Power From the Sun. *Scientific America , 110*, 179.

Spence, S., & Artt, D. (1997). Experimental Performance Evaluation of a 99.0 mm Radial Inflow Nozzled Turbine with Different Stator Throat Areas. *Journal of Power and Energy , 211*, 477–488.

Stephan, K., & Abdelsalam, M. (1980). Heat-transfer correlations for natural convection boiling. *Int. J. Heat and Mass Transfer , 23*, 73-87.

Whitfield, A. (1990). The Preliminary Design of Radial Inflow Turbines. *Journal of Turbomachinery , 112*, 50–57.

VII. Appendix

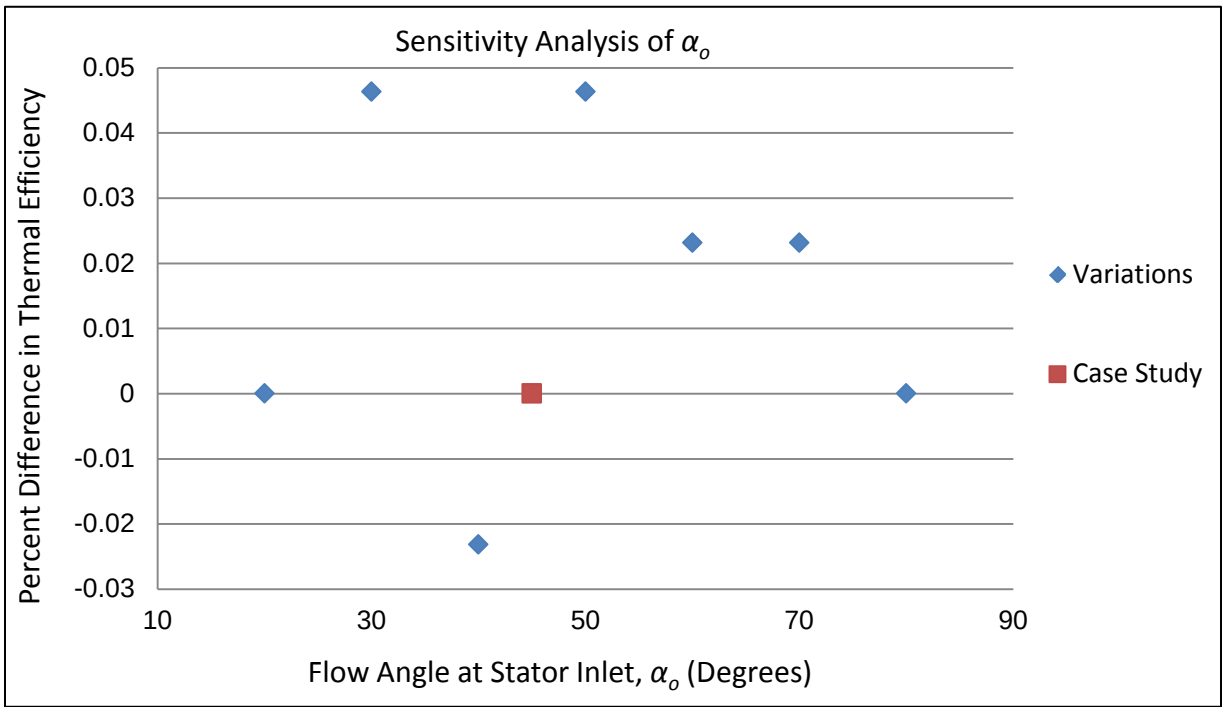

Figure 88: Effect of flow angle at stator inlet coupled with mass flow rate on thermal efficiency. All other input parameters held at case study values. Water is the operating fluid.

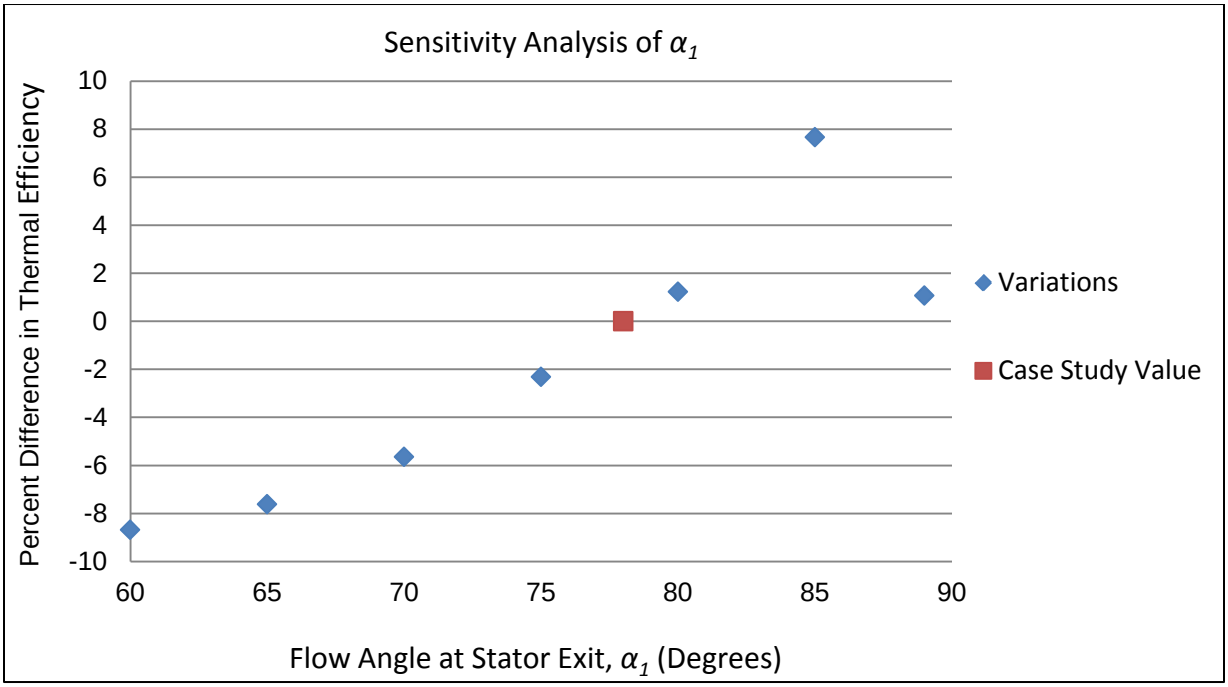

Figure 89: Effect of flow angle at stator exit coupled with mass flow rate on thermal efficiency. All other input parameters held at case study values. Water is the operating fluid.

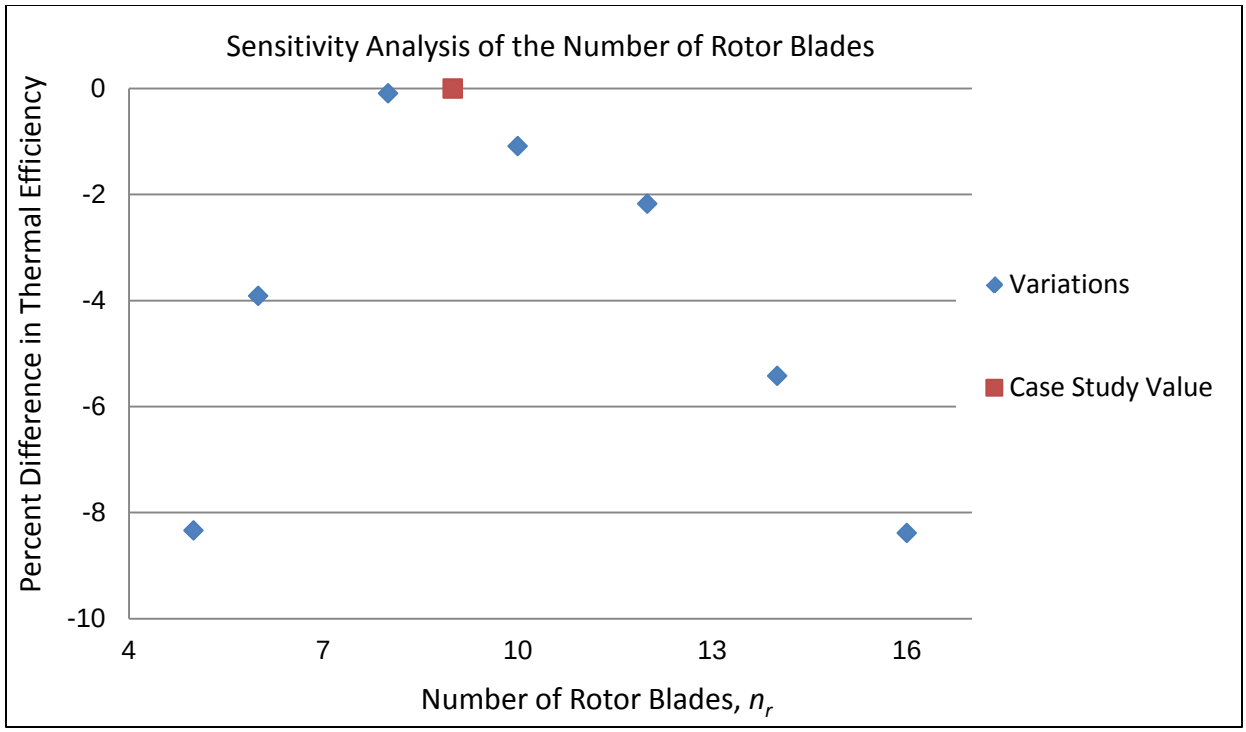

Figure 90: Effect of the number of rotor blades coupled with mass flow rate on thermal efficiency. All other input parameters held at case study values. Water is the operating fluid.

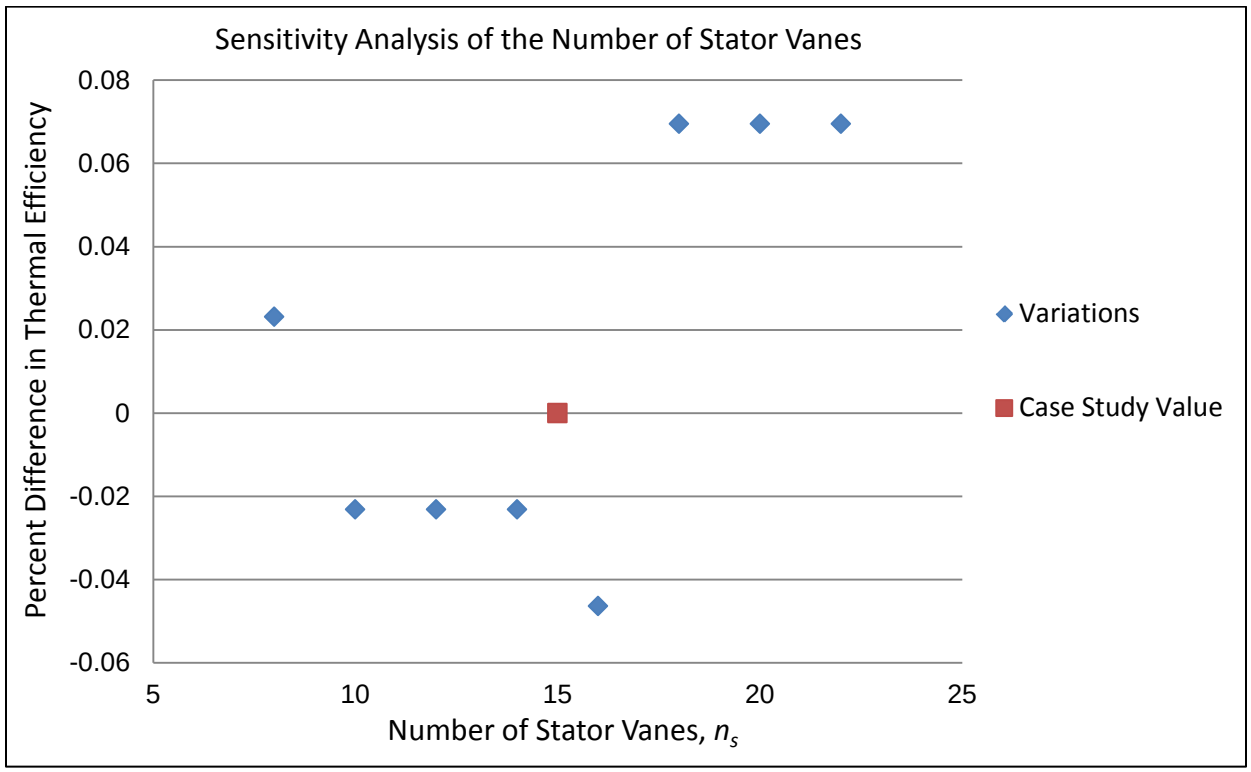

Figure 91: Effect of the number of stator vanes coupled with mass flow rate on thermal efficiency. All other input parameters held at case study values. Water is the operating fluid.

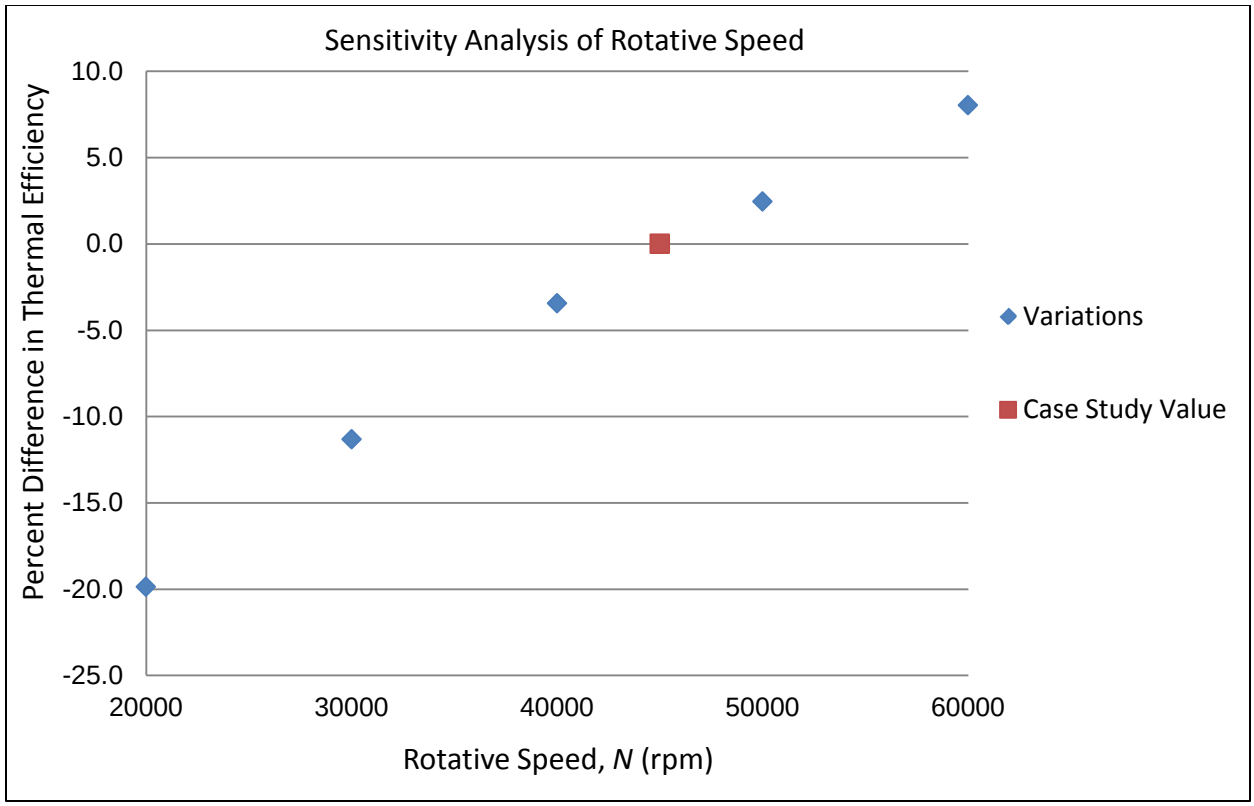

Figure 92: Effect of the rotative speed coupled with mass flow rate on thermal efficiency. All other input parameters held at case study values. Water is the operating fluid.

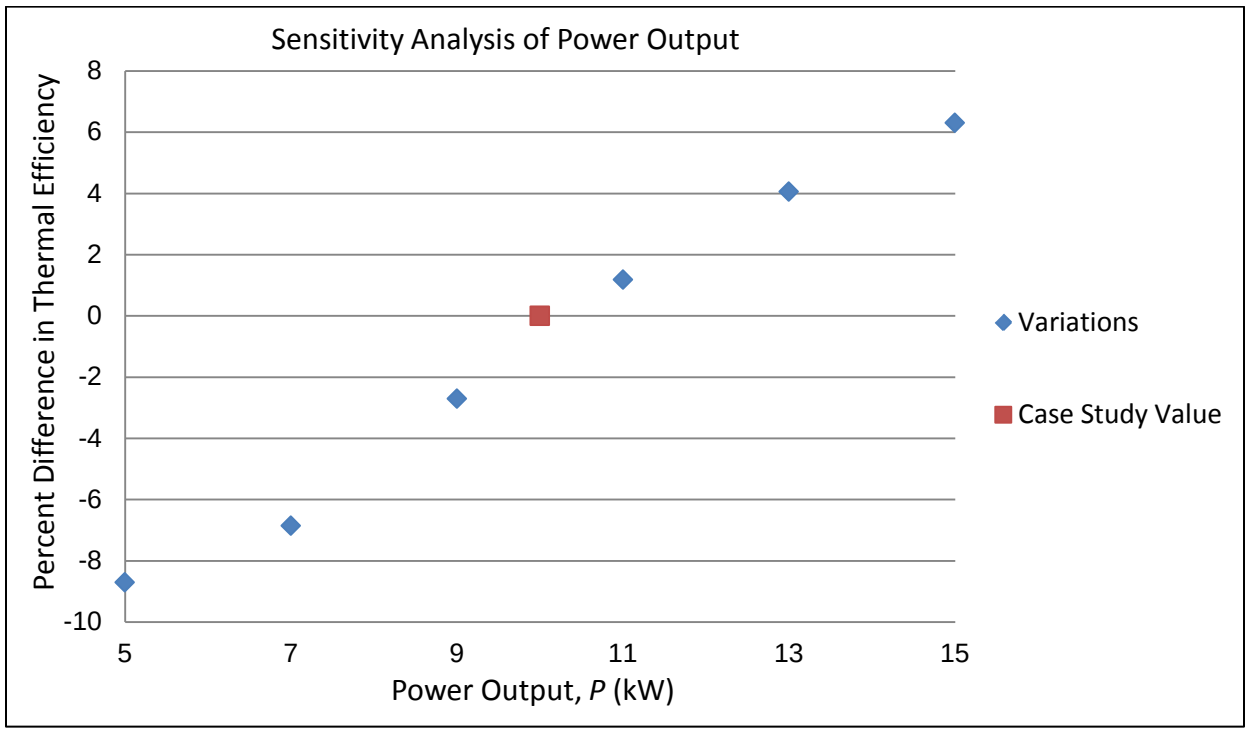

Figure 93: Effect of the power output coupled with mass flow rate on thermal efficiency. All other input parameters held at case study values. Water is the operating fluid.

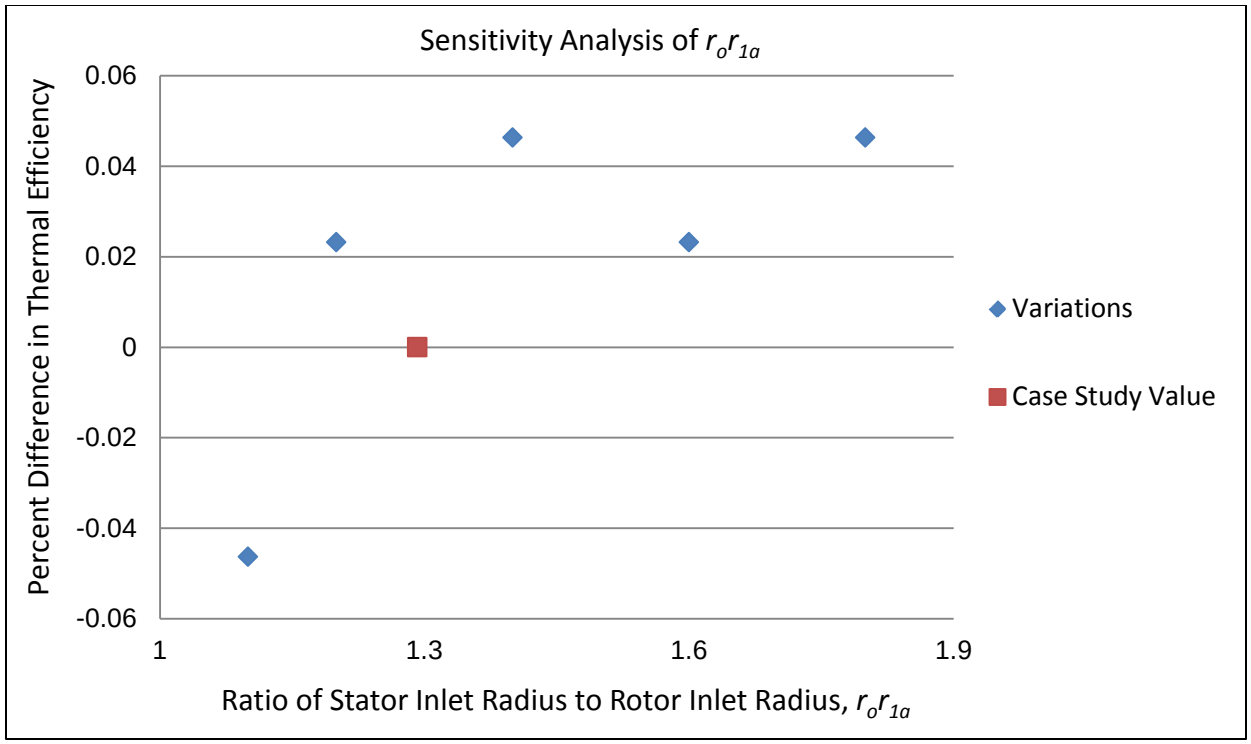

Figure 94: Effect of the ratio of stator inlet radius to rotor inlet radius coupled with mass flow rate on thermal efficiency. All other input parameters held at case study values. Water is the operating fluid.

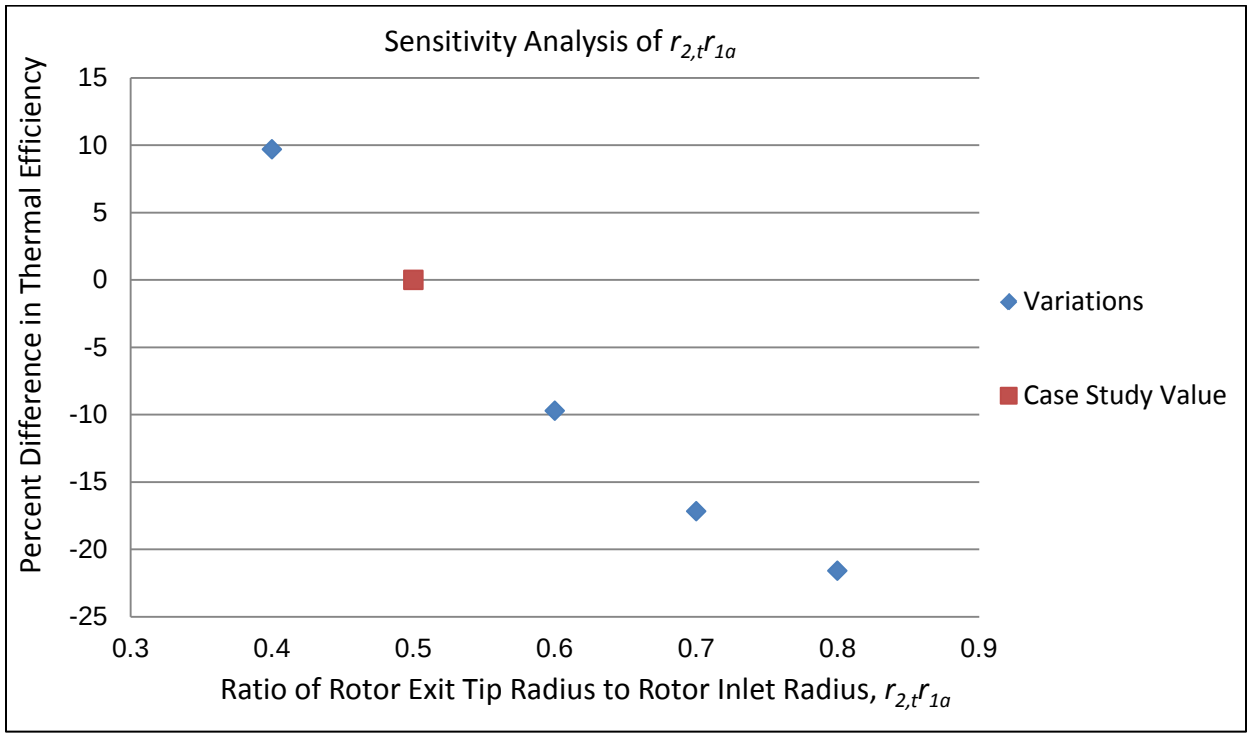

Figure 95: Effect of the ratio of rotor exit tip radius to rotor inlet radius coupled with mass flow rate on thermal efficiency. All other input parameters held at case study values. Water is the operating fluid.

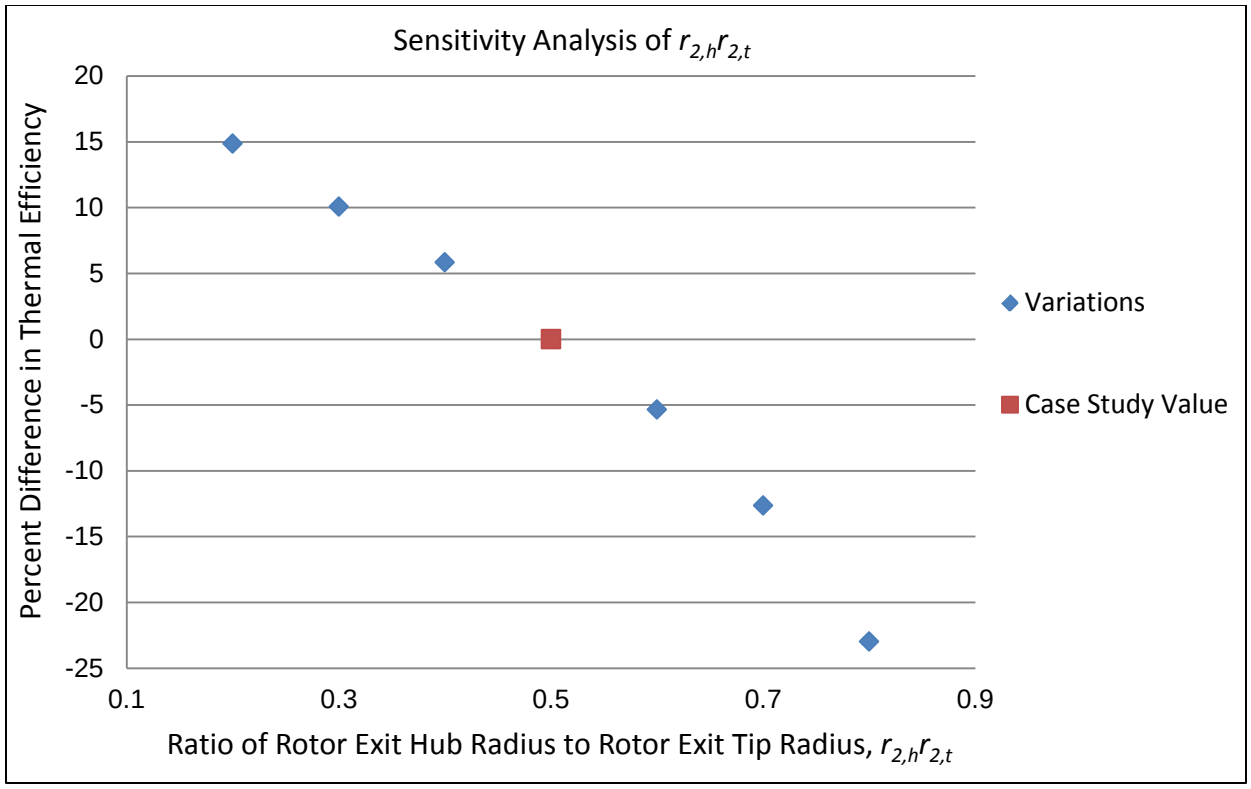

Figure 96: Effect of the ratio of rotor exit hub radius to rotor exit tip radius coupled with mass flow rate on thermal efficiency. All other input parameters held at case study values. Water is the operating fluid.